Title

Multifunctional Neural Probes for Electrochemical Sensing, Chemical Delivery and Optical Stimulation

Permalink

https://escholarship.org/uc/item/5kv1n6r0

Author

Wen, Ximiao

Publication Date

2018

Peer reviewed|Thesis/dissertation

UNIVERSITY OF CALIFORNIA

Los Angeles

Multifunctional Neural Probes for Electrochemical Sensing, Chemical

Delivery and Optical Stimulation

A dissertation submitted in partial satisfaction of the

requirements for the degree Doctor of Philosophy

in Mechanical Engineering

by

Ximiao Wen

2018

ABSTRACT OF THE DISSERTATION

Multifunctional Neural Probes for Electrochemical Sensing,

Chemical Delivery and Optical Stimulation

by

Ximiao Wen

Doctor of Philosophy in Mechanical Engineering

University of California, Los Angeles, 2018

Professor Pei-Yu Chiou, Chair

Implantable neural probes are one of the most important technologies for neuroscientists to detect and stimulate neural activities inside the brain to advance the understanding of brain function and behavior, especially in the deep brain regions where other non-invasive approaches cannot reach. With the development of microelectromechanical systems (MEMS) in the past few decades, a great amount of efforts has been made to improve the neural probes to provide reliable and versatile tools to enable neuroscience studies that otherwise impossible to conduct.

In this dissertation, I focused on three important objectives to improve the current neural probe platform: 1) to incorporate optical stimulation capability on top of the current silicon-based microelectrode arrays (MEAs) with electrochemical sensing function for optogenetics applications; 2) to integrate microfluidic channels with the current silicon

platform for chemical deliveries; and 3) to develop a soft neural probe to reduce the brain damage and foreign body response. All the probes developed in this work are capable of deep brain implantation (>5 mm) and equipped with various electrochemical biosensors to study neural activities in deep brain regions.

For the first objective, an ultra-thin silicon nitride waveguide was integrated on top of the silicon probe using grating couplers to couple light in and out of the waveguide. PECVD silicon nitride film was optimized to reduce the waveguide propagation loss to ~ 3dB/cm at 450 nm wavelength. The probe is capable of delivering ~40 µW light power to the probe tip with ~2 mW input light power from a 3 µm polarization maintaining optical fiber coupled with a pigtailed laser diode. The average light intensity is ~200 mW/mm^2 which is sufficient for Channelrhodopsin-2 excitation. Using this probe, we have detected optically-evoked glutamate release in the rat nucleus accumbens several weeks after injection of channelrhodopsin-expressing AAV into the above region.

For the second objective, PDMS microfluidic channels were transferred to the front and backside of the current Si probes using a novel PDMS thin-film transfer process. With this process, microfluidic channels can be easily bonded to Si probes as an add-on module to provide a simple solution to integrate chemical delivery functions into existing silicon-based probes, providing another level of control of the brain activities. Local injection of drug solution with nanoliter precision can be controlled by the pumping pressure and duration. The system was validated in vivo by local glucose injection through the fluidic channel and detection by biosensors in rat striatum.

For the third objective, a multifunctional neural probe with Ultra-Large Tunable Stiffness (ULTS) was developed for chemical sensing, delivery and deep brain

implantation, whose stiffness can be tuned by 5 orders of magnitude before and after brain implantation. ULTS probe is stiff enough to penetrate 2 cm deep into a gel with similar mechanical properties as the brain tissue and becomes soft and flexible within few minutes to minimize brain damage due to the brain movements in all directions. With appropriate coatings, the electrodes on ULTS were converted into different biosensors which exhibits similar sensing performance as previous Si probes. The integration of microfluidic channels permits delivery of chemicals in the local vicinity of the sensing sites. Acute stimulation and sensing experiments were conducted in rats, in which potassium induced glutamate release was recorded demonstrating the capability of in vivo application. The chronic immune response was compared between ULTS and silicon probes with similar geometry, which shows a reduced immune response indicated by the lower astrocytes density around ULTS.

The dissertation of Ximiao Wen is approved.

Harold G. Monbouquette

Tsu-Chin Tsao

Yong Chen

Pei-Yu Chiou, Committee Chair

University of California, Los Angeles

2018

Contents

LIST OF FIGURES

ACKNOWLEDGEMENTS

It has been an extremely challenging and precious experience and journey working towards my Ph.D. degree in Mechanical and Aerospace Engineering at the University of California, Los Angeles. I want to express my sincere gratitude to all who have provided invaluable guidance, advice and support to help me grow and overcome all the obstacles in the past six years, without which this work would not have been possible.

First and foremost, I would like to thank my advisor, Prof. Pei-Yu Chiou, for having me study and work in his research lab. I am extremely grateful to be able to work under his guidance for not only equipping me with a solid foundation in knowledge and problem-solving skills, but also giving me encouragements and trusts that motivates me to move forward. His passion and persistence in creating truly innovative ideas that have significant impact to the field and society greatly influenced me to step out of the comfort zone.

I would also like to thank my dissertation committee, Prof. Harold G. Monbouquette, Prof. Tsu-Chin Tsao and Prof. Yong Chen for their professional advice, suggestions and time on my work.

The work presented here could not have been possible without the close collaborations between neuroscience and engineering. Prof. Nigel T. Maidment, in the department of psychiatry & biobehavioral sciences, has provided invaluable advice and supports on the animal experiment to validate the devices. I would like to thank everyone in his lab that helped me with animal experiment, especially his post-doc, Bo Wang, who hold a Ph.D. degree in chemical engineering and just started working in the neuroscience lab. I extremely appreciate his expertise in making biosensors, and more importantly his

VITA

Education

2008-2012   BEng., Electronic & Computer Engineering

The Hong Kong University of Science and Technology (HKUST)

Hong Kong, China

Publications and Presentations

- *__Wen, X.__, *Wang, B., Liu T, Huang S, Lee M.S., Chung, P.Y., Chow Y.T., Maidment N, Chiou P.Y., "Multifunctional Neural Probe with Ultra-Large Tunable Stiffness for Deep Brain Penetration, Delivery, and Sensing," 2018 (In preparation)

- *Wang, B., *__Wen, X__., Maidment N, Chiou P. Y., "A Hybrid Silicon-PDMS Glutamate Microbiosensor Integrated with On-probe Reference and Microfluidic Channel," 2018 (In preparation)

- Wang, B., __Wen, X.__, Maidment N., "Nanostructured Platinum Modified Carbon Fiber Microelectrode for Electrochemical Sensing of Hydrogen Peroxide", 2018 (in preparation)

- Chow, Y. T., Man, T., Acosta, G., Zhu, X., __Wen, X.__, Chung, P.-S., Liu, T., Wu, B. M., Chiou, P. Y., "Liquid Metal-Based Multifunctional Micropipette for Four-Dimensional Single Cell Manipulation," Advanced Science, 2018

- Xiao, F., __Wen, X.__, Tanm X. H. M., Chiou, P. Y., "Plasmonic micropillars for precision cell force measurement across a large field-of-view," Applied Physics Letters, 112, 033701. 2018.

- *Frank AC, *Huang S, Zhou M, Gdalyahu A, Kastellakis G, Silva TK, Lu E, __Wen X__, Poirazi P, Trachtenberg JT, Silva AJ. (2018) Hotspots of dendritic spine turnover facilitate learning-related clustered spine addition and learning and memory. Nature Communications. 9(1):422. PMID: 29379017

- Wu, Y.-C., Wu, T.-H., Clemens, D. L., Lee, B.-Y., __Wen, X.__, Horwitz, M. A., Teitell, M. A., Chiou, P. Y., "Massively parallel large cargo delivery into mammalian cells with light pulses," Nature Methods, 12, 439-444, 2015.

- __Wen, X.__, Liu, T., Chiou, P. Y., "A hybrid silicon-PDMS multifunctional neural probe," in 2016 International Conference on Optical MEMS and Nanophotonics (OMN), Singapore, 2016, pp. 1-2.

- Chow, Y. T., Man, T., Acosta-Velez, G. F., Zhu, X., __Wen, X.__, Chung, P.-S., Liu, T. Y.,

Wu, B. M., Chiou, P. Y., "Rapid fabrication of multifunctional microcapillar for four-dimensional single cell manipulation, "in the proceeding of the 30th Annual International Conference on IEEE Micro Electro Mechanical Systems (MEMS '18), pp. 1-4, 2018.

- Man, T., Zhu, X., Chow, Y. T., Liu, T., **Wen, X.**, Teitell, M.A., Chiou, P.Y., "Photothermal Intracellular Delivery with Self-Aligned Cell Seeding," 2017 IEEE International Conference on Optical MEMS and Nanophotonics, DOI: 10.1109/OMN.2017.8051513, pp. 1-2, 2017.

- Liu, T., **Wen, X.**, Kung, Y.-C., Chiou, P.Y., "Fabrication Strategy for Micro Soft Robotics with Semiconductor Devices Integration," in the proceeding of the 29th Annual International Conference on Micro Electro Mechanical Systems (MEMS '17), pp. 663-666, 2017.

- Xiao, F., **Wen, X.**, Chiou, P.Y.," Plasmonic Micropillars for Massively Parallel Precision Cell Force Measurement," in the proceeding of the 29th Annual International Conference on Micro Electro Mechanical Systems (MEMS '17), pp. 243-246, 2017.

- Wu, Y.-C., Santra, T. S., Wu, T.-H., Clemens, D. L., Lee, B.-Y., **Wen, X.**, Horwitz, M., Teitell, M. A., Chiou, P. Y., "Photothermal nanoblades for delivery of large-sized cargo into mammalian cells at high throughput," in the proceeding of IEEE Nano 2016, pp 47-50, 2016.

- Xiao, F., **Wen, X.**, Chiou, P. Y., "Gold nanoparticle embedded PDMS micropillar array for large area cell force sensing," in Proceedings of Optofluidics 2015, pp 1-2, 2015. (Best paper award)

Chapter 1

Introduction

Brain is the most vital component of the human body, however it is least understood and its disorders are the most difficult to treat due to the extreme complexity[1]. Neurologic disorders accounts for 3% of total global burden of disease measured in disability-adjusted life years, such as Alzheimer's disease, Parkinson's disease, and epilepsy[2]. Therefore, it is of the utmost importance to understand the brain so that we can find treatments to brain diseases and create tools to enhance brain functions.

Neural signal propagations are composed of conduction (electrical signal propagates within neurons) and neurotransmission (movement of chemicals across neurons) (**Figure 1.1**). Various technologies have been developed to monitor the signal propagation and can be categorized into two major types, optical-based and electrical-based. Optical imaging[3]–[5] provides high spatial-resolution and fair temporal resolution detection over a large area, however its application is often limited to the cortex region due to the short optical transmittance in brain (~1 mm) and the bulky optical system prevents the implantation without severe brain damages. On the other hand, electrical-based system[6]–[8] for detection of electrical and chemical signals is less invasive, which is an ideal tool

to monitor brain activities in deep brain regions. In addition, stimulation approaches including optogenetics[9], chemical deliveries[10] and electrical stimulation[11] are commonly used to manipulate brain activities for scientific studies as well as disease treatment. Therefore, an implantable miniaturized platform with electrodes and other stimulation modalities is needed to facilitate the understanding of brain functions in deep brain regions.
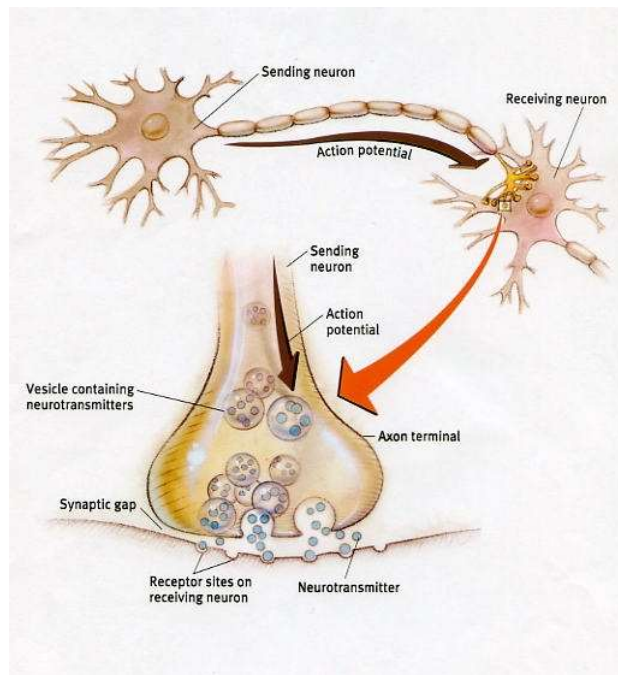
Figure 1.1 Neural signal propagation within and across neurons
(http://www.rhsmpsychology.com/Handouts/synapse.htm)

1.1 Electrochemical Biosensors

Signal propagation between neurons is accomplished by the movement of neurotransmitters across the synapse, where they are released by the pre-synaptic neuron and activate post-synaptic receptors. To date, over 100 types of neurotransmitters have been identified, which could influence the function of neurons through various mechanisms and control the electrical excitability of the post-synaptic neuron in two ways: excitatory

or inhibitory. Neurotransmitters play a significant role in modulating brain activities. Imbalance of neurotransmitters could lead to many neurological and psychiatric disorders including Alzheimer's disease, Huntington disease and Parkinson's disease[12]–[16]. Therefore, it is extremely important to monitor different neurotransmitters to understand both normal and abnormal brain activities.

Various technologies have been developed to detect neurotransmitters in deep brain. Microdialysis, as one of the most established methods, requires the insertion of a small catheter (microdialysis probe) into the brain. The microdialysis probe is composed of a liquid channel that is encapsulated by a semipermeable membrane, where small solutes can diffuse through and removed for downstream analysis (**Figure 1.2**)[17]. However, such
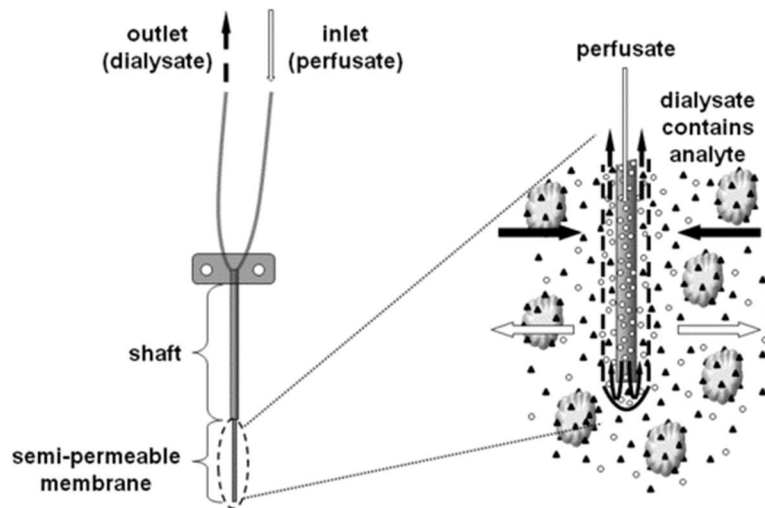
Figure 1.2 Schematic illustration of a microdialysis probe ("Microdialysis," *Wikipedia*)

approach suffers from low temporal (5-10 mins) and spatial (~mm) resolution, making it inapplicable for sophisticated behavioral studies[18]. Electrochemical sensing methods have been developed for neurotransmitters detection that provides millisecond-range

responses and micrometer-range resolution[12], such as fast scan cyclic voltammetry (FSCV)[19] and constant potential amperometry (CPA). However, these approaches face difficulties of detecting a limited number of neurotransmitters and inability to selectively sense the neurotransmitter of interest without interference from other molecules with the similar redox potentials [20]. As the major excitatory neurotransmitter, glutamate (Glut) is non-electroactive which cannot be measured using above approaches.

On the other hand, as demonstrated in Monbouquette lab and others[7], [8], [21], [22], non-electroactive species, such as glutamate and glucose, in biological tissue can be detected by coating the surface of electrodes with appropriate enzymes with near real-time response (~1 s) and micrometer scale spatial resolution. Oxidases are often used to selectively catalyze the formation of H_2O_2, which can be detected by electrooxidation to generate amperometric signals. Other polymers are coated to reject interferents utilizing mechanisms of size-based exclusion and charged-based repulsion to achieve selective detections. In this thesis, electrochemical sensing of
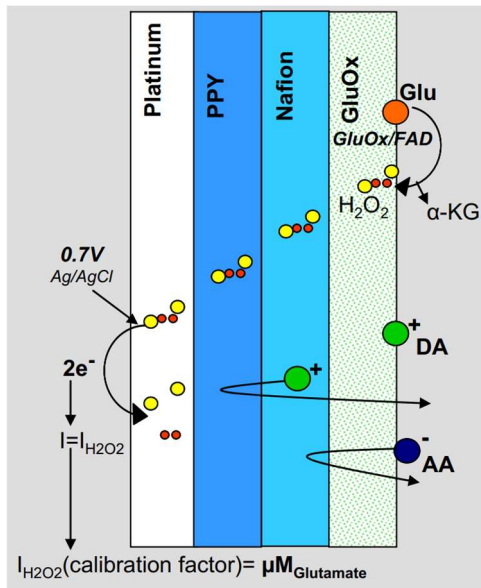
Figure 1.3 Schematic of glutamate sensors

neurotransmitters and glucose is used to validate the *in vivo* functionality of each platform.

4

1.2 Optogenetics

Optogenetics[9] is evolving rapidly due to its importance that could reveal questions no other method could. Optogenetics enables light control of neurons which have been genetically modified to be sensitive to light. The function is realized by making specific cells express microbial opsins, which is a kind of light-activable transmembrane proteins. Depending on the type of opsin, the neurons can be both activated and inhibited using light at different wavelength. **Figure 1.4** shows the most used opsins to depolarize and hyperpolarize the neurons[23]. Channelrhodopsin2 (Chr2) is commonly used to activate neurons with blue color (473nm) illumination. Halorhodopsin (Halo) and archaerhodopsin (Arch) are instead used to inhibit neurons with yellow color (570nm) and green color (520nm) illumination respectively. With this technology, people can target and control precisely defined events even in freely moving mammals[9].
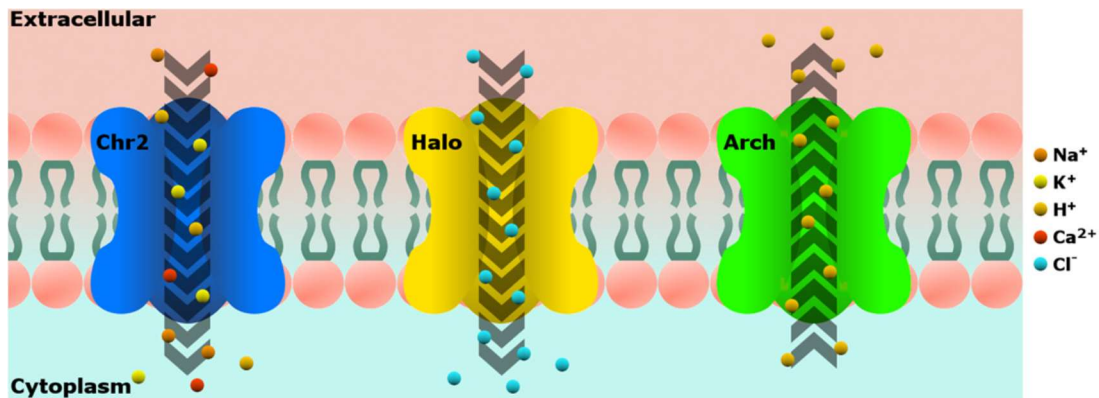
Figure 1.4 Schematic representation of microbial opsin used in optogenetics [23]

1.3 In vivo fluidic delivery

Delivery of fluid into certain brain region is another important tool in neuroscience studies to help understand complex neural circuits, neurochemical interactions and help

find treatments to brain diseases such as Parkinson's disease and brain tumors[24]. In vivo neuropharmacology is the study of how drugs affect brain functions and behaviors, which requires drug delivery directly into certain brain region, providing faster response, higher spatial resolution and not being blocked by blood-brain barriers (BBB) compared to other routes of administration such as oral and intravenous administration. In addition to traditional pharmacological agents, there is an increasing demand for delivery of other fluidic agents, such as gene therapy vectors[25] and antibody treatments for chronic diseases[26]. Moreover, fluidic delivery can activate or inhibit neural activities directly through chemical/neurotransmitter delivery or combined with other technologies such as optogenetics[9], [10] and chemogenetics[27], [28]. For example, chemicals such as pilocarpine hydrochloride and tetrodotoxin were infused locally into a mouse brain to increase and decrease the neural activities at CA1 in hippocampus[29]. For optogenetics applications, viral vectors need to be designed and injected into the targeted brain region to modify neurons to be sensitive to light. Chemogenetics (**Fig. 1.5**), similar to optogenetics, uses chemically engineered molecules, such as designer receptor exclusively activated by designer drugs (DREADD), and small molecules ligands, like clozapine N-oxide (CNO) instead of light-sensitive channels and light to manipulate specific brain circuits and populations, which requires fluidic injection of both viral vectors and ligands. Although chemogenetics has inferior temporal resolution compared to optogenetics, it is better performed to influence larger brain regions and easier to implement.
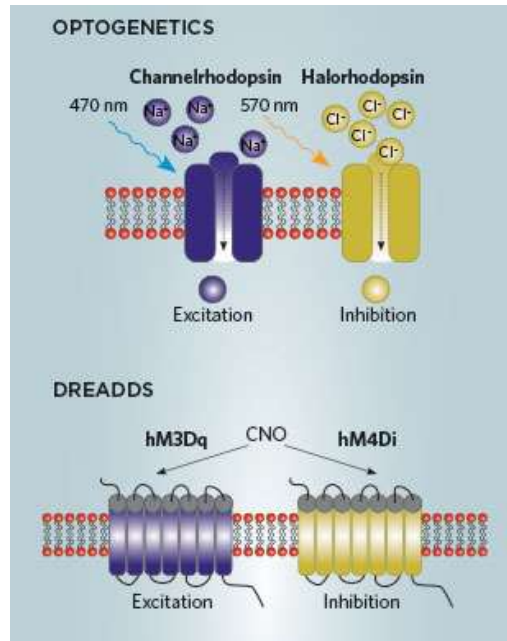
Figure 1.5 Optogenetics vs Chemogenetics

Current *in vivo* chemical delivery relies on decades-old use of metal cannulas[27] or microdialysis[30], whose scales are on the order of a few hundred micrometers (**Figure 1.6**). The large dimension leads to poor spatial precision to study brain microcircuits and cause significant brain damages. Therefore, people are pursuing innovative technologies with better spatiotemporal resolution, minimized tissue damage and integration with other tools.
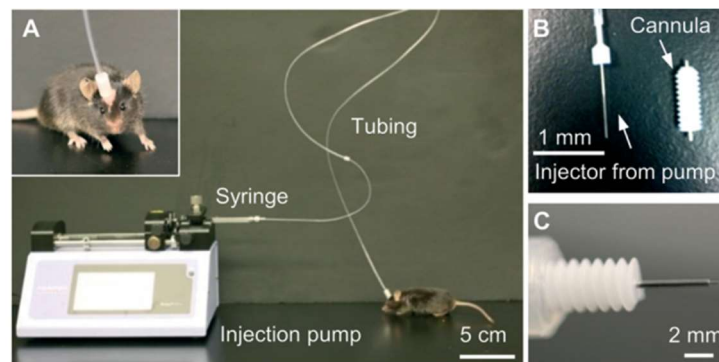
Figure 1.6 Conventional cannulation system

1.4 Development of Implantable Neural Probes for Neuroscience Study

Electrode-based implantable device was first made from insulated microwires in 1950s to record electrical signals from single neurons[31], which allowed neurophysiologists to study the activity of individual neuron in awake, free-moving animals. Since then, various technologies have been developed to improve the system, however the concept remains unchanged in the last few decades[32]. A tetrode (**Figure 1.5**) with four microwires is capable of detecting and separate individual neurons within a 50 μm radius, which contains ~100 neurons, using clustering methods. And neurons within the radius of 140 μm, which contains ~1,000 neurons, could also be detected without separation[33]. Microwire based devices are widely used and inexpensive. However, microwires have limited number of electrodes, which are all located at the tip, preventing the detection along the microwires simultaneously.
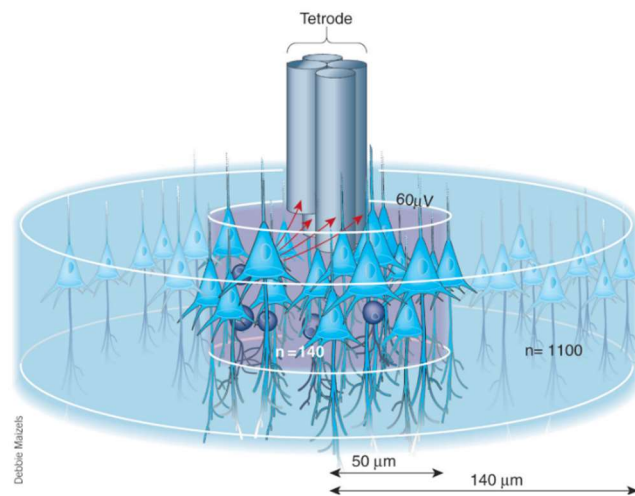
Figure 1.7 Schematic of electrophysiology recording from a tetrode

With the advancement of microfabrication technology, recording electrodes can be fabricated on silicon substrates with micron to nanometer scale precision. Since the first

development of planar Si probes by Wise *et al.*[34] from University of Michigan, efforts have been made to increase the number of electrode sites, minimize the device dimension, integrate with integrated circuits (ICs) and even create 3D probe arrays. These probes with planar Si structures are commonly known as Michigan probes or Michigan arrays. In a very recent work, a silicon probe with 960 sensing electrodes and fully integrated CMOS chip has been developed, which can detect more than 700 isolated single neurons simultaneously[35]. With 130-nm CMOS fabrication process, nearly 1,000 electrodes are placed on a single, 10-mm long, straight shank with 70×20-μm cross-section with multiple layers of wires connecting out. Recorded signals are processed, multiplexed and digitized directly by the IC for read-out (**Figure 1.6**). Probes with planar structures have a limited recording volume within 50 μm from the probe shank. Hence a three-dimensional probe arrays is needed to achieve neuron recordings from a larger volume, which is typically fabricated by stacking 2D planar probe arrays[6], [36]–[38]. The commonly used silicon-based microelectrodes arrays (MEAs) for electrochemical sensing also has the planar structure fabricated by microfabrication process to have precisely patterned sensing electrodes to achieve biosensing with high spatial resolution[7], [39].
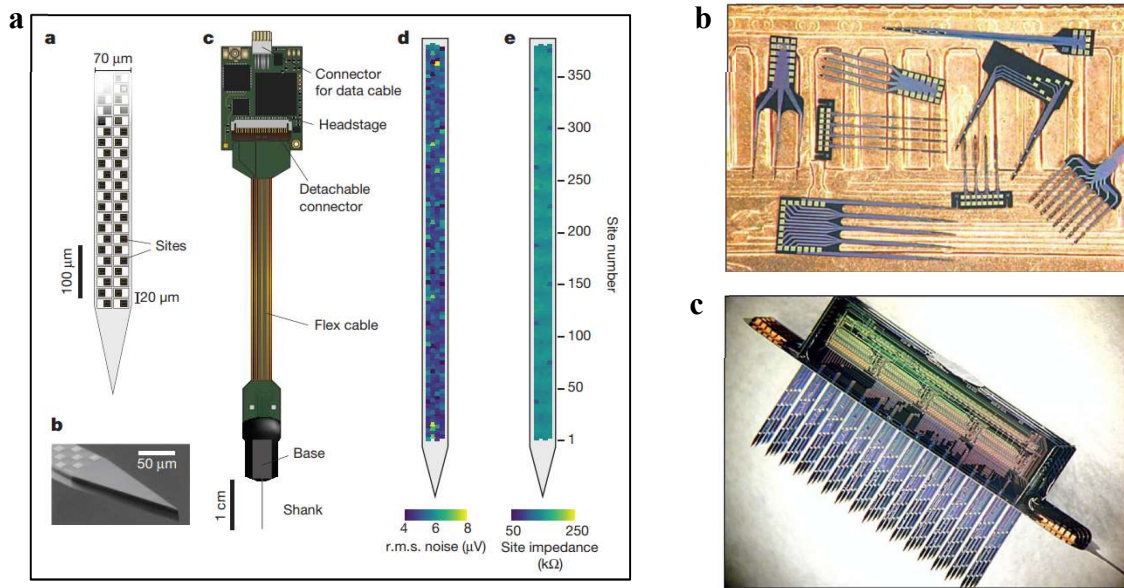
Figure 1.8 Advanced planar silicon probes. (a) Silicon probe with ultra-high density of electrodes[34], (b) Multi-shank probes and (c) 3D probe arrays[37]

In addition to the efforts of improving Si probes in terms of the electrodes density to record more and more neurons, another major direction in developing implantable neural probes is to incorporate more functions together for more complex experimental studies. As introduced in previous sections, the integration with optogenetics and chemical delivery functions would help answer questions that otherwise impossible.

The most straightforward approach for simultaneous electrical recording paired with optogenetics and/or chemical delivery is done by inserting multiple implants, such as a tetrode, an optical fiber and a metal cannula. However, the drawbacks are excessive wound size and poor alignment precision among these devices. Therefore, a compact integrated multifunctional system is needed to minimize brain damage caused by the implants and to achieve highly localized sensing and stimulation.

To date, there are two major approaches to make integrated light stimulation neural probes: (1) light delivery to the probe tip from outside through optical waveguide [40]–[43]

and (2) integrate light source (LEDs) directly on the probe [44]–[46] (**Figure 1.9**). Each approach has its own advantages and drawbacks. Waveguide approach uses external light source, which eliminates the heat production inside the brain, while it usually has relative large power loss especially at the waveguide input end, and such device is tethered with optical fiber which would restrict the movement of animals. μLEDs put at the probe tip could provide higher light power, and the all electrical system could be powered wirelessly. However, such devices are complicated to fabricate and will generate excessive heat inside brain especially for applications required high-power and long-duration illuminations[47].
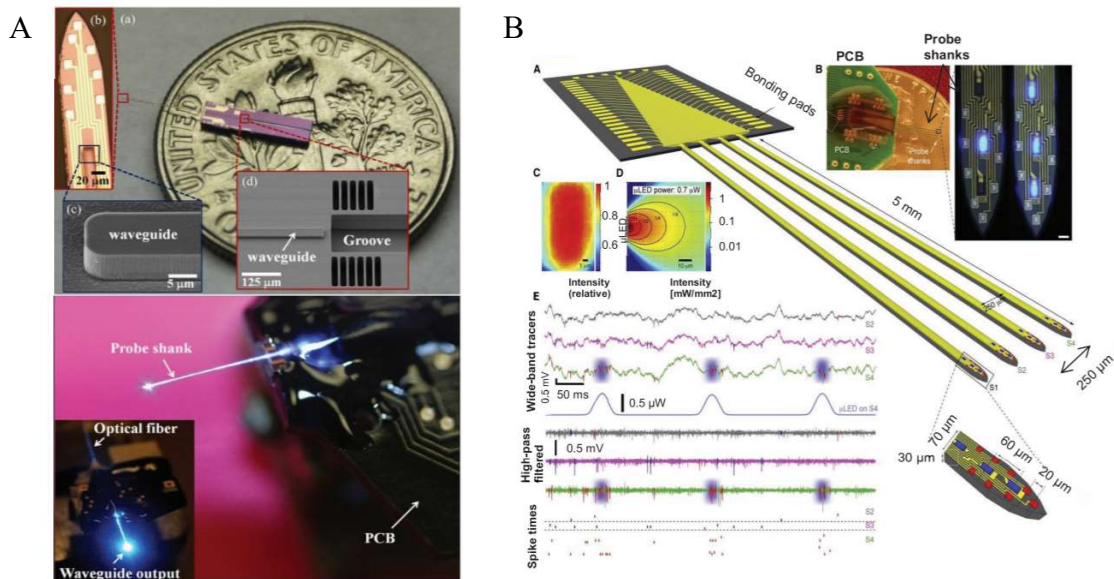
Figure 1.9 Reperesentative neural probe with optial stimulation based on (A) waveguide [40] and (B) on probe μLEDs[44].

The integration of microfluidic channel with Si neural probes is developed through surface micromachining[48]–[52] and bulk micromachining methods[29], [53]–[58] (**Figure 1.10**)[24]. In the case of surface micromachining, microfluidic channel is formed by first deposit and pattern a sacrificial layer (e.g. photoresist and SiO_2), followed by the coverage of another material (e.g. silicon nitride, silicon oxide, metals and polymers) to

11

form the top of the liquid channel. The channel is finished by removing the sacrificial material. In the case of bulk micromachining, microchannel is formed by the etching of bulk Si substrate followed by isotropic deposition or bonding of another layer to seal the channel.
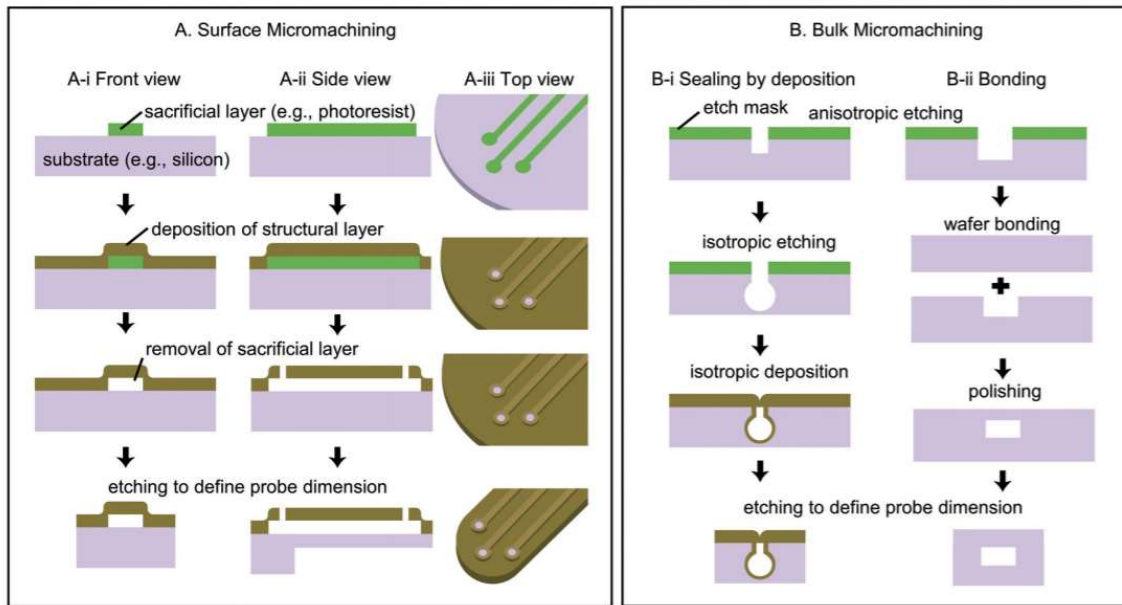
Figure 1.10 Representative fabrication processes of Si microfluidic neural probes [24]

Silicon neural probes are widely used due to the mature fabrication technologies from MEMS and CMOS processes. Such devices are great tools for acute and short-term applications, however, electrical recordings with increasing noise levels, decreasing signal amplitude and loss of detected neurons are often observed[59]–[61]. It is believed that the mechanical mismatch and micromotion between rigid silicon (E = 130-170 GPa) and soft neural tissues (E = 0.1-6 kPa) could leads to neuron loss and scar formation near the implants due to neuroinflammation response[62]–[64]. Therefore, there is a major motivation to develop polymer-based soft and flexible neural probes that could prolong the lifetime of the implants and minimize foreign body reactions and brain damages. Two

major strategies are taken to match the mechanical properties of neural tissues. The first one is to use softer material such as Parylene C, polyimide, SU-8 and PDMS as probe substrate[65]–[69]. And the second approach is to use stiff material but with dimension close to cell size (1-10 μm) [70]–[73]. Cases with improved chronic performance have been reported using both approaches. Nguyen et al.[68] reported neural probes made from soft polymer (E = 12 MPa) and observed nearly complete attenuation of inflammatory response and absence of neuron loss around the implant at week 16. Zhou et al.[74] compared SU-8-based ultrasmall meshed structure with polyimide probe (E = 2.5 GPa) and showed less inflammation and higher neuron populations.
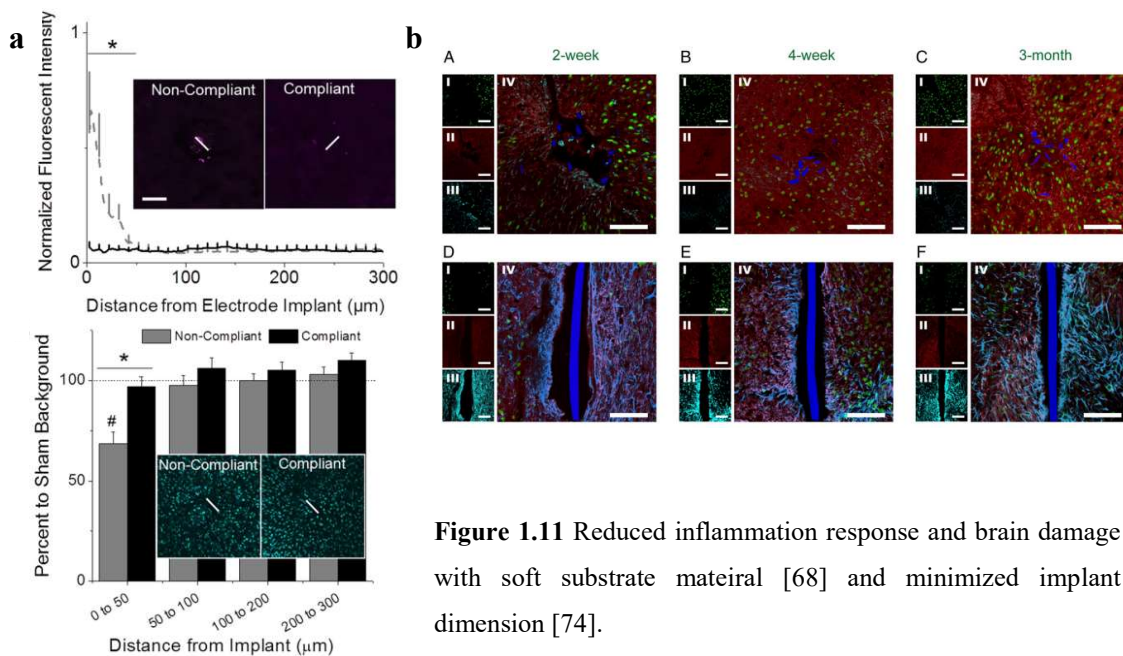
Figure 1.11 Reduced inflammation response and brain damage with soft substrate mateiral [68] and minimized implant dimension [74].

The two primary objectives for the work described in the thesis are (1) integrating optical stimulation and chemical delivery functions on silicon probes to increase the functionality of the current silicon MEAs for electrochemical sensing; and (2) developing

a completely new ultrasoft PDMS-based neural probes with new implantation strategy aiming to reduce neuroinflammation response and brain damage.

Chapter 2

Silicon neural probes with integrated optical waveguide

2.1 Introduction

Neural probes enable monitoring of local brain activities in both electrical and chemical ways, which is one of the most important tools to study brain functions in deep brain regions. However, neuroscience study can be more effective by using stimulation modalities while monitoring neuronal response and animal behavior changes to identify the functionality of a brain circuit [75]. Among various stimulation modalities, optogenetics provides both activation and inhibition of neurons with high spatial and temporal resolution that makes it a unique tool in neuroscience studies.

In the early stage of combined optogenetics and electrical recording, commercially available components such as microwires, silicon neural probes and optical fibers were manually aligned and glued[76], [77]. The components are readily available to enable such studies right away, however, the relative distance between each component would be hard to control. In addition, such tools would create large brain damages due to the bulky size of optical fibers (~200 μm).

MEMS technology can not only enable micron-scale patterning, but is also capable of forming active (LEDs) and passive (waveguides) optical components by depositing and patterning layers of films or transferring from another substrate[44], [45], [78]. LED integrated neural probes provide advantages including high scalability and wireless capability, however, also have limitations including heat generation inside the brain, crosstalk between the driving circuits for the LEDs and electrical recordings, limited wavelength selection and incompatible fabrication processes. On the other hand, optical waveguides can be integrated monolithically using standard MEMS fabrication, without heating effects since the light source is out of the probe[47], which make it more suitable for applications with high power and long duration stimulations. Several silicon neural probes with optical waveguides have been demonstrated for electrophysiology recording[40], [79], however, combining optogenetics with electrochemical sensing using integrated silicon probes have not been demonstrated.

We designed and fabricated silicon-based probes with integrated PECVD Si_xN_y waveguides and grating couplers to deliver light from a single mode fiber to the probe tip. Light is emitted from the center of a sensing electrode perpendicular to the probe surface, enabling highly localized optical stimulation to neurons just above the sensing electrode. The PECVD Si_xN_y waveguide was optimized to have low absorption to blue light (450 nm), and capable of deliver ~40 μW of light to the tip with 2 mW input light power from an optical fiber. We validated the device by detecting optically-evoked glutamate release in anesthetized rats' nucleus accumbens several weeks after injection of channelrhodopsin-expressing AAV into the above regions.

2.2 Design

The waveguide integrated neural probe is based on the silicon-based MEAs for biosensing developed by Monbouquette lab[7], [39]. The probe thickness is defined by the thickness of the 4" silicon wafer,150 μm, which is smallest thickness that can be handled without cracking. The probe shank is 9mm long with a tapered width from ~400μm at the probe base down to 144μm at the probe tip. The probe consists of two Pt electrodes and a light stimulation site. The electrodes are designed to have the same surface area as in a prior work to satisfy the electrochemical sensitivity requirement[21]. Silicon nitride was chosen as the waveguide material due to its relatively large refractive index (~2) so that light can be better confined inside the core for denser integration. We deposited 200nm thin silicon nitride to avoid excess stress issue and reduce the deposition time. The waveguide is slightly tapered with width from 50 μm at the input port to 20 μm at the output port. Due to the extremely thin waveguide structure, butt-coupling method would have significantly large coupling loss, which is not applicable in our device. Instead, we decided to use grating couplers (GCs) for both input and output coupling, which could give much higher coupling efficiency in theory (**Figure 2.1**).
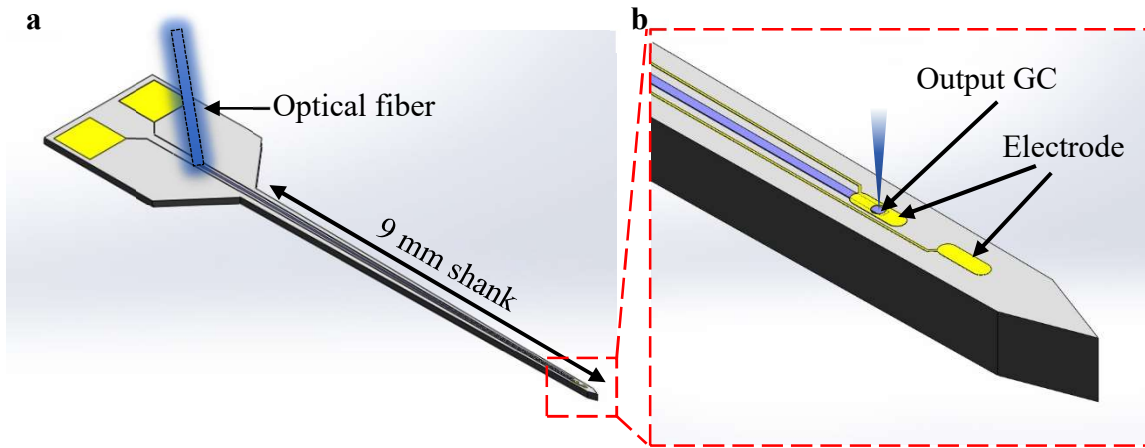
Figure 2.1 Schematics of the waveguide integrated silicon neural probe. (a) 3D schematics of the overall probe design. (b) Probe tip showing 2 electrodes and 1 light stimulation site.

Grating couplers are designed using 2D Finite-Difference Time-Domain (FDTD) approach (RSOFT) to couple 450 nm wavelength blue light into the waveguide with an input coupling angle of 10º and a vertical output coupling. The GCs were finalized with the following parameters:

input GCs: grating period $\lambda = 300$ nm, etch depth d = 100 nm, duty cycle $\eta = 50\%$

output GCs: grating period $\lambda = 270$ nm, etch depth d = 100 nm, duty cycle $\eta = 50\%$

which led to an input coupling efficiency of 13%, and output coupling efficiency of 50%.
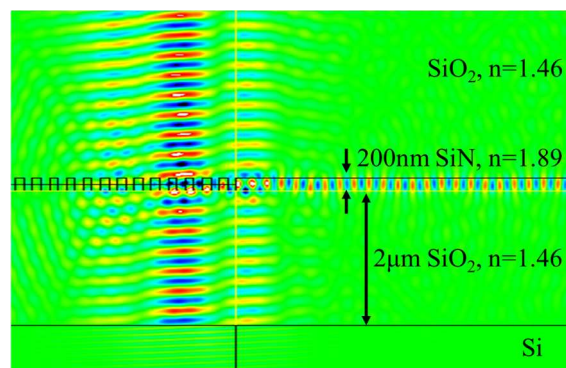
Figure 2.2 FDTD Simulation of input grating couplers

2.2 Fabrication process

The fabrication process is summarized below (**Figure 2.3**). We first grew a 2 μm thermal oxide film on a 150μm-thick Si wafer as the bottom cladding, which was sufficiently thick to prevent leakage loss towards the silicon substrate[80]. A 200nm silicon nitride was deposited by PECVD by optimized NH_3/SiH_4 ratio of 9:1 to minimize the waveguide loss. The grating couplers and the waveguide were patterned by e-beam lithography and photolithography processes, and etched by RIE (**Figure 2.4a**). Finally, a 1μm PECVD silicon dioxide film was deposited as the top cladding. Electrodes and interconnections (Cr/Pt 10nm/100nm) were fabricated on top of the cladding oxide layer by lift-off process. Another layer of silicon dioxide was deposited on top of the electrodes as an insulation layer, and the electrodes were opened by RIE etching. The probes were released from the silicon wafer using deep-RIE process for assembly and testing (**Figure 2.4b**).

Si   SiO$_2$ SiN   Pt

(a)

(b)

(c)

(d)
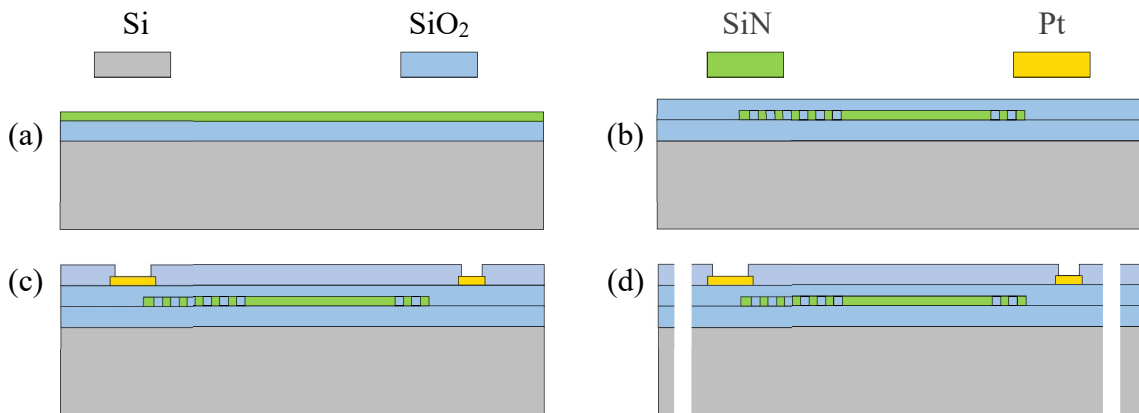
Figure 2.3 Process flow. (**a**) Deposition of 2 μm SiO$_2$ and 200 nm Si$_x$N$_y$ using thermal oxidation and PECVD. (**b**) Pattern Si$_x$N$_y$ grating couplers and waveguides using e-beam lithography and contact lithography followed by RIE etching and deposition of top cladding layer. (**c**) Pattern metal layer using lift-off process, followed by deposition of insulating SiO$_2$ layer. (**d**) Release probes from the substrate using DRIE process.
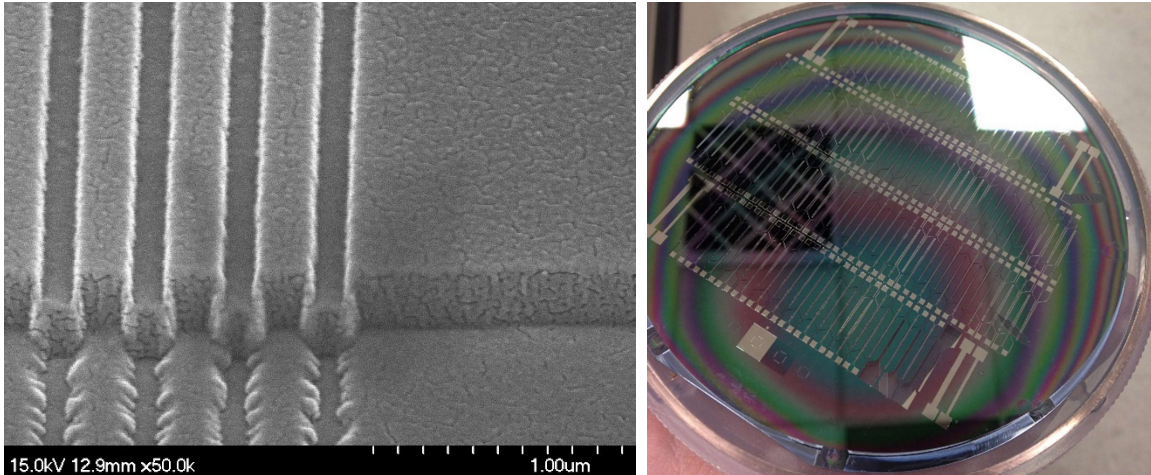
Figure 2.4 Fabricated structures. (**a**) SEM of a patterned grating coupler with 100nm etch depth and 360nm period. (**b**) Released probes on a 4" silicon wafer.

2.3 Optimization of PECVD Si$_x$N$_y$ film for reduced blue light absorption

Since the most used opsin, Channelrhodopsin-2, is stimulated efficiently in the blue light range, with the peak absorption at 480 nm [81], the optical waveguide should have good performance in this range. However, it is very challenging since the light absorption typically increases at smaller wavelength (blue/UV). LPCVD stoichiometric Si$_3$N$_4$ film has been demonstrated to have low absorption in visible light range [80], [82], however, exhibited huge waveguide propagation loss in our trials, which might be due to the poor stoichiometry. Instead, PECVD Si$_x$N$_y$ provides higher flexibility in tuning the material properties by changing the gas ratio between NH$_3$ and SiH$_4$ and the plasma frequency. Increasing the flow rate of NH$_3$ relative to SiH$_4$ led to a decrease in the refractive index of the nitride film (**Figure 2.5**), as an indicator of reduced absorption coefficient in visible light range. As demonstrated in reference [83], the waveguide loss was minimized when the refractive index is less than 1.90 at 532 nm wavelength, which corresponds to gas ratio

20

of $NH_3/SiH_4 > 2$ deposited by STS-PECVD at 380kHz plasma frequency. Gas ratio of 9:1 was used to fabricate the waveguide on the probe, which has a refractive index of 1.867 at 532 nm and 1.882 at 450nm.
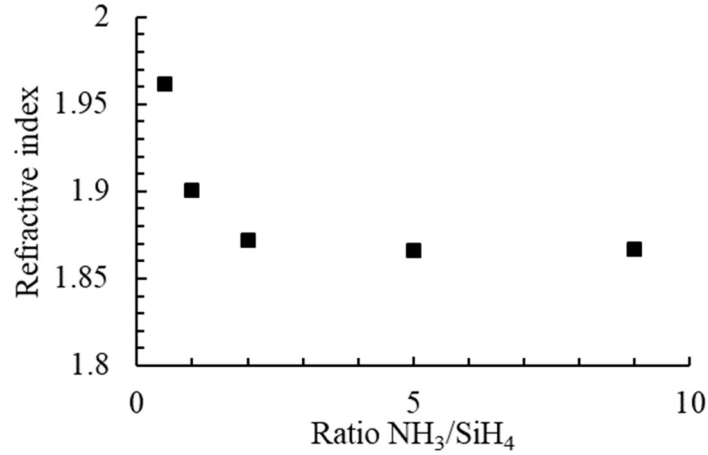
Figure 2.5 Refractive index (λ=532 nm) decreases as the ratio between NH_3 and SiH_4 increases.

2.4 Results

After releasing, a pigtailed laser diode (Wavespectrum Laser Group Limited) connecting to a polarization-maintaining fiber (PM-S405-XP, Thorlabs) was aligned to the input grating coupler, while the output power was collected by a 200 μm multimode fiber and measured by a photodetector (**Figure 2.6**). The waveguide loss was measured by a direct cut-back method, and yielded a propagation loss of ~ 3dB/cm. The maximum output power measured at the output grating coupler was ~40 μW with an input light power of 2 mW, which yielded a total light delivery efficiency of 2%. The loss consisted of three major components, (1) input grating coupler (~8% efficiency, 11dB loss), (2) waveguide loss (~50%, 3dB loss), and (3) output grating coupler (50%, 3dB loss). The mismatch between the simulated and the measured input coupling efficiency could come from the errors in the film thickness deposited in each step and the etch depth of the grating couplers. It is

generally accepted that the light intensity threshold for stimulating Channelrhodopsin-2 is ~1 mW/mm², and several experiments have reported intensity less than 0.1 mW/mm² would be sufficient for stimulation. In our case, the dimension of the output grating coupler was 20 × 20 μm, while most of the light was emitted within 10 μm along the light propagation direction. Therefore, the light intensity above the GC can be calculated as $40\mu W/(20\mu m \times 10\mu m) = 200\ mW/mm^2$, which is sufficient to stimulate the neurons sitting right above the GCs.
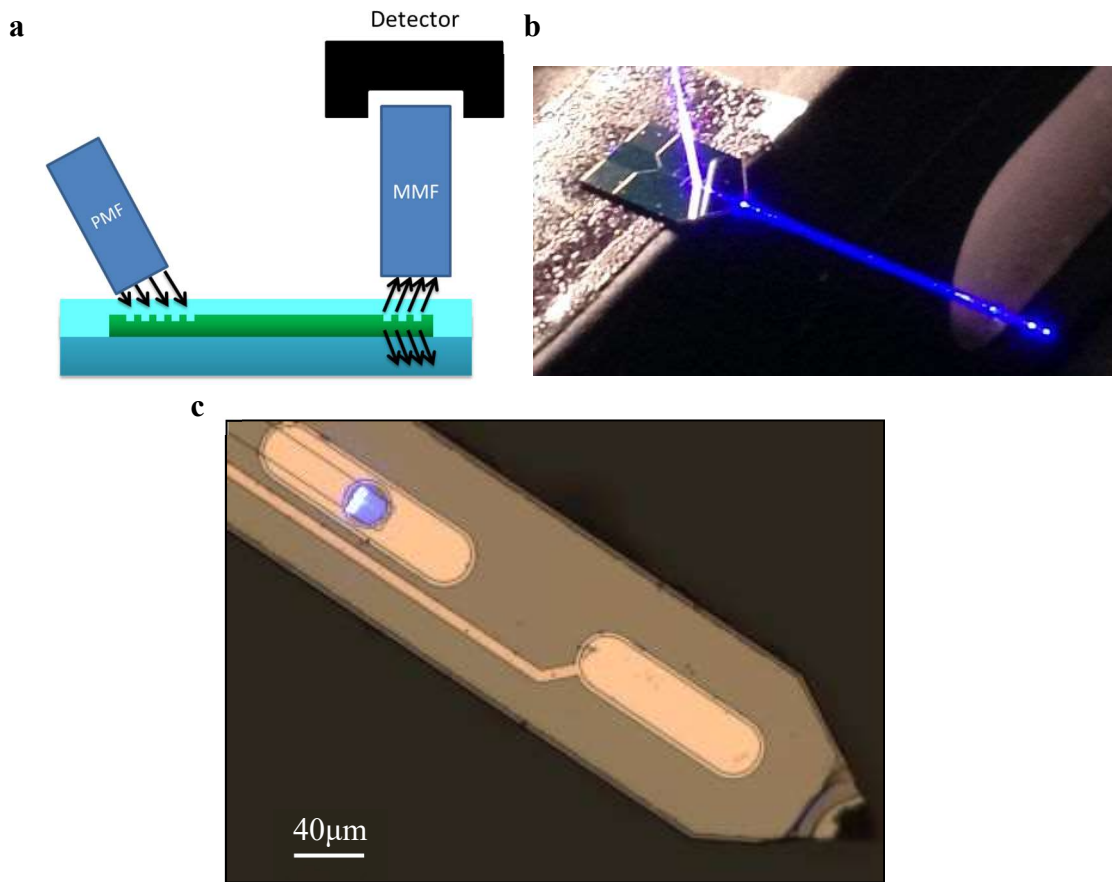
Figure 2.6 Optical setup for optical fiber alignment and light power measurement. (**a**) Schematics of the optical setup. (**b**) Light coupling into the waveguide after aligning the optical fiber to the input grating coupler. (**c**) Light emitting from the GC at the center of a sensing electrode. Most of the light was emitted within first 10 μm length along the light propagation direction.

To fix the position of the optical fiber on the probe, a transparent epoxy (E-30CL, Loctite) was used for initial fixation of the probe tip. The coupling angle in epoxy is different than that in air, due to the higher refractive index of ~1.5, and can be calculated by Snell's law (**Figure 2.7**).

$$n_0 \sin \theta_0 = n_1 \sin \theta_1 \, , n_0 \sin \theta_0 = n_2 \sin \theta_2$$

$$\Rightarrow n_2 \sin \theta_2 = n_1 \sin \theta_1$$

Therefore, the angle of the optical fiber should be changed to 6.65° for an incident angle of 10° in air.

Before aligning the optical fiber, the probe was mounted on a customized holder, so that more epoxy can be contained to increase the robustness of the package. After aligning the optical fiber to the GC, epoxy was used to pre-fix the fiber tip to the GC. To avoid fiber movement due to the epoxy shrinkage during the curing process, minimum volume of epoxy should be used and was done by dip coating the fiber into a drop of epoxy and then aligning to the GC. After epoxy cured, large volume of dental cement was applied to form a more stable packaging (**Figure 2.8**).
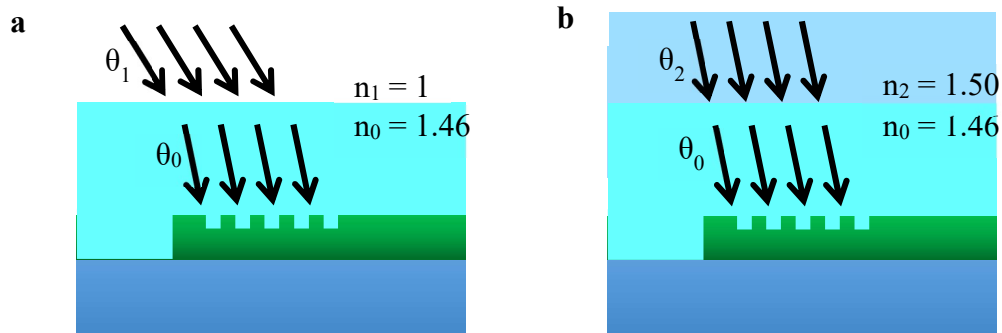
Figure 2.7 Alignment of optical fiber to GCs (**a**) with and (**b**) without epoxy.
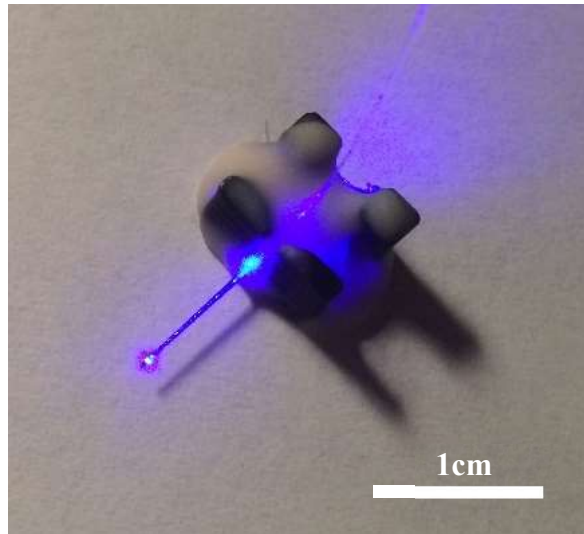
Figure 2.8 Image of a packaged probe with light delivery to the probe tip

The vertical illumination property was confirmed by immerse the probe tip in a dye solution. As shown in **Figure 2.9**, light was emitted almost vertically from the probe surface, with an angle of ~3° emitting backwards from the probe tip, which came from the fabrication error in the film thickness and GC etching depth. The light emitted from GCs has a small beam divergence angle, which potentially enables deeper penetration into the tissue.
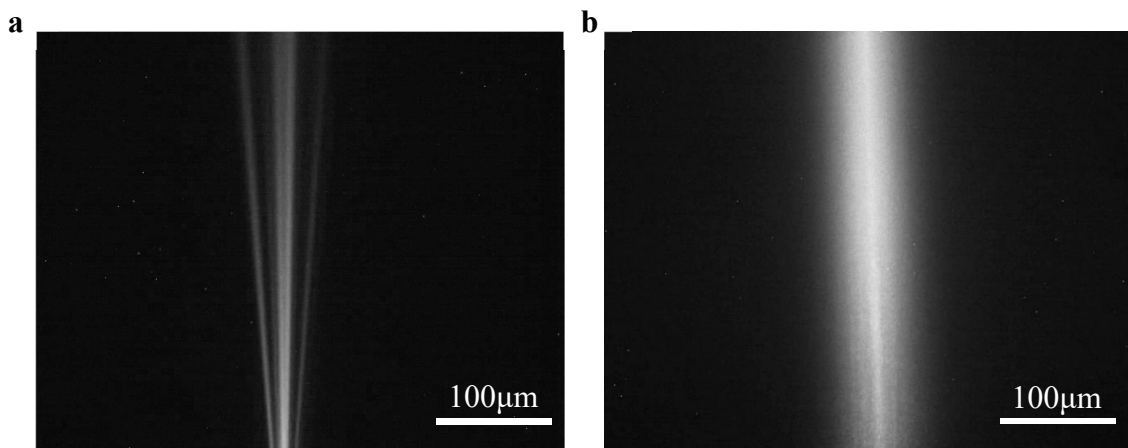
Figure 2.9 Light illumination pattern taken in a dye solution. (**a**) Front view. (**b**) Side view.

Channelrhodopsin-expressing AAV was injected to mPFC region of rats and waited for several weeks for the expression of ChR2 at nucleus accumbens (NAc). During the surgery, the probe was inserted to the NAc. Light power of 29μW was used for stimulation, which was calibrated before the experiment. The stimulation was conducted at 120Hz with a duration of 2s. **Figure 2.10** shows the result of detected light-induced glutamate release. The light stimulation site was in the center of the channel 1 sensor. The black line represents the detected glutamate release to light stimulation of neurons with ChR2 expression. To determine the level of light artifact, the probe was then implanted to the contralateral NAc, where neurons do not have ChR2 expression. Light stimulation was performed in the contralateral NAc using the same parameters, and resulted in a much lower signal level, and a sharp drop upon the end of the stimulation (Gray line). Subtracting the two lines, we got an artifact free glutamate sensing curve with a peak concentration of 40μM, with a gradual glutamate decay to the baseline level, representing the glutamate uptake by surrounding neurons. It should be noted that Ch 2 did not show obvious glutamate level change other than noise, which may come from the LED controller, indicating the light stimulation was highly localized and did not affect the neurons near the other electrode 100 μm away.
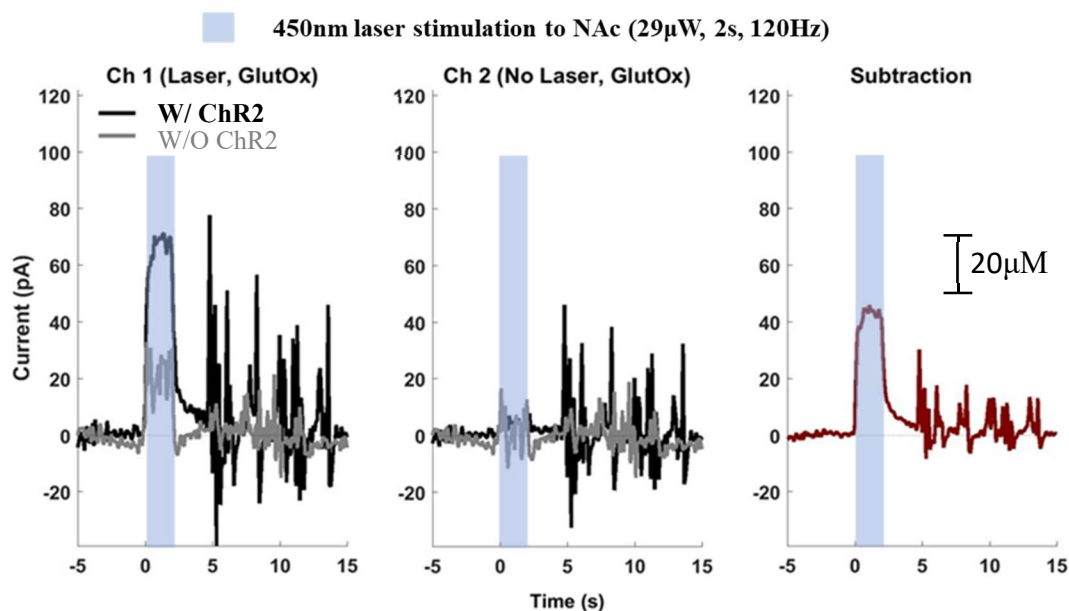
Figure 2.10 In vivo responses collected from the biosensor incorporated with waveguide. The darker line is the response collected in the NAc expressing channelrhodopsin (ChR2). The lighter line is the response collected in the contralateral NAc without ChR2. Injection site: mPFC.

2.5 Discussion

Optogenetics is the most attractive technology to manipulate neural activities with extremely high spatial and temporal resolutions, which offers unparalleled advantages as compared with conventional electrical stimulation. At the same time, monitoring of chemical signals, such as neurotransmitters, provides invaluable insights about how neurons communicate with each other. The combination of these two technologies (closed-loop optogenetics) would enable enormous researches to dissect neural circuits and cellular signaling and advance understandings of not only normal, but also many abnormal behaviors apparent in neurological and psychiatric disorders. However, a miniaturized neural probe with integrated functions of optical stimulation and electrochemical sensing has not been demonstrated and validated *in vivo*.

In this study, we developed a new proof-of-concept neural probe with integrated optical waveguide and electrochemical sensing electrodes. The initial *in vivo* validation experiments demonstrated promising results of light-induced glutamate release with light power of 29 µW. Although there were some artifacts superimposed on the real signals, we were able to subtract them out from the pure artifact signal detected from the contralateral brain region without the ChR2 expression to get a pure chemical signal.

A localized directional illumination pattern from the center of the sensing electrode and perpendicular to the probe surface was realized by using grating couplers to make sure the stimulation zone is well matched to the recording zone. Since the light was emitted through the transparent window in the center of the electrode, no light was directly illuminated onto the electrode, which could possibly reduce the level of light-induced artifacts to be low enough to recover the real signal. However, grating couplers are very sensitive to fabrication errors, such as the thickness of the bottom oxide, refractive index of the waveguide material, the duty cycle of grating couplers and grating etch depth, which would affect the efficiency significantly. In the future, optimization could be done after the deposition of bottom oxide and silicon nitride layer so that the fabricated structure would be better matched to the simulation design.

Chapter 3

Silicon neural probes with integrated microfluidic channel

3.1 Introduction

Neural probes are one of the most important tools in neuroscience studies that enable recording of neural activities (electrical[1], [38], [75] and chemical[7], [21], [39]) in deep brain regions with high temporal and spatial resolutions. At the same time, various stimulation modalities, such as electrical, optical and chemical, are commonly used to manipulate neural circuits and animal behaviors for various purposes, such as to identify the function of the specific neural circuits, to repair/restore sensory or motor function and to treat disease[10], [85], [86]. Among these stimulation modalities, chemical delivery is of great interest for both fundamental neuroscience research[85] and clinical medicine[10], [87]. Combining the chemical delivery with recording function enables simultaneous observation of neural activities in response to the chemical/drugs, which would help study complex nervous system[24] and assess the efficacy of new pharmaceutical drugs[29].

The most commonly used approach relies on implanting separate or assembled metal cannula and neural probes, which causes huge damage to the targeted brain region

due to the large footprint size. Moreover, the distance between the liquid channel and electrodes is hard to control, leading to poor experiment repeatability. Therefore, with the advances of MEMS technology, various silicon probes with integrated microfluidic channels (chemtrodes) have been developed using bulk or surface micromachining[24]. For bulk micromachining, the channel is formed by etching the silicon substrate and sealed by either deposition of isotropically grown materials such as PECVD oxide and nitride[56] or wafer bonding[29], [54]. For surface micromachining, the channel is formed by removal of sacrificial film deposited on top of the silicon substrate[52]. The silicon chemtrodes can be batch fabricated with high precision, however often involve complicated fabrication processes such as wafer bonding, polishing, deposition and etching of many films. The process to fabricate fluidic channels is often more complicated than the fabrication of electrodes.

In this work, we developed a customized PDMS thin-film transfer process based on conventional soft lithography technology that enable easy microfluidic channel integration on conventional silicon probes. Thin PDMS channels can be easily transferred to existing neural probes as an add-on module that could enable highly localized chemical delivery immediately. The process can also be applied to wafer-level fabrication to integrate microfluidic channels to hundreds of probes in parallel. PDMS microfluidic channel with a total thickness of 15 μm, and a channel dimension of 10×20 μm (thickness $\times$ width) was fabricated that enables precise chemical delivery at flow rates ranging from 0.25 to 1.75 μL/min with pumping pressure from 5 to 20 Psi. The proposed microfluidic neural probe was validated in rats with simultaneous chemical delivery and electrochemical sensing that proved the viability of the PDMS/Si hybrid chemtrode.

3.2 Design

The microfluidic channel is designed to be integrated to the existing silicon-based probes[7], [21], [39], [88] to enable simultaneous chemical (e.g. neural transmitters) delivery and electrochemical sensing capabilities at the same time to provide a method to validate the in-vivo functionality of a specific biosensor as well as to study fundamental neuroscience. To demonstrate the capability of the fabrication process, microfluidic channels were added to both front and back side of the silicon probe, and the latter case was characterized and tested *in vitro* and *in vivo*.

Microfluidic channel was first integrated with the optogenetics probe described in chapter 2 to achieve 3-in-1 multifunctional neural probes (**Figure 3.1**). The fluidic channel was transferred to the front side of the probe with liquid outlet 40 μm away from the top electrode. Due to the limited space on the front side of the probe, the fluidic channel was routed to an extension platform out of the probe for inlet connection. Two layers of PDMS thin-films were transferred, where the 10 μm-thick bottom layer was used to prevent leakage from the interface between the probe and outside platform. The top layer contained a 9 mm × 20 μm × 10 μm (length × width × height) channel and a 5 μm-thick cover.

Microfluidic channel was also transferred to the backside of the traditional silicon-based biosensors (**Figure 3.2**). Since there were plenty of room on the backside for inlet connection, one layer of PDMS thin-film with channel was transferred directly to the probe surface to form an enclosed channel, with the silicon probe itself as the channel bottom surface and PDMS as the cover. It also eliminated the need for the fabrication of the extension platform, which made the fabrication more straightforward. As suggested by Chen *et al.*[89], the fluid outlet with a diameter of 40 μm was placed on top of the PDMS

membrane instead of facing forward towards the probe tip to avoid channel occlusion during the probe insertion process. The liquid outlet was placed on the backside of the probe, right beneath the center point of the four electrodes. Same as the first design, the channel is 9 mm-long with a cross-sectional dimension of 20×10 μm.
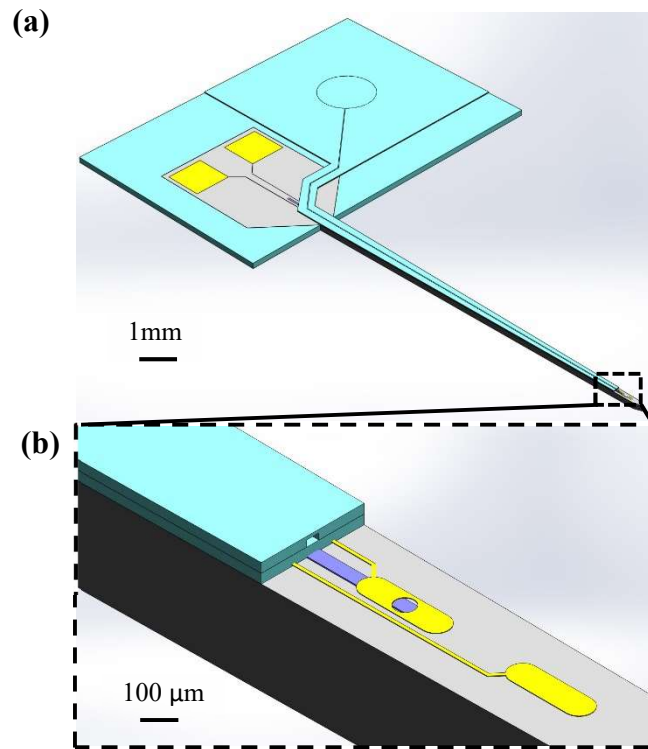
Figure 3.1 Schematic diagrams of a optogenetics probe with integrated microfluidic channel on the front side of the probe. (**a**) Overview of the structure. (**b**) Enlarged view of the probe tip showing the electrodes, waveguide and liquid channel.
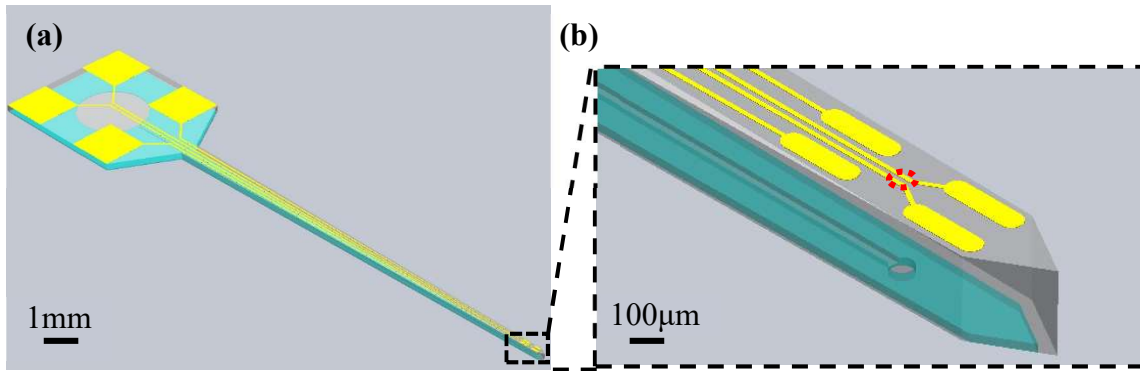
Figure 3.2 Schematic diagrams of a silicon probe with integrated microfluidic channel on the backside. (**a**) Overview of the structure. (**b**) Enlarged view of the probe tip showing the electrodes and liquid channel.

3.3 PDMS Thin-film Transfer Process

A customized PDMS thin-film transfer process was developed based on previously reported process[90], with higher yield, efficiency and alignment accuracy. The process of fabricating the two-layer microfluidic channel on the front surface of silicon probe is illustrated in **Figure 3.3** as an example. Instead of SU-8, silicon wafers were processed as molds due to the flat top surface even with multiple-layer structure, which is critical in the following pressing process. Masked by photoresist and silicon dioxide together, we were able to fabricate silicon molds with two etching depth, creating more complex structures with one molding/demolding process, such as creating isolated ultra-thin microfluidic channels with one transfer process. Otherwise, we would need to transfer a thin-film with a trench and then transfer a cover separately. Single-layer SU-8 mold tends to have ~1-2 µm height different across the wafer, which is even worse for double-layer SU-8 mold. Using silicon molds, the chance of having large-area uniformly pressed film was

significantly increased. Silicon molds with even more etching depth are also possible to make by incorporating other materials as etching masks, such as silicon nitride.
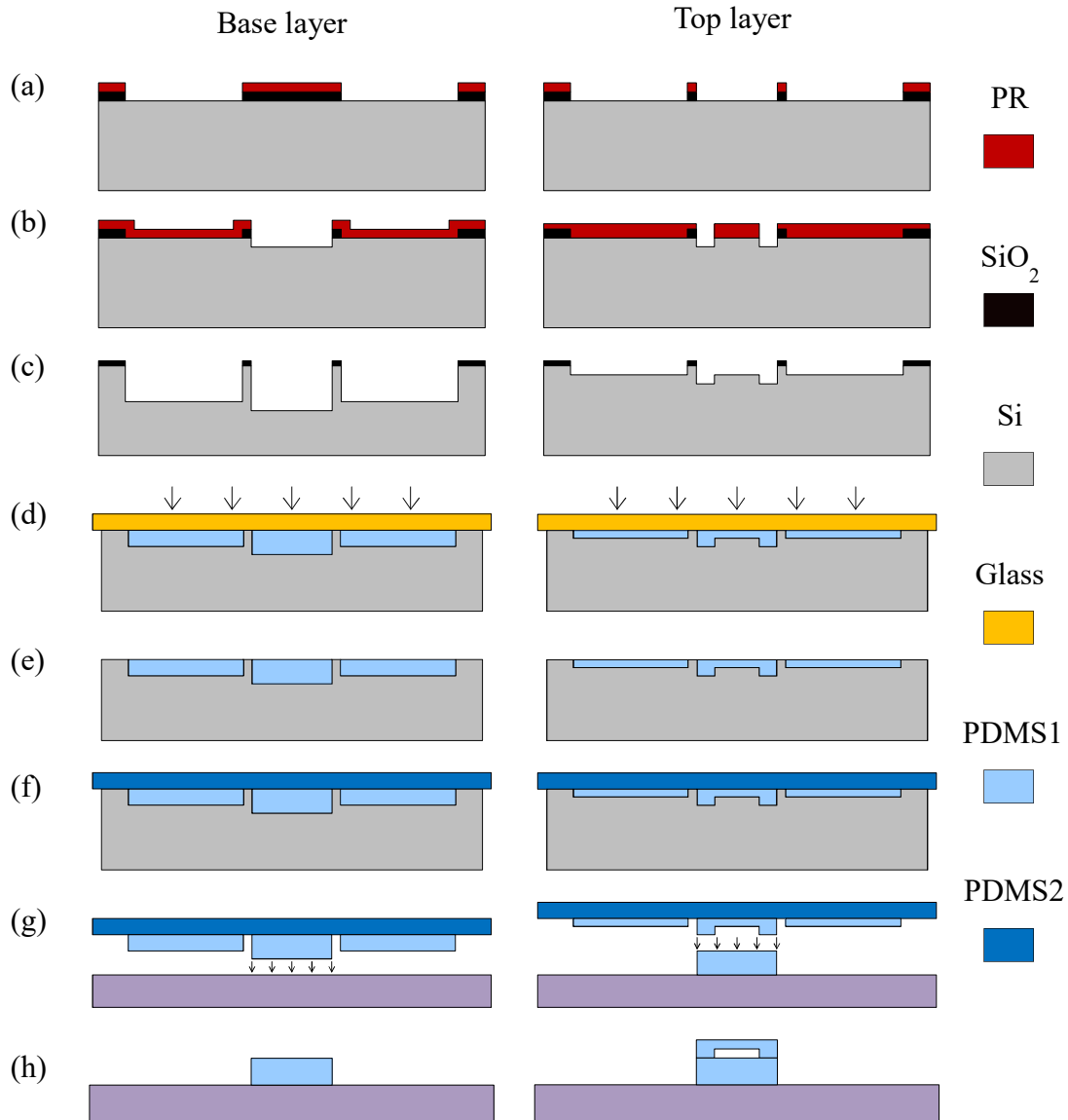
Figure 3.3 Process flow of the PDMS thin-film transfer process

The detailed fabrication process is described below:

1. The silicon molds were fabricated using the standard MEMS fabrication process with two photolithography, one RIE etching process to remove

silicon dioxide and two DRIE process to create two etching depth into the silicon wafer (**Figure 3.3a-c**).

2. After mold fabrication (**Figure 3.3c**), the molds were treated with trichloro-IJ1H,1H,2H,2H-perfluorooctyl)silane (97%, SigmaAldrich, USA). This surface treatment was carried out in a vacuum chamber at a pressure of -30 Psi for overnight. 3 µL of silane was added into the vacuum chamber, which is critical to achieve a relatively strong adhesion between PDMS and silicon molds.

3. Next (**Figure 3.3d**), freshly made PDMS was poured into the mold and pressed by a silane coated glass at room temperature to unwanted thermal expansion in PDMS. PDMS was prepared by first mixing 10 g pre-polymer with 10 µL Pt catalyst (PLATINUM-DIVINYLTETRAMETHYLDISILOXANE COMPLEX; 2% Pt in xylene; Gelest, Inc) and then mixing with 1 g of cross-linker. Pt catalyst was used to speed up the curing process at room temperature (~6 hours). Glass were coated with silane using the same procedure described above, however with much higher silane volume of 20 µL to lower the adhesion force between the PDMS thin-film and the glass. A PDMS buffer was placed on top of the silane treated glass and then covered by another regular glass. Then, a large pressure was applied to the glass to press the uncured PDMS out of the mold. The pressure can be applied using heavy weight (20 kg) or from a pressure source.

4. After PDMS curing (~6 hours in room temperature), the silane coated glass

was peeled off. The PDMS thin-film was left inside the mold due to the stronger adhesion force between the PDMS and silicon molds compared to the force between PDMS and the silane coated glass (**Figure 3.3e**).

5. Another layer of PDMS (same as described above) was poured on top of the PDMS thin-film and covered by a silane-coated glass separated by a spacer (~3 mm). After PDMS curing (~6 hours), the PDMS thin-film can be detached from the mold by peeling the top glass slide (**Figure 3.3f, g**). The second PDMS layer was needed to achieve better bonding results, while the glass backing was used to make sure that there would be no deformation of the PDMS layer to achieve highly precise alignment (<5 μm).

6. The PDMS film was then bonded to the substrate (silicon, oxide or PDMS) using oxygen plasma (500mT, 80W, 30s; Technics MICRO-RIE, SERIES 800). The alignment was performed using a Quintel mask aligner.

7. After alignment and bonding, the device was baked in oven at ~65 ºC for >1 hour to achieve better bonding strength before peeling off the second PDMS layer. The thick PDMS layer can be removed easily, leaving the thin-film bonded to the substrate. The relatively poor adhesion between these two PDMS layer is presumably due to the silane residue on the PDMS thin-film during the pressing process by the silane coated glass. When lower adhesion is required, the PDMS thin-film can be coated with silane with very low volume and time (e.g. 1 μL, 10min). It should be noted that the ultimate bonding strength (>60 Psi) is usually achieved after 6 hours baking in oven at 65 ºC.

Figure 3.4 shows the transferred microfluidic channel on the optogenetics silicon probe. The channel outlet was aligned right next to the electrode showing the capability of highly co-localized electrochemical sensing, optical stimulation and chemical deliveries.
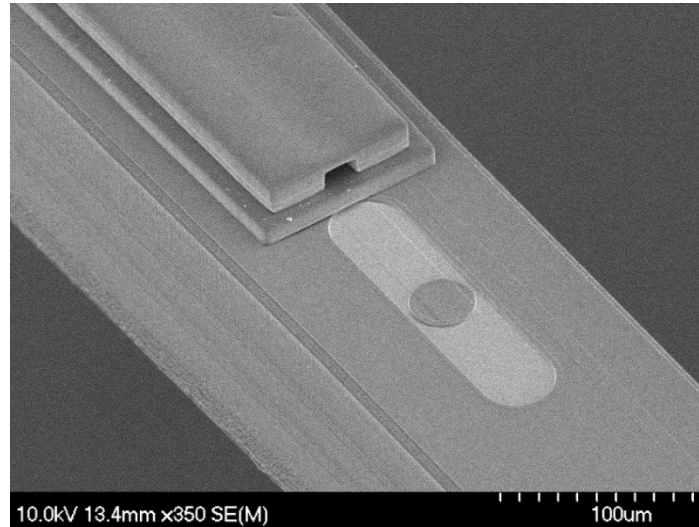
Figure 3.4 SEM of PDMS microfluidic channel transferred to the optogenetics probe

Figure 3.5 shows the transferred microfluidic channel on the backside of a conventional silicon probe with the liquid outlet facing perpendicular to probe surface instead of pointing to the probe tip, which would prevent channel clogging issue during the implantation process.
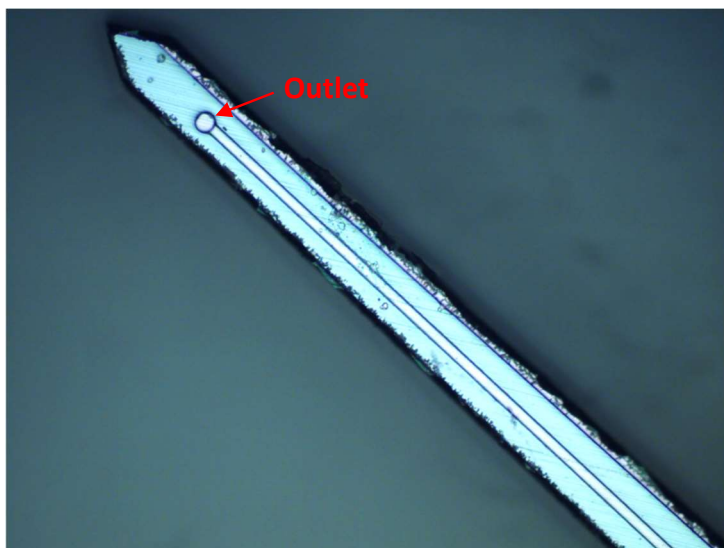
Figure 3.5 Microscope image of a microfluidic channel integrated on the backside of a silicon probe

3.4 *In vitro* characterization

The injection behavior of the microfluidic channel on the backside of silicon probes was tested in a brain phantom (0.6% agarose gel). ULTS probe was connected to a microfluidic tubing with preloaded liquid, which was connected to a constant pressure source. The probe was then implanted into a brain phantom to simulate the brain environment. Liquid started flowing out as soon as we turned on the pressure source, and the time duration for injecting all the liquid preloaded in the tubing was recorded. The flow rate was determined by the ratio between the preloaded volume and pumping duration. Flow rates at different pumping pressure (5-20 Psi) were tested for 3 times to determine the system repeatability.

The chemical delivery function was evaluated by injecting aqueous solution of red colored dye into brain phantoms with a pressure source (**Figure 3.6a**). The flow rate of the PDMS microfluidic channel was measured at various pumping pressures ranging from 5 Psi to 20 Psi (**Figure 3.6b**), which demonstrates a linear relationship ($R^2 = 0.996$) versus

the pumping pressure and high repeatability (n = 3). As suggested by Neeves *et al.*[52], backflow of infused solutions up the along the needle shaft would happen at flowrate higher than 1 μL/min, when the tissue was separated from the probe surface due to the large flowrate. It is also suggested that the backflow is correlated with the damage caused by the implant in terms of the size, insertion procedure. For a 30-ga needle, backflow was observed at a flowrate of 0.41 μL/min, while it was not observed until pumping at a much higher flowrate of 4.5 μL/min for a miniaturized neural probe with dimension of 100×100 μm (width × thickness). Poor insertion procedure would create larger wound in the brain and increase the possibility of backflow. Therefore, it is critical to have minimal increase of probe dimension with additional microfluidic channel; find out the range of flowrate without backflow and minimize the brain damage during the probe implantation process.
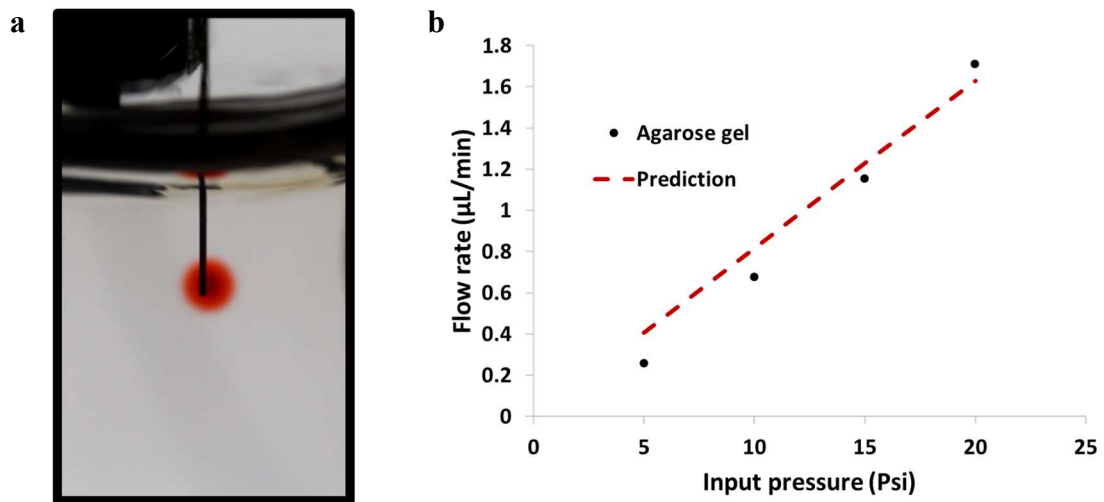
Figure 3.6 Fluidic injection in gel. (**a**) Optical image that demonstrates delivery of liquid (aqueous solution with red dye) into a brain phantom (0.6% agarose gel in water). (**b**) Flow rate of the microfluidic channel at different pumping pressures shows a linear relationship versus pumping pressure ($R^2 = 0.996$) and high repeatability (n = 3).

3.4 *In vitro* test

Next, we tested the integrated functions of electrochemical sensing and chemical delivery in an artificial cerebrospinal (aCSF)-brain phantom (0.6% w/v agarose in aCSF), by injection and detection of the same chemicals, glucose (800 μM). Local injections of the chemicals were immediately captured by biosensors (**Figure 3.7**). The current level starts decreasing when the injection ends based on pure diffusion. Fluid was injected at 20 Psi with 2 pumping duration, 2s and 0.2s, and repeated for three times. Under the same injection condition, the detected signal had almost identical pattern demonstrating the repeatability of the fluidic channel.
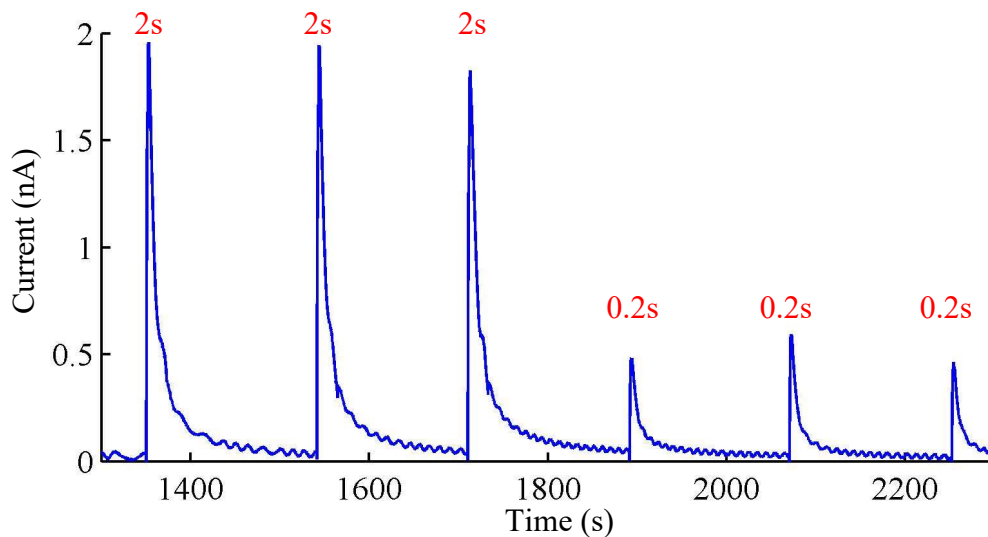
Figure 3.7 *In vitro* testing of 800μM glucose injection and detection in 0.6% agarose gel. The slow decrease in the glucose concentration is based on pure diffusion. Pumping pressure, 20Psi.

3.5 *In vivo* test

We also validated the chemtrode with glucose sensors in rat striatum. The integrated probe eliminates the need of inserting separate reference electrode and needle, hence reduces the brain damage and improve the alignment precision of the sensors and fluidic outlet. For *in vivo* tests, 4 mM glucose in aCSF solution was injected at 20 Psi with various injection duration. We converted the current signal to glucose concentration based on a calibration curve tested before the *in vivo* experiment. In this experiment, glucose injection was captured by biosensors immediately, followed by a sharp decrease which was likely due to the glucose uptake (**Figure 3.8**). Increasing the glucose injection duration not only increased the rising time, which is the same as the injection duration, but also increased the peak concentration, meaning more glucose reached the sensing sites.
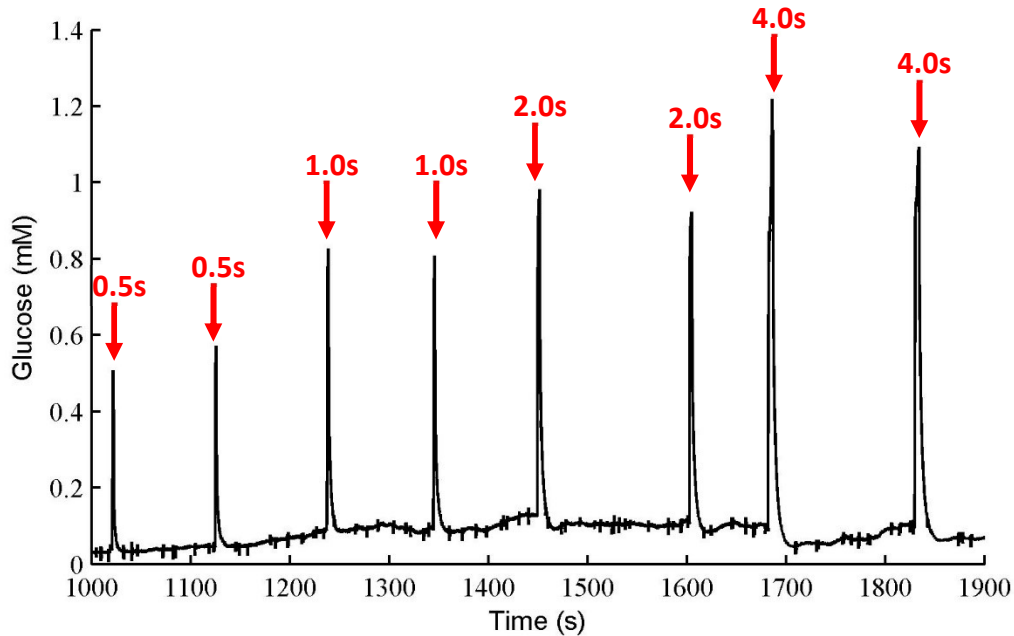
Figure 3.8 *In vivo* glucose (4mM) injection and sensing. Injection pressure was kept at 20 Psi with various injection duration. The detected glucose concentration peak increases as the pumping duration increases, meaning more glucose reach the sensing sites. Current response was converted to concentration based on pre-calibration curve.

We repeated the same experiment, which showed similar trend. By increasing the pumping duration, the signal level increased first (0.2-0.8s), and reached plateau at duration longer than 1.2s. At the same time, we also noticed some variations of glucose signal in terms of both signal pattern and amplitude (**Figure 3.9**). First, the baseline glucose level was very low in the first experiment, while it was much higher in the second experiment, which may come from the variation in different animals, and surgery procedures. Second, there was a reduction of glucose level below the baseline level following the injection, which may be due to the over-absorption of glucose from surrounding neurons.
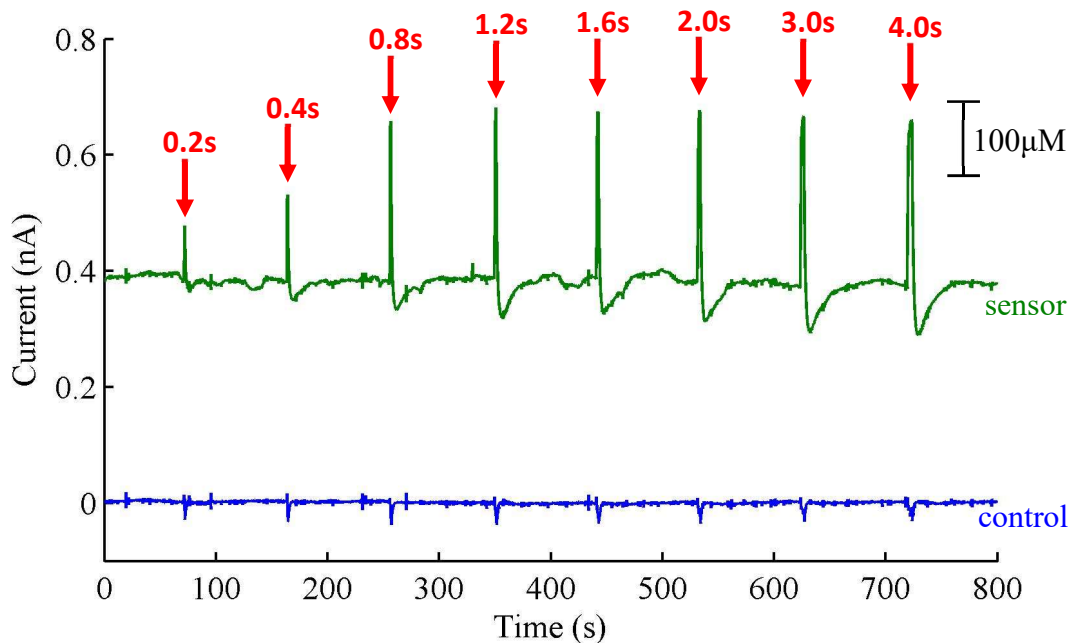
Figure 3.9 Second *in vivo* experiment with 4mM glucose injection and sensing. Green and blue curves represent signals from glucose sensor and a control electrode. Pumping pressure, 20 Psi

3.6 Discussion

Chemical delivery is one of the most important tools in neuroscience with numerous applications such as stimulation and inhibition of neuron activities, modify neurons by delivery of virus for optogenetics and chemogenetics, treat diseases like tumor by delivery pharmaceutical drugs. The combination of chemical delivery with other modalities such as optogenetics and electrochemical sensing will dramatically increase the diversity and possibility of conducting different neural science studies, and answer questions that cannot be answered using individual function alone. However, the integration of multiple functions into a miniaturized neural probe is usually complicated, and requires completely different fabrication process.

In this work, we presented a novel approach to integrate microfluidic channels on off-the-shell neural probes using a novel PDMS thin-film transfer process. Microfluidic channels have been transferred to two types of neural probes: (1) the optogenetics neural probe describe in chapter 2 and (2) existing neural probe developed by Monbouquette lab, while the latter case was validated in rat striatum with glucose injection and sensing. The key innovations of this work are the simple and versatile fabrication approach that is capable of wafer-level process as well as on-demand integration onto individual probes. The neural probes with microfluidic channel on backside instead of frontside were tested *in vitro* and *in vivo* because of the simpler fabrication process as mentioned above. However, it can be solved by simply enlarge the area of the probe base to accommodate fluidic adapters without changing any process to achieve the close distance between liquid outlets and electrodes with transfer of only 1 layer of PDMS thin-film.

We have noticed some variations of the detected signal with glucose injection in gel and *in vivo*. With dye injection experiment in gel, we observed the variation of the dye pattern at the probe tip and backflow at higher flowrate, which is highly related to the insertion procedure and the wound created by the probe. To minimize the tissue damage and backflow, the probe needs to be aligned in parallel with the insertion direction and the flowrate needs to be optimized.

The current experiment of injection and detection of the same chemical can be used as an easy approach to validate the *in vivo* performance of novel biosensors. In neuroscience studies, other chemicals can be injected to manipulate neuron behaviors. For example, potassium can be injected to depolarize neurons and trigger neural transmitter release, which consumes glucose, the source of energy. Other chemicals are also proposed

43

to be injected to silence the optogenetics response of the modified neurons to quantify the light artifact level. In these experiments, the transient flow pattern is less important, since it could take several minutes for the chemical/drugs to diffuse and get into a larger volume of cells to show the effects.

Although microfluidic channel with only one channel is demonstrated for chemical delivery, it can be easily scaled up with more liquid channels for chemical delivery at different location without increasing the dimension of the total thickness. Moreover, the microfluidic channel can also be converted to optical waveguide for optogenetics when filled with high refractive index material such as SU-8 and PDMS (GELEST OE-50).

Chapter 4

PDMS Neural Probes with Ultra-large Tunable Stiffness

4.1 Introduction

Implantable neural probes are important technologies for neuroscientists to detect and stimulate neuronal activities inside the brain. These tools are also employed to stimulate neural networks as a clinical treatment, known as deep brain stimulation (DBS), to various diseases such as Parkinson's disease, epilepsy, depression and obsessive compulsive disorder (OCD)[64], [85], [91]. When combined with *in vivo* neuropharmacology, microinjection of chemicals or virus, neural probes enable additional level of manipulation of neural activities, animal behaviors and treatment of neural diseases[10], [79]. Current approaches rely on implanting neural probes assembled with fluidic tubes for drug delivery, which causes huge damage to the targeted brain region due to their large footprint sizes. In the past few decades, with the development of microelectromechanical systems (MEMS), a great amount of efforts has been made to develop miniaturized multifunctional neural probes. Various silicon-based probes integrated with microfluidic channels have been developed [56], [92], [93]. However, the large mechanical mismatch between the rigid

probes (E~200 GPa) and the soft brain tissue (E~0.1-6 kPa) triggers long-term inflammatory responses that cause neuronal loss and scar formation around the implants. These rigid probes also result in extra brain damage due to brain motion[62]–[64], [94].

In recent years, efforts have been put on developing flexible probes based on polymers such as polyimide, parylene-C and SU-8 to reduce chronic immune response[72], [73], [95], [96]. However, due to their weak mechanical stiffness, there is a major challenge to directly implant soft probes into brain tissues. To mitigate this issue, soft probes are either coated with stiffening polymer that can be dissolved after implantation, or made of polymer whose stiffness can be tuned before and after implantation[62], [96]–[98]. However, deep brain penetration is challenging for such probes due to the low Young's modulus (~2 GPa) of polymers. Probes with large cross section area are needed to provide sufficient stiffness to prevent buckling during insertion[96], [97], [99]. Soft probes can also be attached with a stiff shuttle, such as a metal syringe and Si probes, that can be retracted after insertion[72], [73], [45]. The final location of the inserted probes, however, can be easily disturbed during shuttle retraction processes[100]. These approaches also require manual assembly processes, which makes them difficult to extend applications for fabricating multi-shank and 3D probe arrays. These insertion challenges together with other issues such as multifunction integration complexity and small footprint size requirement make the design and fabrication of flexible multifunctional probes for deep brain applications very difficult.

This work presents a multifunctional flexible and stretchable neural probe whose stiffness can be tuned by 5 orders of magnitude before and after brain insertion for chemical sensing and chemical delivery deep within the brain. This neural probe with Ultra-Large Tunable Stiffness (ULTS) can penetrate 2 cm deep into a gel with similar mechanical

properties as brain tissues. For in-vivo testing, this probe can penetrate 5mm deep into the rat brain. Once implanted, the probe becomes soft and flexible within a few minutes. With miniaturized design (30 µm thickness) and soft substrate material (1 MPa), this flexible and stretchable probe can greatly minimize brain damage due to brain movements in all directions[68], [101]. Deposition of appropriate enzymes and exclusion polymers onto the platinum electrode sites on ULTS permits electrochemical detection of neurotransmitters from deep-lying brain structures, and the integration of a microfluidic channel allows delivery of drugs and other chemicals in the local vicinity of the sensing sites. This is the first demonstration of a self-implantable, flexible multifunctional probe that integrates chemical sensing and chemical delivery capability into a compact footprint size for deep brain applications.

4.2 Design

The objective of making ultrasoft neural probes with large tunable stiffness and comparable sensing performance as silicon probes, we started our design from two fundamental elements: (1) to use PDMS as the substrate material due to its low Young's modulus of around 1 MPa, high stretchability of ~600% and biocompatibility[24], [85], [102]; and (2) to integrate platinum as sensing electrodes which are required for high performance electrochemical sensing and can be directly compared with prior works demonstrated on rigid silicon probes[7], [21].

Inspired by previous works done by John Roger's group [103], [104], thin oxide film is flexible and making metal patterning easy and straightforward. Therefore, in the first design (**Figure 4.1**), we fabricated Pt wires and electrodes on top of a 1 µm-thin SiO_2,

which was then covered by thicker PDMS film to provide temporary stiffening. However, after probe released in XeF_2, oxide cracks are observed. The difference between our structure and other works are the substrate material, PDMS vs. Polyimide. Polyimide is a relatively soft material compared to Si, however it is only bendable, while PDMS is much softer and highly stretchable. Continuous thin oxide film is prone to be stretched together with the PDMS substrate to reach its fracture point (~2%)[105] and break into pieces. On the other hand, we also noticed that the small oxide pieces are hard to be broken further under stretching since most of the strain is experienced by the PDMS under the cracks.
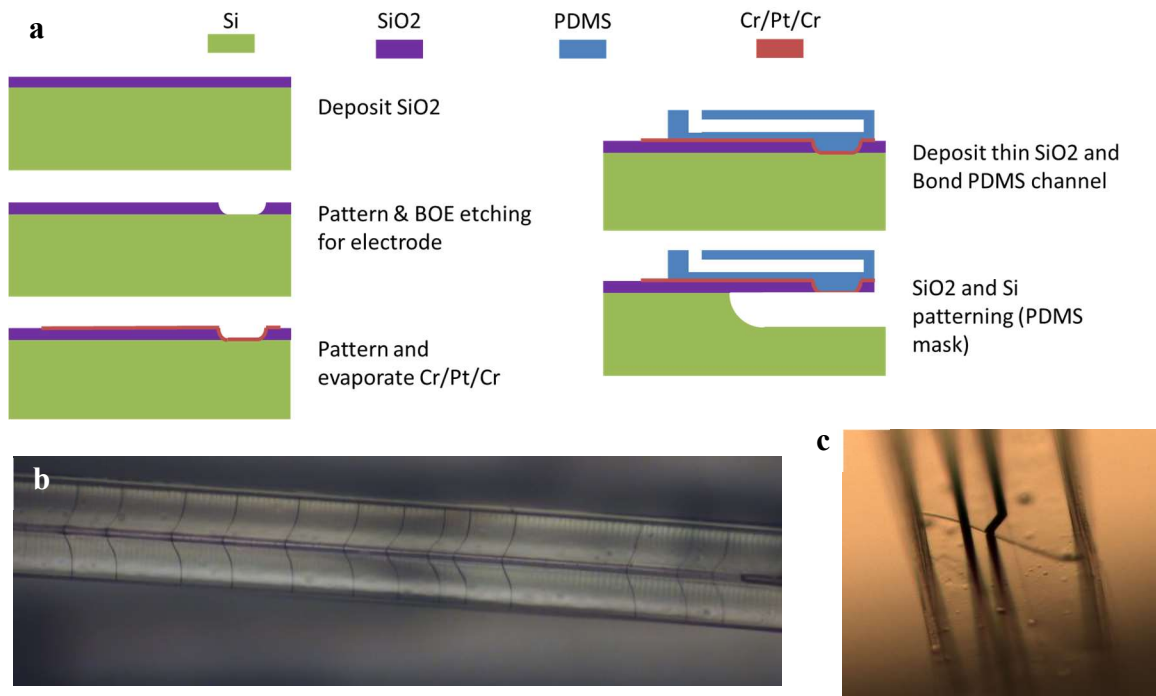
Figure 4.1 Initial design of the PDMS-based probe. (a) Process flow. (b), (c) Oxide cracks after probe release.

The finding gave us two inspirations: (1) isolate rigid and fragile components, such as oxide and metal, and leave most of the space with PDMS only; and (2) electrical interconnects need to be formed by intrinsically stretchable material to avoid cracking issues. Metal wires, such as gold and platinum are ductile to some extent, however starts

to crack with ~10% stretching[106], which is significantly smaller than the stretchability of PDMS despite the concern of poor adhesion between metal films and PDMS[102]. Devices with larger stretchability have been demonstrated by forming in-plane or out-of-plane serpentine metal lines[107], [108], however inevitably increased the device dimension, which is undesired for implantable neural probes. Gallium (Ga), a liquid metal, is used to provide electrical connections to these electrodes on the flexible and stretchable probe without cracking and delamination issues. In principle, liquid metal can be stretched infinitely following the deformation of the substrate such as PDMS[109]. Ga is highly conductive with a resistivity of ~ 140 nΩ·m, close to that of platinum (106 nΩ·m), which is 6 orders of magnitude higher than that of conductive polymers. At the same time, it can be filled into microfluidic channels, which can be easily fabricated using the customized PDMS thin-film transfer process as described before. Another reason of choosing Ga is its near body temperature melting point (~30 ºC) and relatively high Young's modulus at solid state (10 GPa), making it a promising material to temporarily stiffen the probe for brain penetration.

With above mentioned considerations, the finalized design has a four-layer free standing structure that integrates Pt electrode, microfluidic channels and soft PDMS substrate (**Figure 4.2**). The purpose of each layer is described as follows: **1. electrodes formation:** platinum electrodes are fabricated on thin and small silicon dioxide islands on a silicon substrate and transferred onto the probe for electrochemical sensing, which has the same exposed area (5656 μm^2) as the silicon probes[7], [21]. **2. PDMS layer 1:** ~5 μm-thick PDMS thin-film physically connects the electrodes on the probe tip with the probe base with vias for electrical contacts and liquid outlet (radius = 15 μm), as well as bottom

passivation of electrical interconnects and drug delivery channel. **3. PDMS layer 2:** PDMS thin-film with microfluidic channels for Ga interconnects and chemical delivery as well as top passivation. This layer has three microchannels with cross-section of 15 × 5 μm (w × t) and separated by 15 μm. The total thickness is ~10 μm. **4. PDMS layer 3:** PDMS stiffening channel filled with Ga and frozen into solid state to provide strength for brain penetration. This layer is 15 μm thick with a 104 × 10 μm (w × t) microchannel. The probe is designed to be a 9 mm-long, 144 μm-wide and 30 μm-thick straight (non-taper) single shank structure.
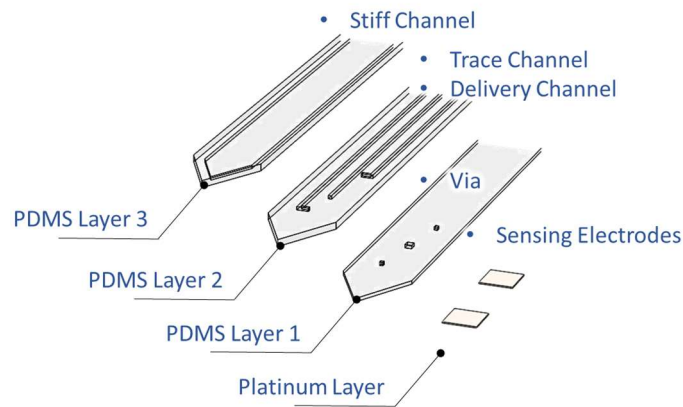
Figure 4.2 Schematics of the probe design. (a) Exploded view of the probe shows the four-layer structure of platinum electrodes and three layers of PDMS thin-films. (b) Final device with filled Ga

Utilizing the elastic property of PDMS, Ga in the stiffening channel can be filled with high pressure to increase the cross-section area by expanding the PDMS channel (**Figure 4.2**), which would further increase the probe stiffness. Therefore, there are two changing factors contribute to the ultra-large tunable stiffness: (1) phase change of Ga from solid state (E = 10 GPa) to liquid state (E = 0), and (2) shape change of the stiffening channel, where the bending stiffness is increased by the cube of the probe thickness.

50

Therefore, we named our devices as neural probe with Ultra-Large Tunable Stiffness, ULTS.
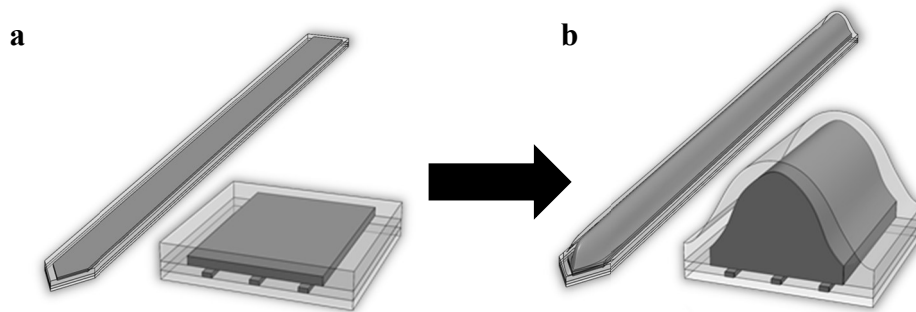
Figure 4.3 Schematic diagram showing the stiffening channel inflation. (a) Flat channel without pressure. (b) Inflated channel with pressurized Ga

Therefore, to fully utilize the tunable stiffness range, the implantation concept involves the following key steps (**Figure 4.4**): (1) selective brain cooling with cold saline of targeted depth down to below 30 ℃, (2) implantation of ULTS probes in "stiff" and "expansion" state following typical implantation procedures, (3) brain temperature recovery after stop applying cold saline and ULTS probes turn into "soft" and "flat" state to further reduce the bending stiffness.
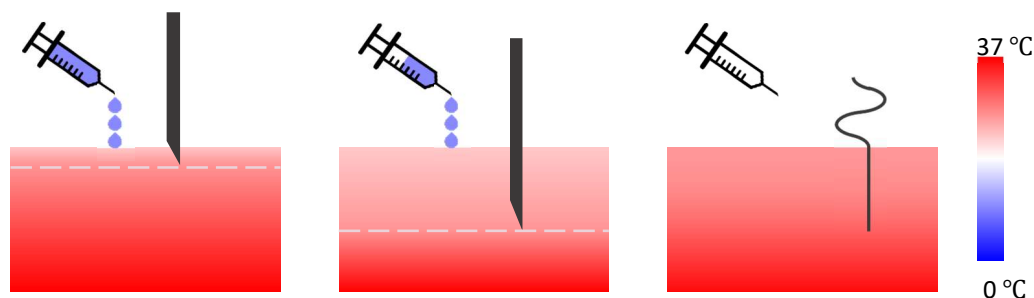
Figure 4.4 Schematics of the implantation procedure. Tissue is cooled down from the surface by application of cold saline. White dashed line represents the temperature of the Ga melting point, 30 ºC, above which the probe remains stiff.

4.3 Fabrication Process

The multifunctional ULTS probes were fabricated on Si wafers using conventional MEMS fabrication process for electrodes patterning and a customized PDMS thin-film transfer process to form the probe substrate and microchannels. Detailed steps involved in the fabrication of ULTS probes are illustrated in **Figure 4.5**, and the PDMS thin-film transfer process are illustrated in **Figure 4.6,** described in Chapter 3. The multifunctional single-shank ULTS probe has 1 drug delivery port and 2 electrochemical sensing sites. Key parameters of the probe are as follows: probe width, 144 μm; probe length, 9 mm; exposed electrodes area, 5656 μm^2; thickness of three PDMS layers, 5 μm, 10 μm and 15 μm respectively; microchannel dimension of electrical interconnects and drug delivery, 15 × 5 μm (width × height) and channel dimension of Ga stiffening, 104 μm × 10 μm (width × height). Key fabrication processes are summarized below: (i) Pt electrodes, soldering pads and SiO$_2$ insulators were patterned on a silicon substrate, which serves as a sacrificial layer (**Figure 4.5 a-e**). (ii) Photoresist (AZ 4620, ~5 μm) was patterned on the processed
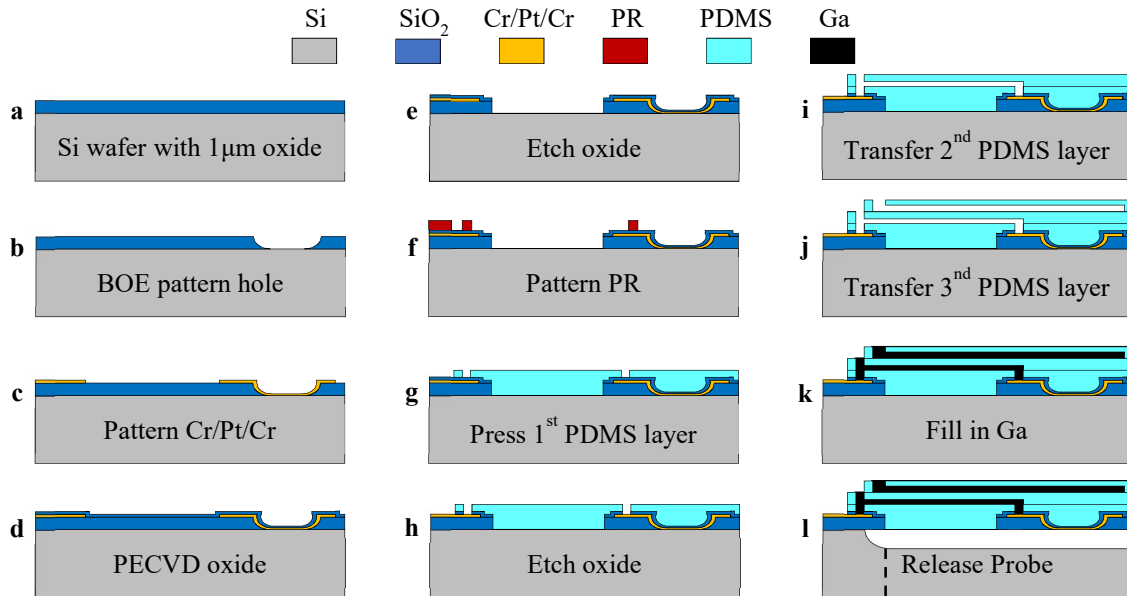
Figure 4.5 Fabrication process of ULTS probes with cross-section along the long axis of the probe: (a)-(e) Pt electrodes and oxide patternnig on Si wafer. (f)-(h) Pattern first layer PDMS using "lift-off" process to creat vias. (i)-(j) Transfer of PDMS thin-films. (k) Fill in Ga. (l) Prob release in XeF_2.

wafer to define the vias and probe shapes. PDMS was then applied and pressed to a thin-film by a silane treated glass. Photoresists were removed in acetone with sonication to expose the vias. Oxide in the vias was then etched by RIE, with PDMS as the etching mask (**Figure 4.5 f-h**). (iii) A second PDMS thin-film with microfluidic channels and top passivation was transferred and bonded to the first PDMS layer via O_2 plasma (80 W, 500 mT, 30s) (**Figure 4.5 i**). (iv) A third PDMS stiffening channel was transferred and bonded via O_2 plasma (**Figure 4.5 j**). (v) Liquid Ga was injected into interconnects and stiffening channels and frozen to solid state to maintain the shape and strength after XeF_2 releasing process (**Figure 4.5 k**). (vi) The probes were released by the Si undercut using XeF_2 in a pulse mode in which the etching chamber is repeatedly filled with XeF_2 gas to 1500 mT and kept for 60 s, and then pumped out to 50 mT (**Figure 4.5 l**). It should be noted that XeF_2 etching of Si is an exothermic reaction. The etching rate needs to be controlled to

prevent excessive heat accumulation that could melt the solid Ga. The 2 cm-long single-shank probes and 1 cm-long 4-shank probes are designed to demonstrate the mechanical properties of ULTS probes, which only have 2 layers of PDMS, (1) bottom passivation (10 μm thick), and (2) stiffening channel (20 μm thick), without sensing electrodes, electrical interconnects and drug delivery channel. The spacing between shanks is 500 μm, which can be easily reduced.
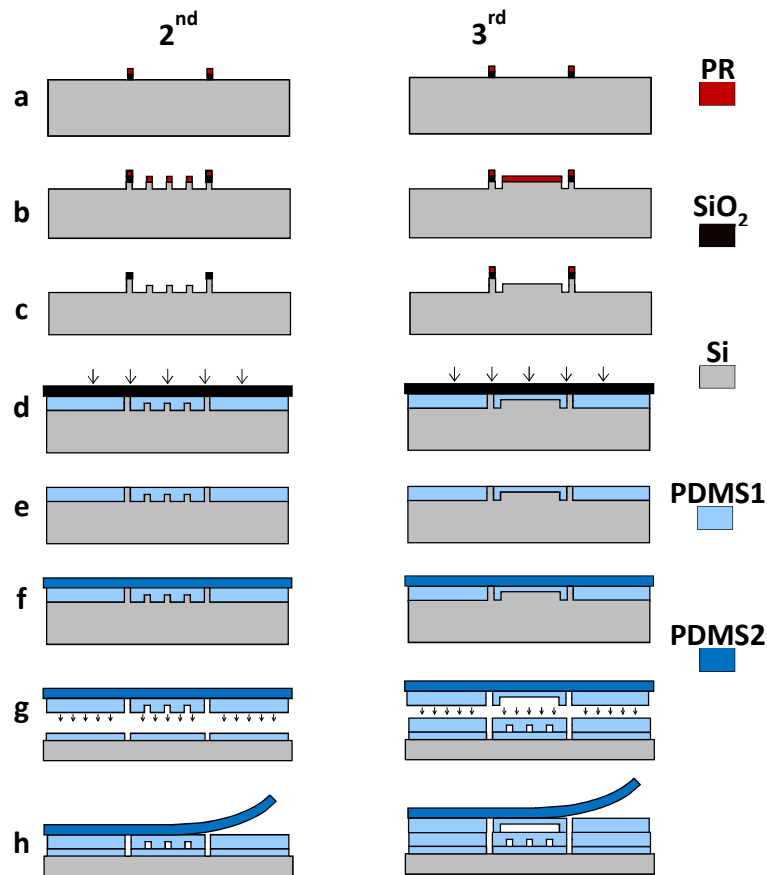
Figure 4.6 PDMS thin-film transfer process. (a)-(c) Si mold fabrication. (d) Press PDMS thin-film by a silane treated glass slide. (e) Remove glass and leave thin-film in mold. (f) Apply another layer of PDMS to (g) pick up the thin-film and for tranfer-bonding. (h) Remove the second PDMS layer leaving the thin-fim bonded to the substrate.

After release, the probes remain straight and stiff (**Figure 4.7 a**) and ready for brain implantation. Melting the Ga at elevated temperature (> 30 ºC), the probe becomes soft and

flexible (**Figure 4.7 b**). In the same way, four-shank probes are fabricated and stacked to form 3D probe arrays (**Figure 4.7 c**).
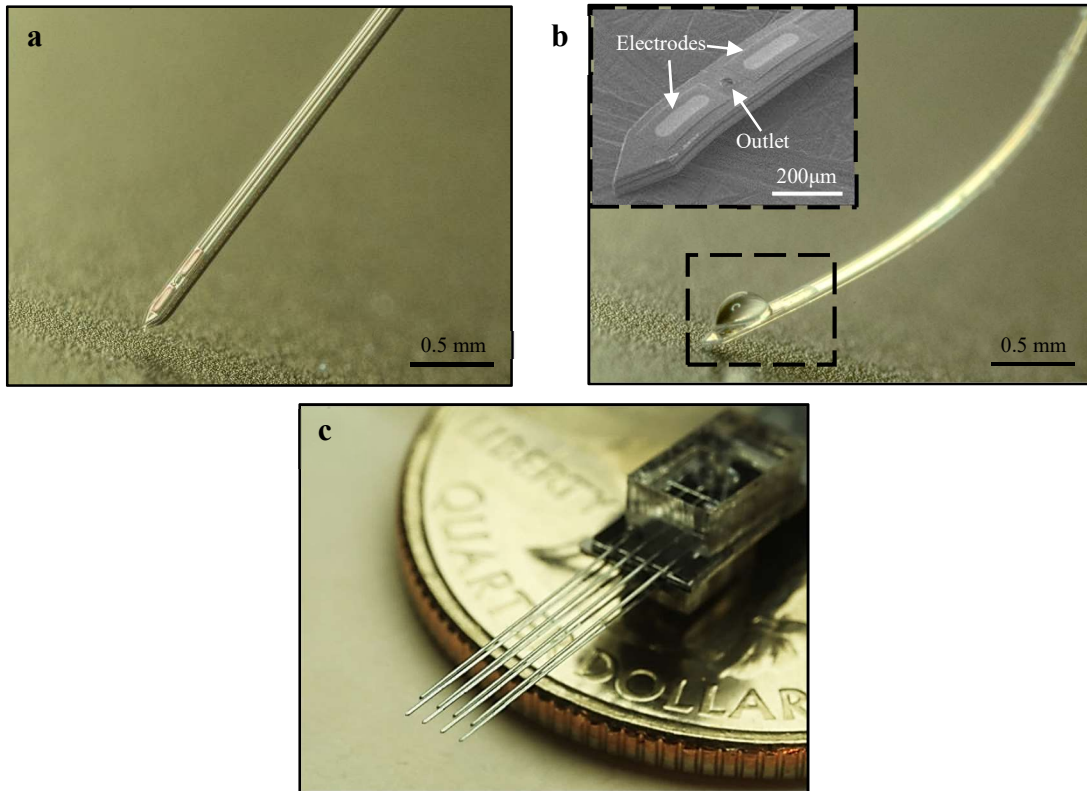
Figure 4.7 Images of released probes: (**a**) Picture of an ULTS probe in the stiff state for brain implantation. (**b**) An ULTS probe in the soft state with integrated chemical delivery function. Inset, SEM of the probe tip that shows the outlet of the chemical delivery channel and electrodes. (c) Two 4-shank probes were assembled to a 3D probe arrays that can be potentially used to record and stimulate neurons in a large volume.

4.3 Characterization of Probe Tunable Stiffness

To investigate the tunable stiffness range, we first characterized the probe deformation with respect to different Ga filling pressures (**Fig. 4.8**). The maximum pressure injected was 60 Psi, which resulted in the largest deformation of ~67 μm. The channel was expanded close to a semicircle with radius of 52 μm at pumping pressure of 30 Psi.
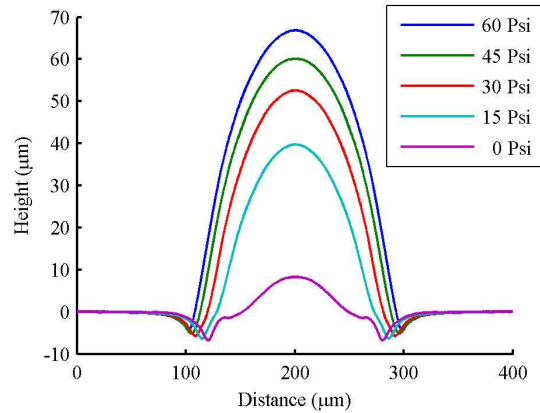
Figure 4.8 Characterization of the probe deformation with respect to different Ga injection pressure

The range of tunable bending stiffness was calculated based on the materials' Young's modulus and the shapes of the probe between the "stiff" and "inflation" state and the "soft" and "deflation" state. For a conservative estimation, the expanded shape was approximated to be a semi-circle (profile at 30 Psi) with a radius of 52 μm. This resulted in a stiffness difference of 5 orders of magnitude between these two states, where the phase change contributes ~4 orders of magnitude and shape change contributes to the rest 10-fold. During real applications, an even larger tunable range can be obtained when a higher pressure (60 Psi) is applied to provide a probe with larger cross-section before insertion.
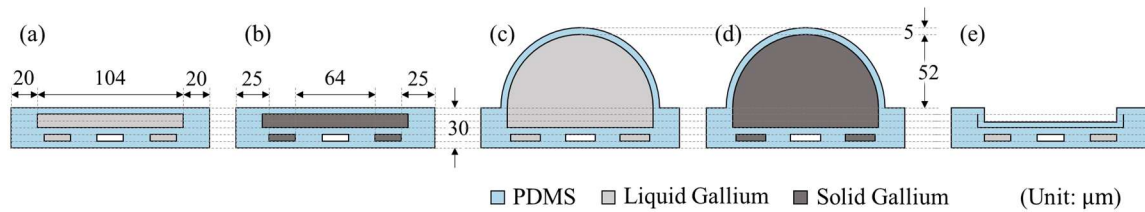
Figure 4.9 Model of neural probes: (a) "Soft" and "flat" state, (b) "Stiff" and "flat" state, (c) "Soft" and "inflation" state, (d) "Stiff" and "inflation" state, (e) "Soft" and "deflation" state

The bending stiffness per width D depend on its cross-section shape and the material properties, as

$$D = \sum_i \frac{E_i I_i}{w} \tag{1}$$
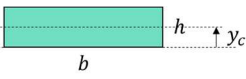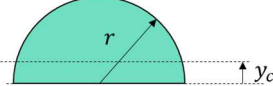
where w is the probe width $(144\,\mu m)$, E is the Young's modulus of material ($E_{\text{Liquid–Gallium}}$ is ~ 0 Pa, $E_{\text{Forzen–Gallium}}$ is ~ 10 GPa, E_{PDMS} is ~ 1 MPa), and I is the second moment of area with respect to the neutral axis. It is easier to derive the second moment of area with respect to its central axis, and use the parallel axis theorem to derive the second moment of area with respect to the neutral axis, as

$$I = \sum_j \left[I_{cj} + A_j \left(y_{cj} - \bar{y} \right)^2 \right] \tag{2}$$

where A is the area of the shape, I_c is the second moment of area with respect to its central axis, y_c is the location of its central axis, and $\bar{y}$ is the location of neutral axis. The expression to calculate A, I_c and y_c are summarized in the **Table 1**. The location of neutral axis $\bar{y}$ can be written as

$$\bar{y} = \frac{\sum_j E_j A_j y_{cj}}{\sum_j E_j A_j} \tag{3}$$
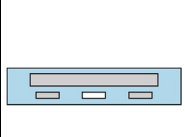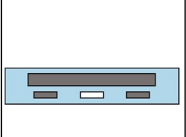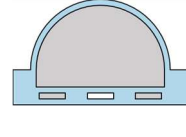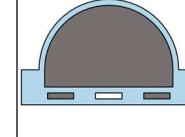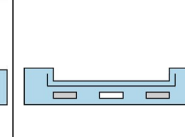
Table 1. The area, second moment of area and the central axis location of rectangle and semicircle

Rectangle	I_c	A	y_c	Semicircle	I_c	A	y_c
	$\dfrac{bh^3}{12}$	bh	$\dfrac{h}{2}$		$\dfrac{r^4(9\pi^2 - 64)}{72\pi}$	$\dfrac{\pi r^2}{2}$	$\dfrac{4r}{3\pi}$

The calculation results of five models are shown in **Table 2**, where the inflated shape with solid gallium has the highest bending stiffness per width $(1.41 \times 10^{-4}\ \text{N·m})$ for tissue penetration and the deflated shape with liquid gallium has the lowest bending stiffness per width $(1.32 \times 10^{-9}\ \text{N·m})$ to reduce micromotion-induced damage. Therefore,

57

the range of tunable stiffness can be as large as 10^5, where the gallium phase change contributes close to 4 orders of magnitude difference ("stiff" and "inflated" vs. "soft" and "inflated), while the shape change contributes to the rest 10-folds ("soft' and "inflation" vs. "soft" and "deflation").

Table 2. The location of neutral axis and the bending stiffness per width of models

$\bar{y}\ (\mu m)$	13.85	18.42	24.60	43.20	12.56
$D\ (\text{N} \cdot \text{m})$	1.89×10^{-9}	2.05×10^{-6}	1.56×10^{-8}	1.41×10^{-4}	1.32×10^{-9}

4.4 Temperature response of ULTS probes

To confirm the probe softening temperature at ~ 30 ºC, we inserted an ULTS probe into DI water with elevating temperature from room temperature (~ 25ºC) to above 30 ºC. DI water was contained in a beaker with stir bar sitting on top of a hotplate with. Probe was inserted into the stirred water at room temperature, and showed no deflection at its stiff state.
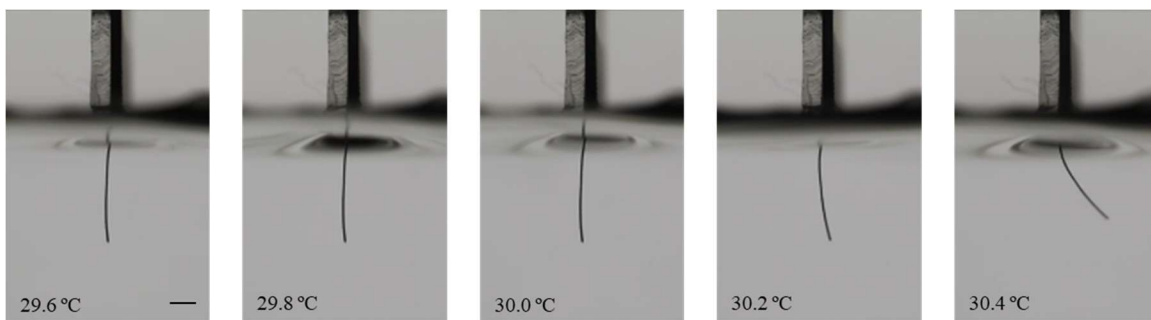
Figure 4.10 Probe softening in stirred and heated water. Below 30 ºC, probe remains stiff indicated by the unchanged probe shape. At higher temperature, probe becomes soft and the shape is disturbed by the stirring water. Scale bar, 1 mm.

4.5 Testing of Self-Implantation Capability in Gel

We tested the ULTS probes in brain phantoms (0.6% agarose gel), which has similar mechanical properties to neural tissues. 9 mm-long ULTS probes can be implanted into brain phantoms robustly when filled with Ga at 15 Psi phantom in "stiff" state at room temperature (**Figure 4.11a**), whereas a probe in "soft" state at elevated temperature (T > 30 ºC) could not remain straight and would deform upon contact with the brain phantom surface. A 2-cm long probe, filled with Ga at 60 Psi, can also be implanted into this brain phantom in "stiff" state at room temperature (**Figure 4.11b**) A four-shank ULTS probe was also fabricated and implanted into the brain phantom, demonstrating the capability of scaling up to multi-shank probe and 3D probe arrays for large volume neural recordings (**Figure 4.11c**).
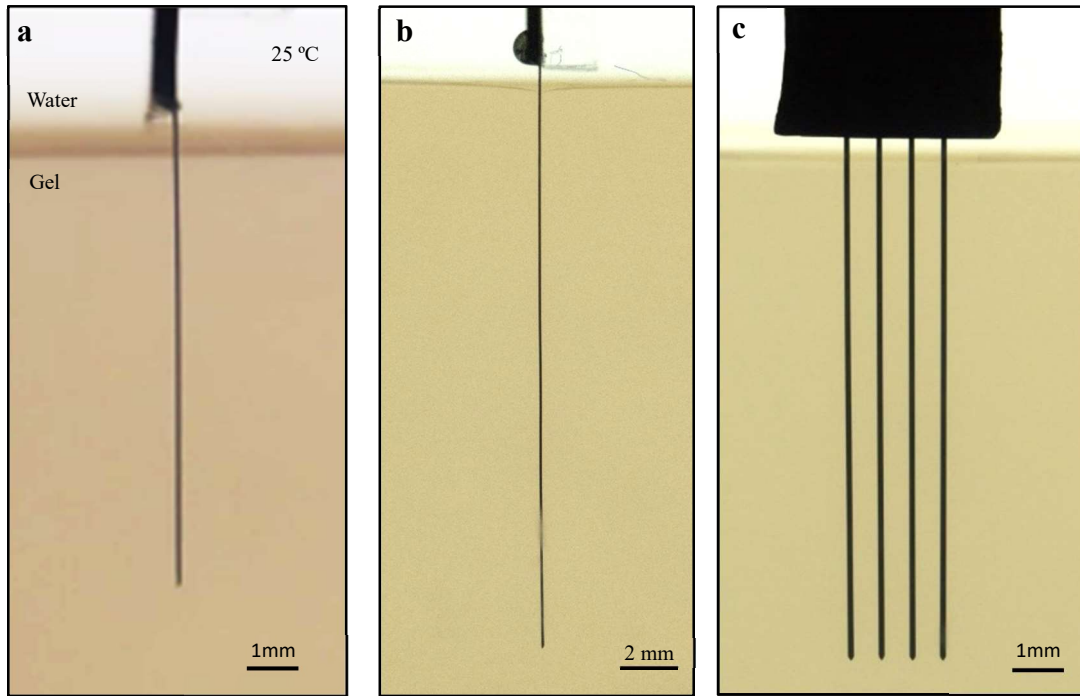
Figure 4.11 Implantation of (**a**) 9-mm long single-shank probe, (**b**) 2-cm long single-shank probe, (**c**) 1-cm long 4-shank probes in brain phantom (0.6% agarose gel) at room temperature.

After implantation, the brain phantom was heated up in a water bath to 37 ℃ to simulate brain temperature recovery. Ga was melted and the stiffening channel was deflated by active suction from the inlet of the Ga channel to reduce the bending stiffness in "soft" state (**Figure 4.12**).
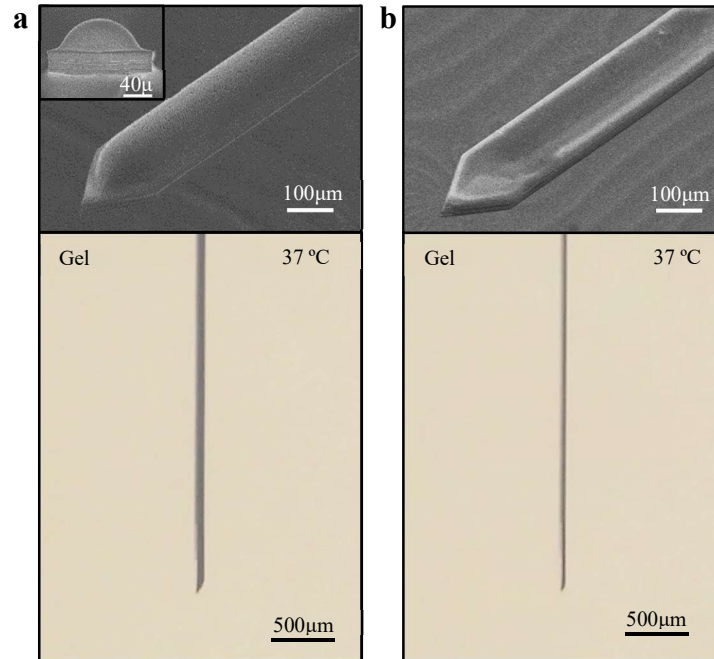
Figure 4.12 (a) ULTS probes in the "expansion" state. Top, SEM bird view of an ULTS probe tip with 15 Psi injection pressure. Scale bar, 100 μm Inset, SEM front view shows a deformation of 40 μm. Scale bar, 40 μm. Bottom, picture of a probe implanted in a brain phantom with expanded shape. Scale bar, 500 μm. **(b)** ULTS probes in the "deflation" state. Top, SEM bird view of a deflated ULTS probe tip. Scale bar, 100 μm. Bottom, picture of a "deflated" probe by active suction of Ga. Scale bar, 500 μm.

For comparison, we tested the flexibility of "soft" ULTS probe as well as Si and SU-8 based probes with similar dimensions (~150 μm wide and ~50 μm thick) (**Figure 4.13, 4.14**). ULTS probe was so flexible that the implanted portion of the probe kept steady regardless of the movement of gel in all directions, whereas both Si and SU-8 probes created larger wound during the movement of probe bases.
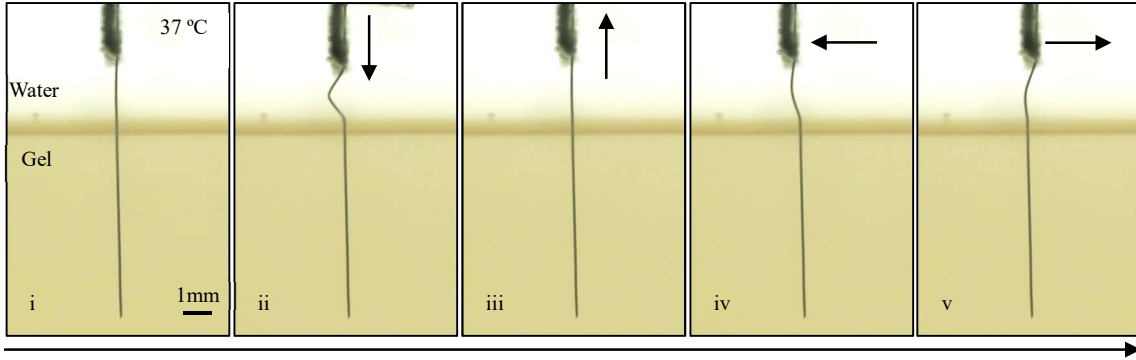
Figure 4.13 Pictures of a "soft" ULTS probe in a brain phantom. Probe base was moved in all directions to simulate the relative motion between skull and brain. Scale bar, 1 mm.
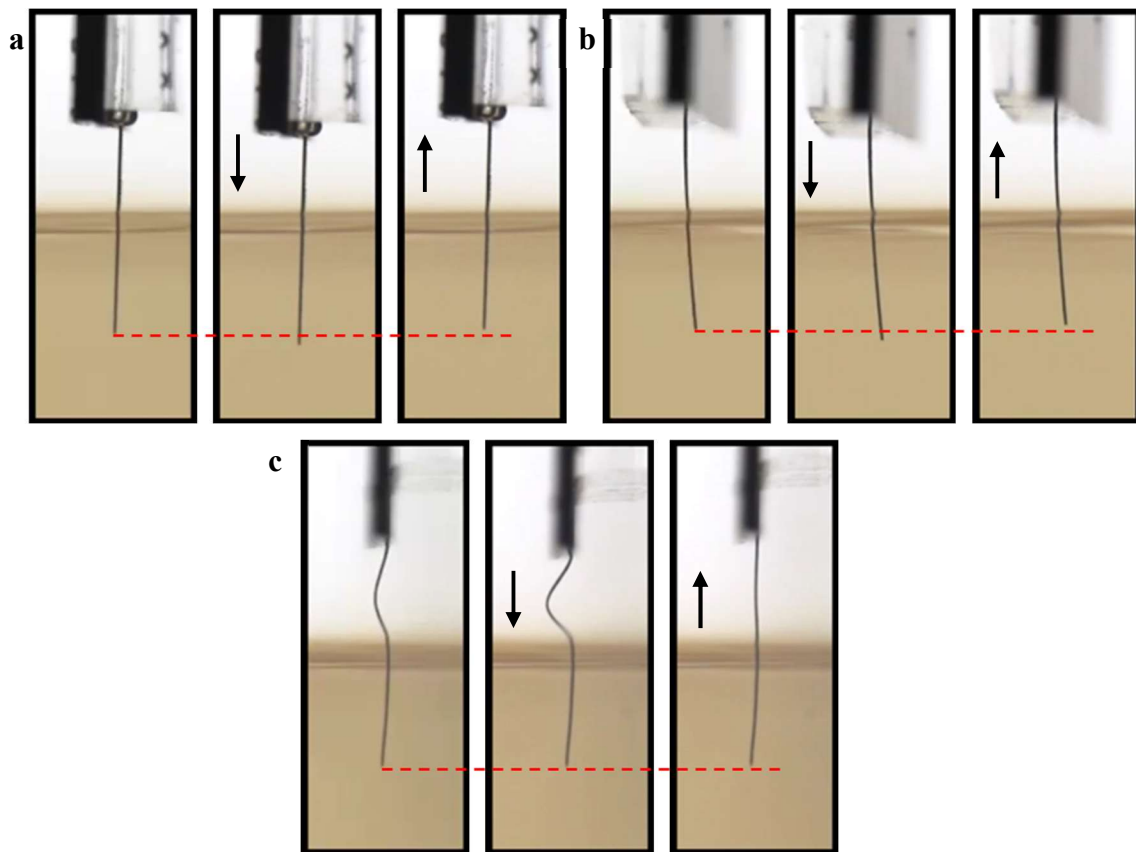
Figure 4.14 Comparison of Si, SU-8 and ULTS probes with similar dimension (50 μm thick) with vertical probe movement to simulate the relative brain/skull movement. Si (**a**) and SU-8 (**b**) probes followed the vertical movement, while ULTS probe (c) remained steady inside the gel without obvious movement. Arrows indicate the movement direction.
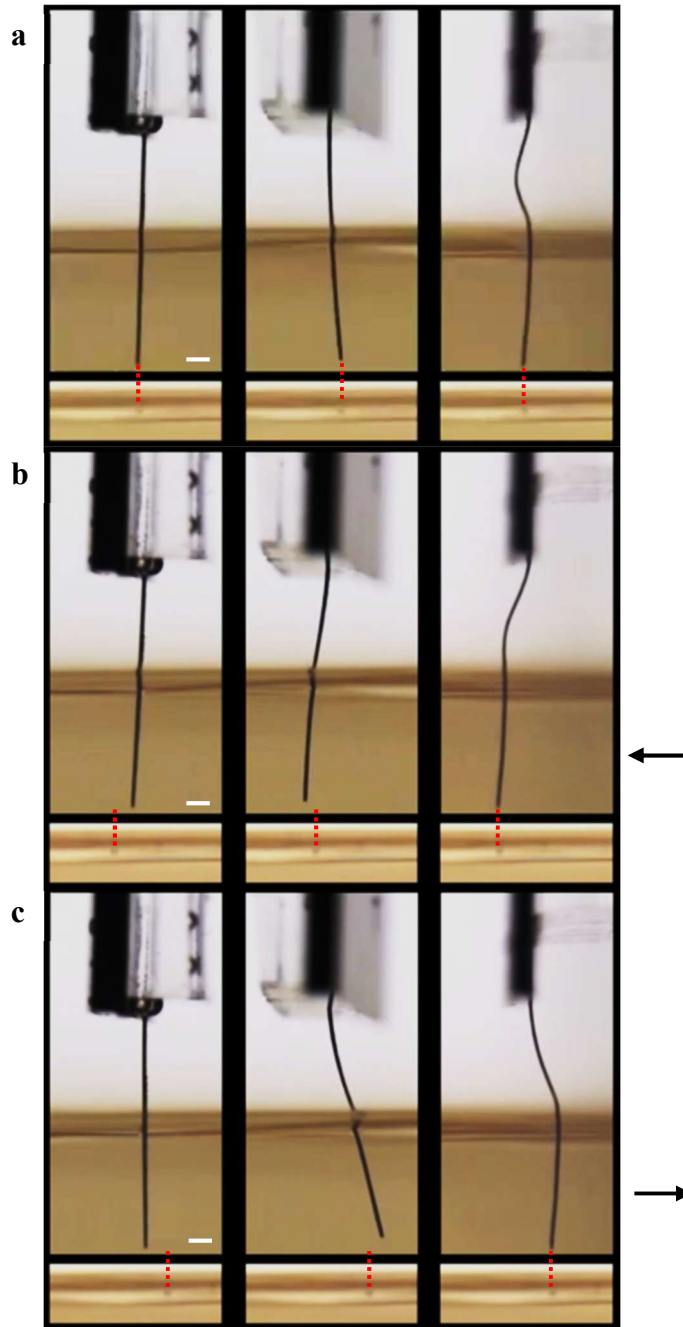
Figure 4.15 Comparison of Si, SU-8 and ULTS probes with similar dimension (50 μm thick) with 500 μm lateral gel movement to simulate the relative brain/skull movement. Silicon probe tended to keep its original position, and created a rectangular wound pattern with the tip scratches a line of ~1000 μm. SU-8 probe created a cone-shape wound pattern, with the probe anchored at the gel interface. The probe tip scratches a line of >1000 μm. While ULTS probe followed the gel movement perfectly without creating any visible wound in gel. Arrows indicate the gel movement direction.

4.6 Fabrication and Characterization of Biosensors on ULTS probes

Pt electrodes on ULTS probes were converted into enzymatic biosensors for chemical detections. Amperometric electroenzymatic methods for the near real-time detection of chemicals, such as neurotransmitters and glucose, have been developed using platinum electrodes modified with H_2O_2-generating oxidase [8], [22], [110], [111]. In the presence of H_2O_2-generating oxidase, the substrate of interests can be converted into H_2O_2, which can be directly electrooxidized by applying anodic potentials on platinum electrodes and converted to electrical current signals that can be recorded. Unfortunately, efficient oxidation of H_2O_2 requires a high anodic potential at which electroactive interferents, such as dopamine (DA) and ascorbic acid (AA), are also oxidized and thereby contribute an undesired amperometric current signal[112]. A layer of poly-m-Phenylenediamine (PPD) were electrodeposited in this study to block common interferents (e.g. AA and DA), to reduce signals from undesired oxidation reaction.

Bare Pt electrodes were first tested to characterize the response to H_2O_2. Before acid cleaning process, the sensitivity varies a lot among different electrodes and typically have a 0.1-1 nA response to 20 μM H_2O_2, leading to a poor repeatability of the final biosensor performance. It is believed that the unstable and low response of the bare Pt electrodes are due to the impurities of the deposited Pt and organics residues on top. Therefore, Pt electrodes are routinely cleaned in sulphuric acid (H_2SO_4) electrochemically by scanning the voltage between -0.2 V to 1.3V for 3 cycles vs. Ag/AgCl reference electrode and Pt counter electrode in a three-electrode system. After the cleaning process, all sensors exhibit a similar response of ~2 nA to 20 μM H_2O_2. **Figure 4.16** compares

typical bare Pt sensors with/without acid cleaning. All the sensors were cleaned before

coatings in this work.

Bare Pt sensor for H$_2$O$_2$ Sensing
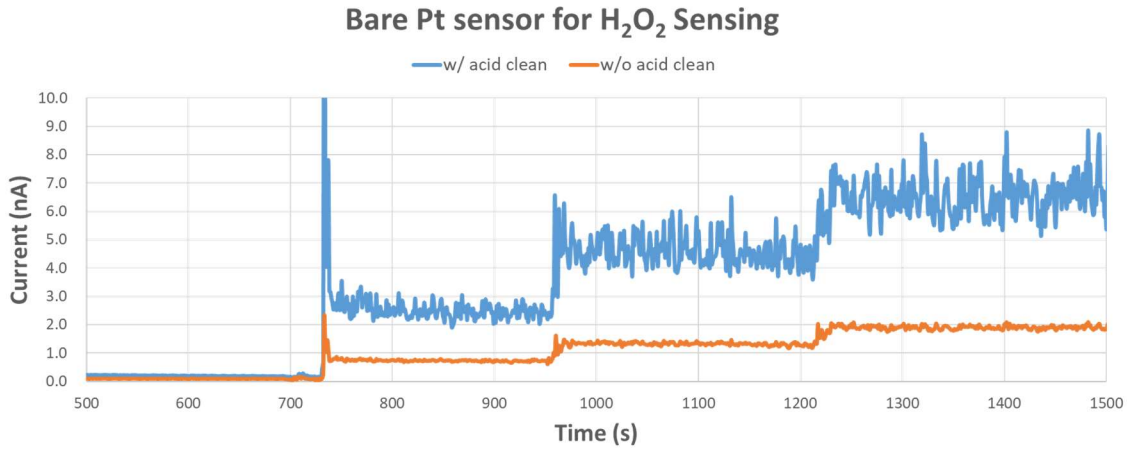
Figure 4.16 Bare Pt sensor test for H$_2$O$_2$ sensing before and after acid cleaning process

We coated the PPD modified Pt electrodes with GluOx to detect the amino acid

Glut, which is the major excitatory neurotransmitter in the mammalian central nervous

system and related to many abnormal behaviors apparent in neurological and psychiatric

disorders[13], [113], [114] (**Figure 4.17**).
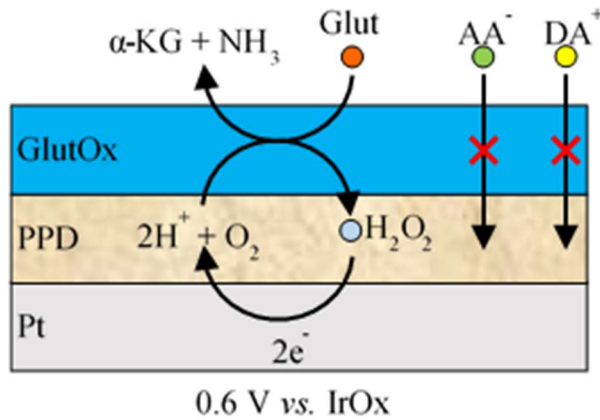
Figure 4.17 Schematic diagram of the coatings on a single electrode on the ULTS probe

The sensitivity, detection limit and linear range were tested by sequential injection of Glut solutions into a stirred PBS buffer. **Figure 4.18a** shows a representative current response of biosensor to Glut with concentrations of 20, 40, 60, 80, 100, 120, 140 and 160 μM. **Figure 4.18b** shows the calibration curve for Glut biosensors (n = 4), displaying a linear detection range of up to 160 μM (R^2 = 0.994)), which covers the concentrations in the physiological range[21]. The Glut sensors coated on ULTS demonstrate a comparable performance to silicon based biosensors with the same electrode design[21], [39]. High sensitivity of 8.2 ± 1.2 pA/μM and detection limit of 0.39 ± 0.07 μM (n = 4) at a signal-to-noise ratio of 3 was achieved. At the same time, common interferents in brain extracellular fluids, AA and DA, were successfully blocked by the PPD layer (**Figure 4.18c**), while the response of glutamate detection was ~1 s, demonstrating a near real-time sensing capability.

Using the same process, Pt electrodes were also converted into Glucose sensor to show the versatility of the platform. **Figure 4.18c** shows a representative sensing curve of glucose, showing a ~6.5 nA response to 800 μM glucose concentration, which is similar to silicon probes.
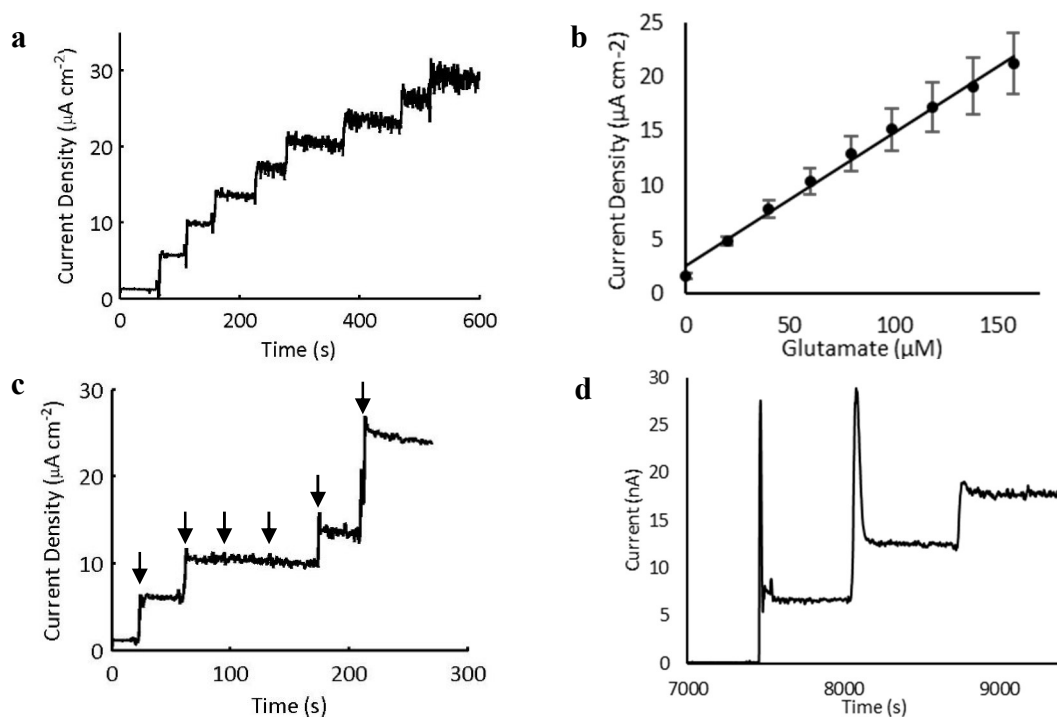
Figure 4.18 Characterization of Glut sensor. (a) A representative current response of the biosensor to Glut. (b) A calibration curve for glutamate biosensor (n = 4) that shows a linear detection behavior in the relevant physiological range, < 10-160 μM. Error bars mark the SD. (c) Current response of the glutamate biosensor to interferents, glutamate and H_2O_2. Arrows indicate the sequential injections of 20 μM Glut, 20 μM Glut, 5 μM DA, 250 μM AA, 20 μM Glut and 20 μM H_2O_2

Electrochemical preparation of the sensors, and characterization (sensitivity and detection limit) were performed using a Versatile Multichannel Potentiostat (model VMP3) equipped with the 'p' low current option and low current N' stat box (Bio- Logic USA, LLC, Knoxville, TN, USA). Gel and *in vivo* experiments were conducted with a multichannel FAST-16 potentiostat (Quanteon, LLC, Lexington, KY, USA). Amperometric data were collected at 80 kHz and averaged over 0.1 s intervals and further processed using moving average filter with 11 input points in MATLAB to remove noise at 1 Hz.

Microelectrodes on ULTS probes were rinsed with DI water followed by electrochemical cleaning step with 0.5 M sulfuric acid. Electropolymerization of poly-m-

Phenylenediamine (PPD) on electrode surface (5 mM m-Phenylenediamine in stirred PBS, 0.85 V *vs.* Ag/AgCl, 15 min) was conducted using a standard three-electrode system, consisting of a platinum wire auxiliary electrode, a glass encased Ag/AgCl in 3M NaCl solution reference electrode (Bioanalytical Systems, Inc., West Lafayette, IN, USA), and a platinum working electrode on our ULTS probes. After the PPD deposition, the GlutOx solution for enzyme immobilization was prepared by mixing 2 µL GlutOx (250 unit/mL) with 3 µL BSA solution (10 mg/mL) containing glutaraldehyde (0.125% v/v). A ~0.1 mL drop of the solution was formed on a syringe tip and the drop was gently swiped across the microelectrode sites at the probe tip. This procedure was repeated 11 times. The resulting Glut sensor microprobe was left to dry overnight in a desiccator at 4 °C.

In vitro (pre-calibration and post-calibration) and *in vivo* measurements were conducted using a two-electrode system, with a separate microscale IrOx reference electrode (0.6 V *vs.* IrOx). IrOx was electrodeposited onto silicon-based multielectrode arrays (MEAs) following the method described by Tolosa *et al*[21]. Before IrOx deposition, electrode surfaces were first modified with Pt nanoparticles to increase the surface area following the method described by Boehler *et al*[115]. The detailed fabrication process was described in previous work. Before making measurements, more than 30 min of equilibrium time in sodium phosphate buffer (PBS) or ~1 hr of equilibrium time for *in vivo* studies was required for the current detected to approach a constant baseline.

For *in vitro* studies, three 20 µL aliquots of glutamate (10 mM) were added to the beaker containing 10 mL PBS solution to reach a final glutamate concentration of 20, 40 and 60 µM glutamate. Additionally, aliquots of the potential interferents, AA (250 µM final concentration) and DA (5-10 µM final concentration), were added to the beaker in most

tests to determine selectivity for glutamate. A calibration factor based on analysis of these data was calculated for each electrode on the ULTS microprobes to be used for *in vivo* experiments.

4.7 Characterization of the microfluidic channel

As shown in **Figure 4.19,** the injection behavior of the microfluidic channel was tested in a brain phantom (0.6% agarose gel). ULTS probe was connected to a microfluidic tubing with preloaded liquid, which was connected to a constant pressure source. The probe was then implanted into a brain phantom to simulate the brain environment. Liquid started flowing out as soon as we turned on the pressure source, and the time duration for injecting all the liquid preloaded in the tubing was recorded. The flow rate was determined by the ratio between the preloaded volume and pumping duration. Flow rates at different pumping pressure (30-60 Psi) were tested for 3 times to determine the system repeatability.
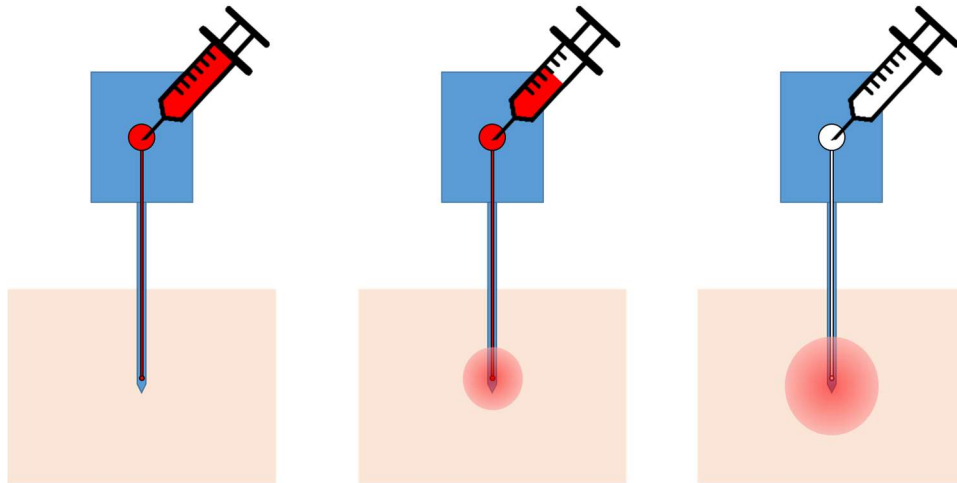
Figure 4.19 Schematic diagram of the liquid pumping system to characterize the chemical delivery function

The chemical delivery function was evaluated by injecting aqueous solution of red colored dye into brain phantoms with a pressure source (**Figure 4.20a**). The flow rate of

the PDMS microfluidic channel was measured at various pumping pressures ranging from 30 Psi to 60 Psi (**Figure 4.20b**), which demonstrates a linear relationship ($R^2 = 0.995$) versus the pumping pressure and high repeatability (n = 3). Therefore, the integrated microfluidic channels on ULTS probes are capable of reliable drug delivery. It should be noted that the flow rate of the microfluidic channel on ULTS probe is much slower than that described in chapter 3, which is due to the smaller channel dimension.
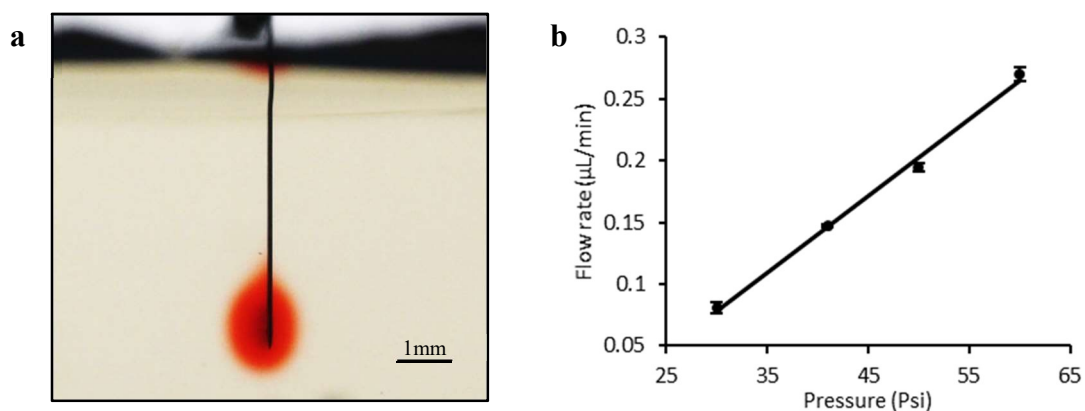
Figure 4.20 Fluidic injection in gel. (**a**) Optical image that demonstrates delivery of liquid (aqueous solution with red dye) into a brain phantom (0.6% agarose gel in water). Scale bar, 1 mm. (**b**) Flow rate of the microfluidic channel at different pumping pressures shows a linear relationship versus pumping pressure ($R^2 = 0.995$) and high repeatability (n = 3).

4.8 Electrochemical sensing and chemical delivery test in gel

Next, we tested the integrated functions of electrochemical sensing and chemical delivery in an artificial cerebrospinal (aCSF)-brain phantom (0.6% w/v agarose in aCSF), by injection and detection of the same chemicals, H_2O_2 (40 μM) and glutamate (150 μM). Local injections of the chemicals were immediately captured by biosensors. Increasing the injection volume resulted in higher detection peak, where the duration of rising edges was the same as the injection duration (**Figure 4.21**). The current level starts decreasing when

the injection ends based on pure diffusion. Due to the molecular weight difference between H_2O_2 (34 g/mol) and glutamate (147 g/mol), the signal level of H_2O_2 decays much faster than that of glutamate (~10s vs. ~50s). The results demonstrate the in-vitro functionality of the ULTS probe.
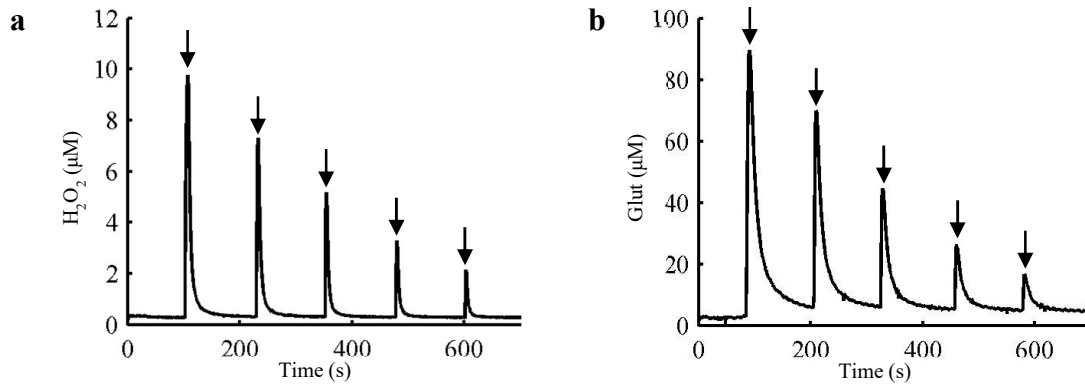
Figure 4.21 In vitro testing of chemical delivery and detection of 40 µM H_2O_2 (**a**) and 150 µM Glut (**b**) in aCSF brain phantom tissues (0.6% agarose gel in aCSF). Liquid was injected at 60 Psi with injection duration of 4.8 s, 2.4 s, 1.2 s, 0.6 s and 0.3 s (Arrows) with 2 mins interval.

4.9 In-vivo experiments

Next, we implanted ULTS probes in rat striatum (A/P +1.0 from bregma, M/L +2.5 and D/V -5.0) to test their *in vivo* capabilities. For tests *in vivo*, male Sprague Dawley rats (250–300 mg) were anesthetized with isoflurane and placed in a standard stereotaxic frame for surgery. All experimental procedures and surgeries were conducted in accordance with the Institutional Animal Care and Use Committee and UCLA.

In a typical implantation procedure (**Figure 4.22**), a microscale temperature probe (HYP1-30-1/2-T-G-60-SMP-M, Omega Engineering, Inc.) was first inserted under the skull (5.0 mm depth) at a site remote from the recording area. Cold sterilized saline (~10 °C) was used to moderately cooled down the brain tissue to below 30 °C to keep the probe

71

straight and stiff throughout the entire implantation track. Then, the ULTS probe with microbiosensors, pre-calibrated to glutamate (see above) was unilaterally implanted into the right stratum (A/P +1.0 from bregma, M/L +2.5 and D/V -5.0) according to the atlas of Paxinos and Watson (4th ed.), typically within a minute to reduce the brain cooling duration. In the meantime, the body temperature of rats was kept at 37 ºC by a heating pad underneath the body during surgeries. The cooling process typically lasts for 3-5 mins, and the temperature recovers to baseline in a few minutes (**Figure. 4.23**). We confirmed that the probe was implanted to the targeted region in striatum by a bright-field microscopy image of brain slices (**Figure. 4.24**).
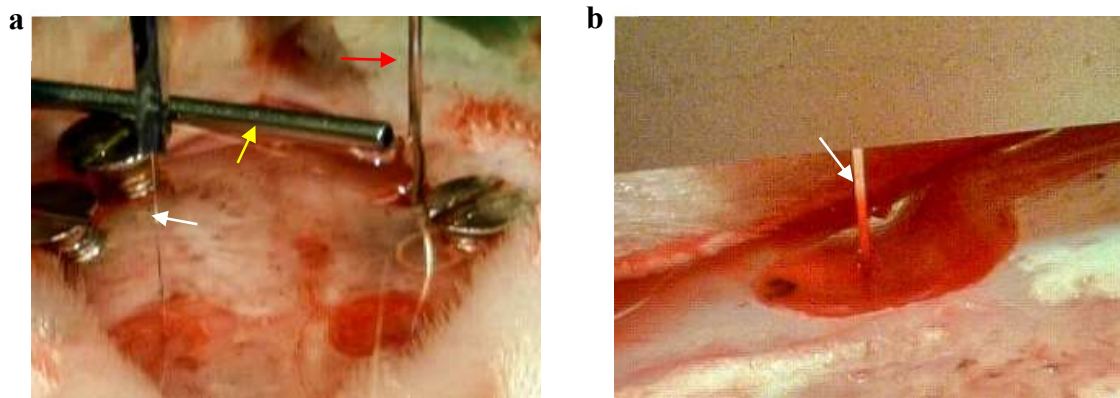
Figure 4.22 Optical image of the stereotaxic implantation of a ULTS probe into an anaesthetized rat brain. The white, yellow and red arrows indicate the ULTS probe, the cold saline outlet and the hypodermic temperature probe, respectively. (**b**) Optical image of an implanted ULTS probe in a rat brain. Arrow indicates the probe.
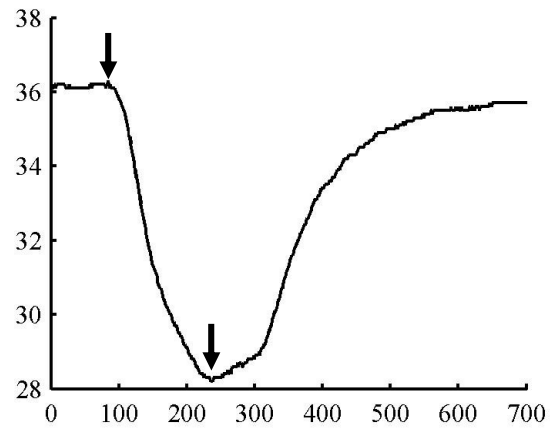
Figure 4.23 A representative brain temperature curve that shows the brain cooling and temperature recovery process. Arrows indicate the start and end of the application of cold saline solution (~10 ℃).
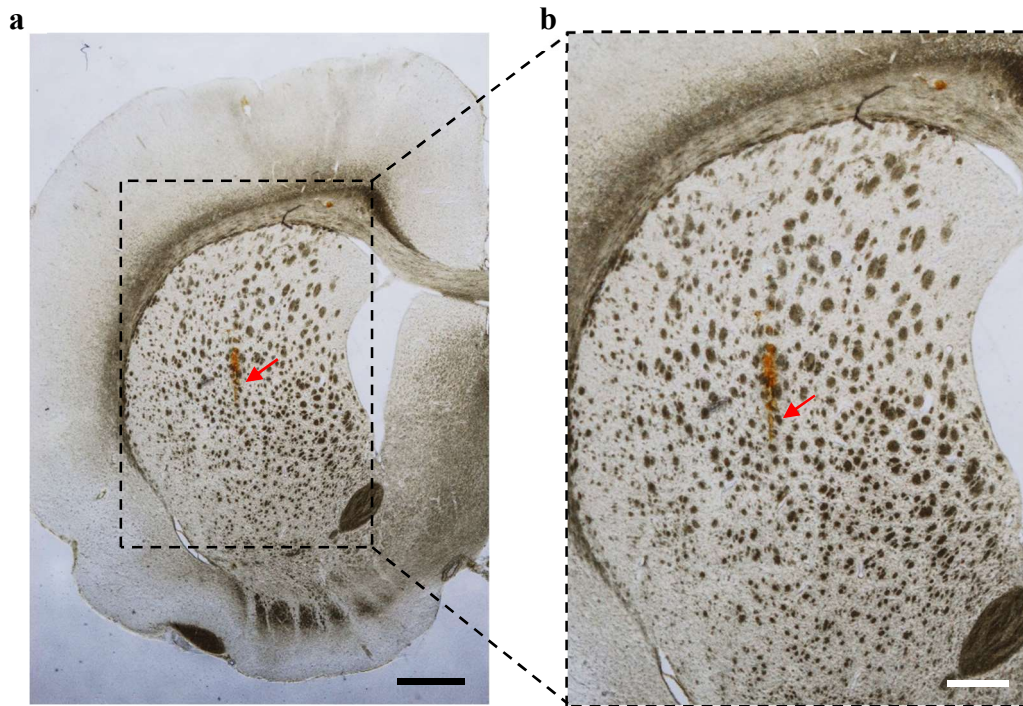
Figure 4.24 Probe insertion into a rat striatum. (**a**) Bright field image of a brain slice cut along the probe insertion direction. The red arrow indicates the implanted position of the probe in the rat striatum, evidenced by the wound caused by the acute implantation process. Scale bar: 1 mm (**b**) Zoomed-in view of the brain slice. Scale bar: 0.5 mm

After the implantation of the probe, the temperature probe was removed and the microscale IrOx reference electrode was inserted at the same spot for acute electrochemical sensing and chemical delivery tests. Animals remained under anesthetic throughout the experiment. The entire experiment was conducted inside a Faraday cage. The biosensor was connected to the FAST-16 potentiostat and a potential of 0.6 V versus IrOx was applied. The electrode signal was allowed to equilibrate to baseline for approximately 30 mins. Changes in signals were recorded following pressure ejection of high potassium aCSF or L-glutamate by a pressure source (FemtoJet, Eppendorf) at various time intervals. Responses were recorded across a range of signal amplitudes by increasing the time of pressure ejection (0.3-4.8 s) and thereby increasing the overall volume applied (~1-20 nL).

We first repeated the same experiment of exogenous glutamate injection and detection *in vivo* to observe the glutamate uptake phenomenon. Glutamate (500 μM in aCSF) was injected with various duration to control the injection volumes and each injection condition was repeated for three times (**Figure 4.25**). Unlike the *in vitro* experiments, the *in vivo* signal level dropped rapidly as soon as the injection ends, and typically returns to the baseline level within 3s, which is due to the glutamate uptake by surrounding neurons compared with the *in vitro* slow diffusion based decay (Figure **4.26**). At the same time, multiple injections under same conditions resulted in nearly identical response demonstrated the repeatability of the system for *in vivo* electrochemical sensing paired with neuropharmacology studies.
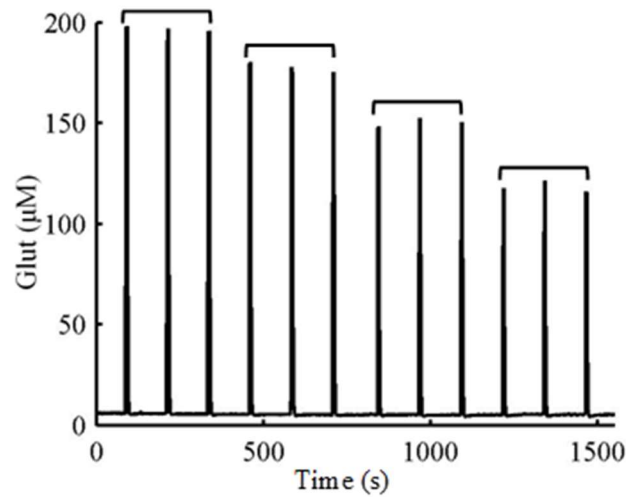
Figure 4.25 Repeated injection of exogenous 500 μM Glut into the rat striatum region with 2 mins interval demonstrating the repeatability of the chemical delivery system. Glut solutions were injected at 60 Psi with injection durations of 2.4 s, 1.2 s, 0.6 s and 0.3 s, respectively, as indicated by the brackets.
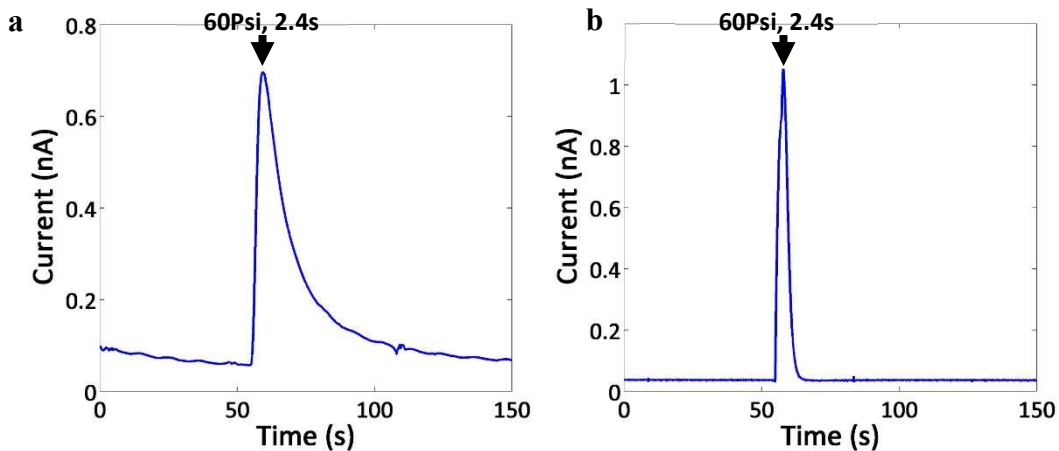
Figure 4.26 Comparison of glutamate injection and detection (**a**) *in vitro* and (**b**) *in vivo*

Second, we also observed physiological phenomena by repeated local injections of potassium enriched artificial cerebrospinal fluid (100 mM K^+ aCSF) to induce glutamate release from neurons (**Figure 4.27a**). Same as reported elsewhere[116] (**Figure 4.27b**), a large glutamate signal was detected followed by an abrupt reduction of induced glutamate

level, presumably due to the depletion of the glutamate storage in neurons. The signal level was slightly recovered after 25 mins recovery period without any stimulation. It should be noted that, the Glut concentration recorded by the ULTS probe is much higher than that of the previous report (~160 μM vs ~30 μM), which is presumably due to the close distance between the liquid outlet and sensing electrodes (<50 μm, edge to edge). Therefore, together with the previous in vivo experiment, multifunctional ULTS probes demonstrate their feasibility in live rodents similar to Si based devices, while the reduced stiffness and dimension would greatly minimize brain damages.
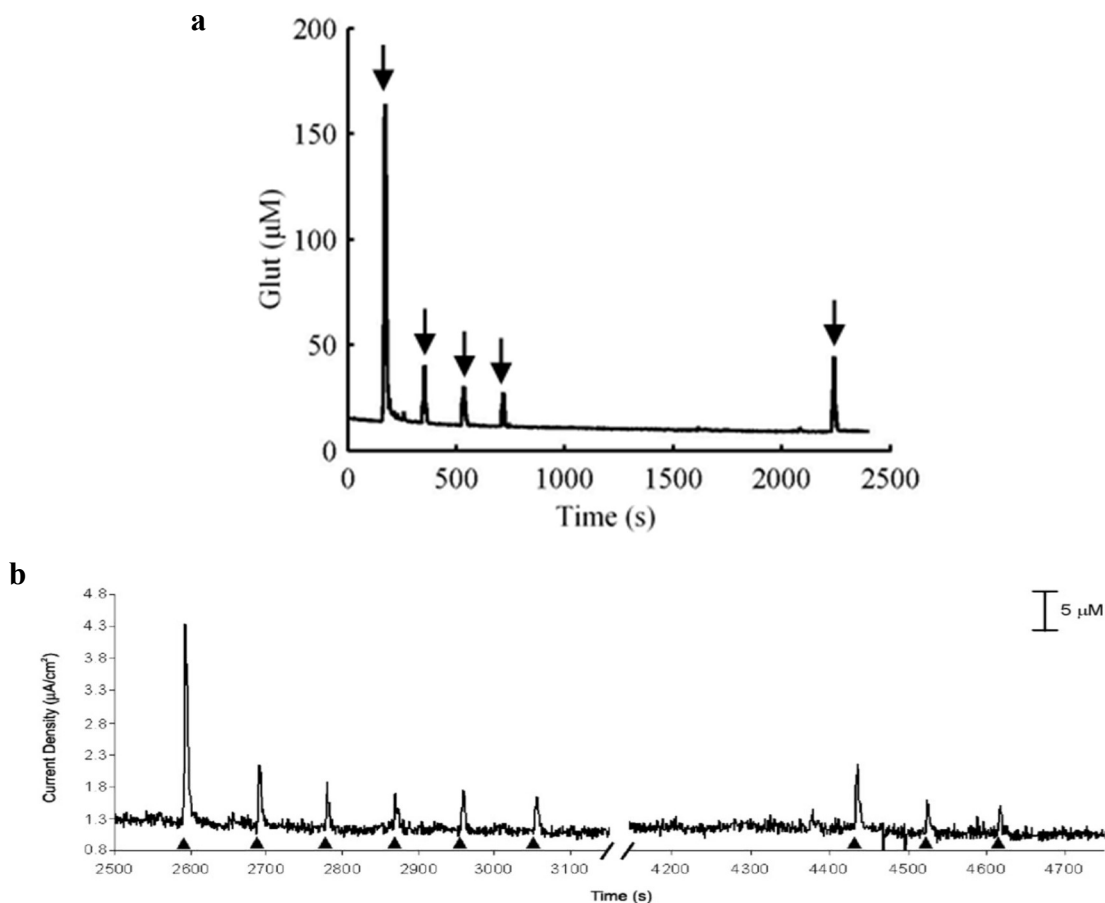
Figure 4.27 (a) Repeated injection of potassium enriched artificial cerebrospinal fluid (100 mM K+ aCSF) in rat striatum to induce Glut release with 2 mins interval. There was an abrupt reduction of induced glutamate level following the first stimulation, which was partially recovered after a prolonged period (25 mins) free from stimulation. Solutions were injected at 60 Psi with an injection duration of 4.8s. (**b**) Same experiment demonstrated by Walker *et al.* [102] showed a similar phenomenon.

4.10 Long-term survival experiment and immunohistochemistry

As described in the introduction, neural probes made from softer substrate material has shown improved implant/tissue integration with reduced foreign body reaction and neuroinflammation response using PVA[68], Parylene-C[99] and etc[74]. However, no one has tested the immune response to PDMS-based ultra-soft neural probe. Therefore, we implanted both an ULTS probe and a size-matched silicon probe (~30 μm thick) into a rat striatum bilaterally. The surgery procedure is similar to the case of acute experiment.

77

Instead, more holes were drilled with one for the implantation of silicon probe on the contralateral hemisphere, and rest of them for screws to anchor the probes. The immune response was evaluated at different time points (2 weeks, 4 weeks and 8 weeks) by immunohistochemistry with procedures described below.

Rats with implanted ULTS and silicon probes were anesthetized with pentobarbital and perfused with 1x PBS (2 mg heparin/100 mL) followed by ice-cold 4% paraformaldehyde in phosphate buffered saline (PBS) transcardially before decapitation. Brains were dissected, postfixed for ~12 hrs at 4 °C with 4% paraformaldehyde in phosphate buffered saline (PBS). Then, the 4% paraformaldehyde solution was replaced by 30% sucrose in PBS at 4 °C. After 2 days, the brain samples were cut into 40 μm sections for immunostaining using LEICA CM 1950 cryosectioning instrument. Horizontal brain tissue sections were washed three times in 1× PBS (10min/each) and blocked using a blocking solution consisting of 0.1% Triton and 5% donkey serum in 1× PBS for 2 h at room temperature. Slices were then incubated with the primary antibody, rabbit anti-GFAP (1:1000 dilution; Millipore) containing 0.1% Triton and 5% donkey serum overnight at 4 °C. After incubation, slices were rinsed 3 times in 3× PBS (10min/each) and 1 time with 1× PBS (10min/each) before they were incubated with the secondary antibodies, Alexa Fluor 488 donkey anti-rabbit (1:100 dilution; Invitrogen) diluted with 2% donkey serum/0.1% Tween in 1x PBS for 2 h at room temperature. Slices were then washed 3 times with 0.1% Tween in 1× PBS (10min/each) and 1 time with 1× PBS (10min/each) before they were mounted on glass slides with coverslips using Aqua-Mount (Richard-Allan Scientific). The slides remained in the dark at 4 ºC before microscopic imaging.

Fluorescence images of the samples were acquired on an Axio Scope.A1 (Zeiss) microscope with AxioCam MRm (Zeiss) camera. Exposure time and other imaging parameters were held constant for all samples. Representative fluorescence images were slightly enhanced using ImageJ to improve visual display.

Following image acquisition, pixel-based image intensity analytics were performed using a modified MATLAB program based on published custom MATLAB script I.N.T.E.N.S.I.T.Y.[67], [117]. In short, an ellipse was drawn to locate the implant-tissue interface. The fluorescence intensity was quantified in 5 μm bins of expanding concentric ellipses around the implantation site up to 300 μm and normalized against the baseline intensity, which was defined as the average intensity in the interval of 500-550 μm away from the center of the implantation site. Statistical analyses were performed using Prism 5.0 (GraphPad Software, USA).

Immunolabeling of GFAP was used to monitor astrocytes[118]. At 2 and 4 weeks post-implantation, GFAP intensity around the silicon probe is significantly higher than that around the ULTS probe, and extended further away from the implant, showing a denser astrocytic scar tissue formed around the silicon probe (**Figure 4.28, 4.29**). GFAP as well as NeuN and ED1 labeling will be applied to longer time points to continue the investigation of the immune response to ULTS and silicon probes. However, the preliminary results from the 2 and 4-week GFAP staining show similar response to other literature[68], which has a lot of promise to reduced inflammation response in longer time.
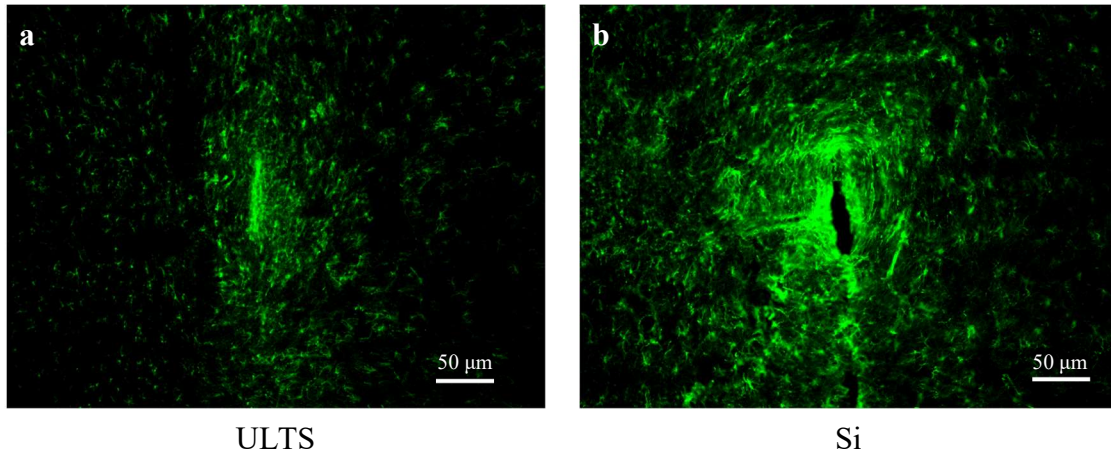
Figure 4.28 Immunohistochemical analysis of the astrocytic scar at 2 weeks. (**a**) ULTS probes vs. (**b**) silicon probes with GFAP staining two weeks after probe implantation. Scale bar, 50 μm.
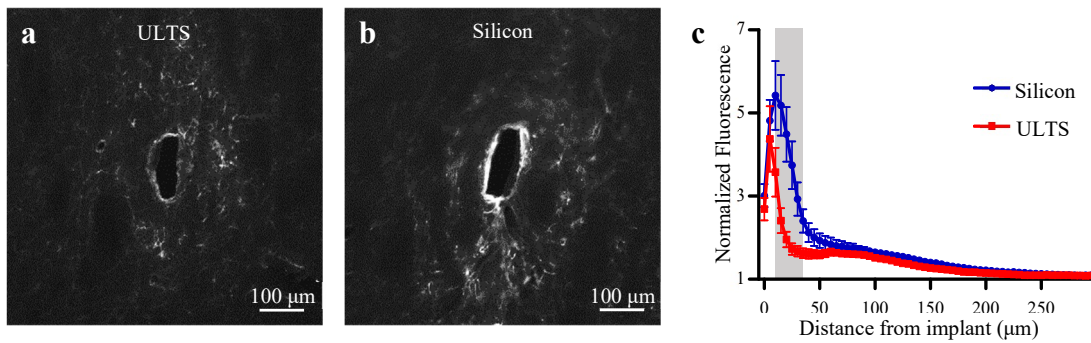
Figure 4.29 Immunohistochemical analysis of the astrocytic scar after 4 weeks of implantation of a ULTS probe and a size-matched Si probe showing reduced scar encapsulation around the ULTS probe. (**a,b**) Representative fluorescence microscopy images of GFAP expression around a ULTS probe and a Si probe respectively. Scale bar, 100 μm. (**c**) There are less astrocytes surrounding ULTS compared to silicon probe. Normalized fluorescence intensity of GFAP expression from the implant-tissue interface to 300 μm away, with 5 μm bin size distance (Silicon n = 10 slices, ULTS n = 10 slices; Two-way ANOVA, probe type and distance interaction: $F_{(59,1080)}$ = 4.95, p <0.0001; Bonferroni post-test for distance at 10-30 μm: p < 0.0001, distance at 35 μm: p<0.001). Gray shadow denotes the significant difference between the ULTS and Silicon probes.

4.10 Discussion

With the advancements of understandings in neural science, deeper and more complicated research questions are raised in academia, while clinically many brain-related diseases such as Parkinson disease can be treated by deep-brain stimulation (DBS). Hence, there is a huge demand for minimally invasive devices to be implanted deep into the brain to record and stimulate neural activities. Here we presented ULTS probes that meet this demand. With the ultra-large tunable stiffness range, ULTS probes are stiff enough to be implanted deep into the brain without temporary carriers, and become extremely soft after implantation so that tissue damage and immune response can be reduced. In addition to the phase change of Ga between solid and liquid state, the stiffness was enhanced by increasing the cross-section area by filling in Ga at higher pressure. When filled at the maximum pressure of 60 Psi, the ULTS probe could penetrate 2 cm deep into brain phantom, which could be potentially used in larger animals such as primates. Regular 9 mm-long ULTS probes with "flat" shape (pressure released after Ga filling) was capable of penetrating brain phantoms, however 15-30 Psi was usually applied to inflate the probe to improve the robustness of the implantation process. When higher stiffness is needed for deeper penetration, the stiffening channel could be fabricated using elastomers with higher stretchability to further increase the probe deformation under same filling pressure.

It should be noted that the calculation of tunable stiffness range is conservative. On the stiff side, semicircle shape was used to simplify the calculation, while in practice the stiffening channel can be filled with larger pressure, e.g. 60 Psi, leading to a major arc shape which is larger than semicircle. On the soft side, the stiffening channel can be contracted with active suction which reduces the probe thickness from 30 μm to ~20 μm,

that further lower the bending stiffness by a factor of 3.375 due to the cubic scaling. Therefore, the tunable stiffness range can be larger than 5 orders of magnitude based on the current ULTS probe design. In addition, compared to other self-implantation approaches, ULTS probes, with similar dimension, can be implanted much deeper. Despite the higher modulus of Ga (10 GPa vs. 2-5 GPa[96], [98], [119]), the tip of the unique "dolphin head" structure (**Figure 4.30**) after expansion remains sharp in 3D and likely reduces the force needed to penetrate the brain surface. With sharper tips, more tissues would be pushed to the sides instead of squeezed along the penetration direction to reduce initial tissue damages.
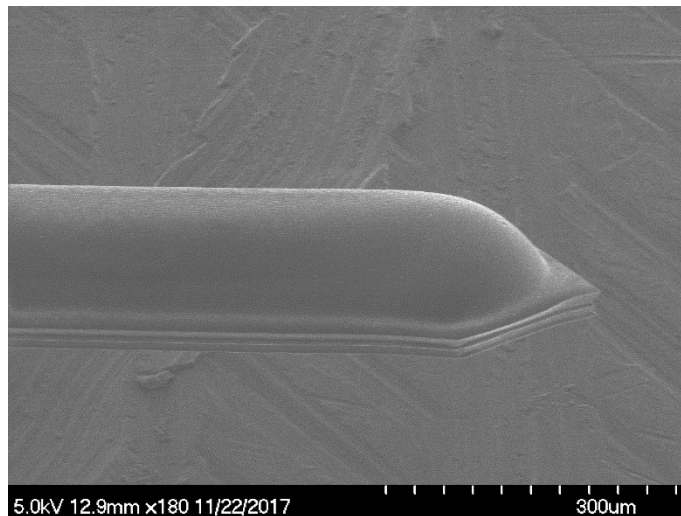
Figure 4.30 SEM image of the "dolphin head" structure of the ULTS probe tip, forming a 3D sharp tip.

The layer-by-layer thin film transfer process has the intrinsic advantage of creating microchannels, which is intricate using conventional MEMS fabrication. As demonstrated in this work, microchannels can be utilized for electrical interconnects and fluidic delivery, moreover, they can be easily converted into optical waveguides for optogenetics applications when filled with higher refractive index fluid. In this work, the number of

electrodes are limited by the large electrode size required by electrochemical sensing but not the electrical interconnects. On the contrary, the linewidth of microchannels are defined by lithography, meaning it can be scaled up to match the electrodes count of conventional probes. Although electrophysiology recording and electrical stimulation were not performed in this study, the impedance of the electrodes, 21.4 ± 1.50 kΩ (n = 5) at 1 kHz (**Figure 4.30a**), is at least identical to Si based probes with platinum electrodes due to the highly conductive liquid metal interconnect. Moreover, rough Pt surface (Platinum grass[115]) can be easily deposited electrochemically to increase the effective surface area and lower the impedance to 6.74 ± 0.49 kΩ (n = 3) at 1 kHz (**Figure 4.30b**) and resulted in a charge storage capacity of 4.5 mC/cm^2 (**Figure 4.30c**) and exhibited a typical Pt electrode property (**Figure 4.30d**). Therefore, we believe that with proper electrode design, ULTS probes can be easily converted for electrophysiology recording and electrical stimulation applications.
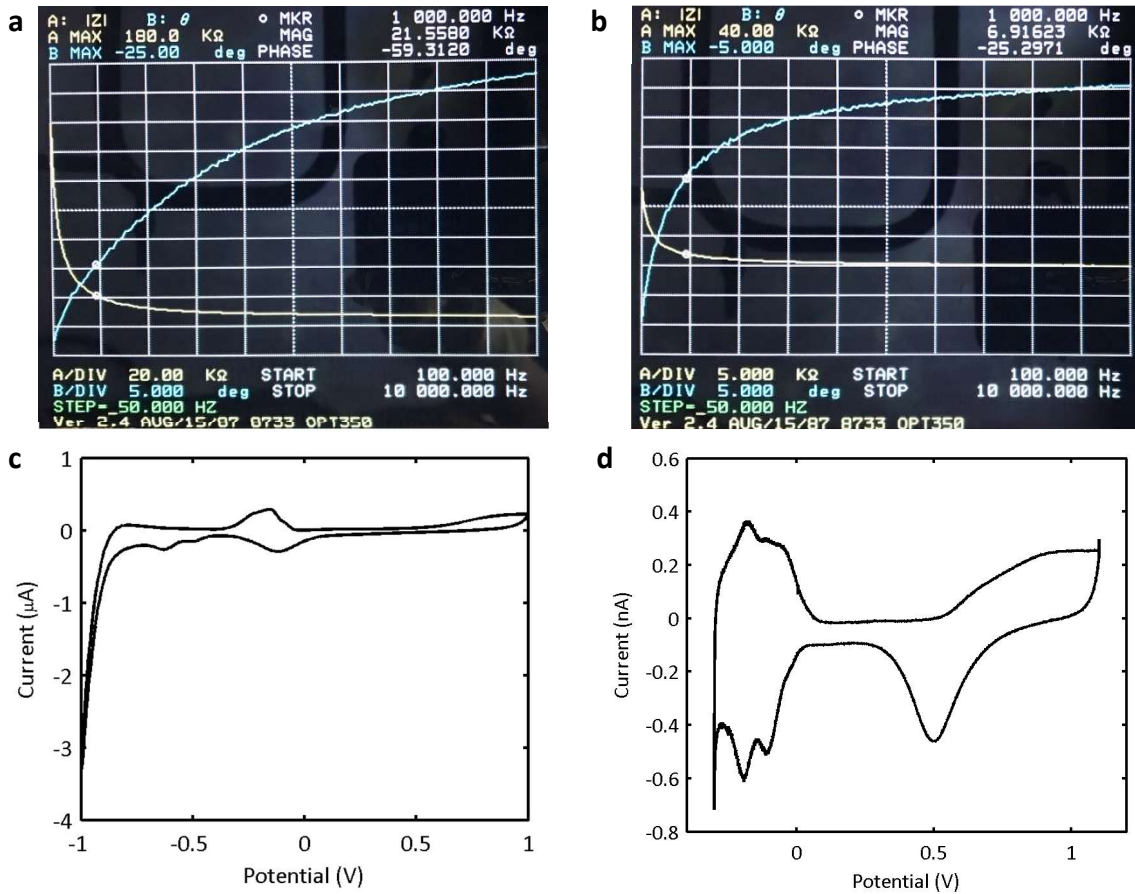
Figure 4.31 Electrical characterization of electrodes. (a) A representative electrochemical impedance spectroscopy (EIS) measurement of a regular Pt electrode of the ULTS probe in saline solution (pH 7.4). The impedance of the regular electrodes, 21.4 ± 1.50 kΩ (n = 5) at 1 kHz, which is similar to the Pt electrodes on Si probes. (b) The impedance decreases to 6.74 ± 0.49 kΩ (n = 3) at 1 kHz with the electrodeposition of rough Pt grass surface. (c) Cyclic Voltammetry (CV) measurement of the Pt grass coated electrodes in saline (pH 7.4) in the range of -1 V to 1 V vs. Ag/AgCl, with a potential scan rate of 100 mV/s. Charge storage capacity is determined by the *integral area of CV curve/(2 × scan rate) = 2.54 µC*. (d) CV measurement of the Pt grass coated electrodes in a diluted sulfuric acid solution (0.5 mM) in the range of -0.3 V to 1.1 V vs. Ag/AgCl, with a potential scan rate of 100 mV/s. The measurement reveals a typical Pt electrode response with high current density.

To implant ULTS probes, selective brain cooling method was used without altering the core temperature. The practice has been widely used to inhibit neural activities and alter behaviors in research labs, as well as clinically used as therapeutic tool in cardiac arrest, hypoxic ischemic neonatal encephalopathy, stroke and brain trauma[120]. With

extensive studies, brain appears to tolerate temperature reduction (0-36 ºC) well for relatively brief period (1-3h), which is fully reversible without significant consequences[121]–[124]. In this work, survival surgeries were performed on 7 rats with ULTS probes implanted with procedures described above. 6 rats survived and behaved normally after surgery, while 1 rat died right after anesthesia before surgery. The results confirm that brief period (~10 mins) of selective brain cooling process shows no observable effect on rats. In the current implantation protocol, a separate temperature probe is used to monitor the brain temperature, which would increase the surgery complexity and invasiveness. In the future, temperature sensor can be integrated by patterning platinum filament on the probe tip to monitor the brain temperature for both implantation purpose and biological studies.

Of note is that ULTS is a platform technology that allows the integration of multiple functional modules on compact and elastic probes that can self-penetrate deep into a brain. Although functions of electrochemical sensing and fluid delivery are shown in the work, these are still proof-of-concept demonstration. The optimization of these functional modules will most likely be based on different specific applications in the future, which will be beyond the scope of this work. For example, the enzyme coating needed for electrochemical sensing may degrades after 7 days, and long-term electrochemical sensing on ULTS is not yet ready. Other optimization such as surface coating the microfluidic channels might also be needed for delivery of drug that may be absorbed on the channel walls through non-specific absorption.

Chapter 5

Conclusion

Electrical-based neural recording including electrochemical sensing of chemicals and extracellular electrophysiological recording is one the most important tools to detect neuronal activities in deep brain regions with minimal invasiveness. Neural probes have been developed for over several decades, however, the existing devices are far from perfect. A great amount of effort has been put to improve the current platform in the directions such as (1) increasing the functionalities of an integrated neural probe to enable more complicated neuroscience research, (2) improving the biocompatibility for stable long-term recordings, and (3) increasing the number of simultaneously recorded neurons. The works presented here aimed to develop innovative neural probes that tackle the first two problems.

The work described in Chapter 2 presented silicon neural probes with integrated optical waveguides and electrochemical sensors. By using ultra-thin silicon nitride waveguides and grating couplers, the light stimulation zone was well matched to the sensing zone. The probe was validated by the successful detection of the light-induced glutamate release in rats.

In chapter 3, we demonstrated silicon probes with integrated chemical delivery channels and electrochemical sensors. An innovative PDMS thin-film transfer process was developed to transfer microfluidics channels to existing silicon probes as an add-on function. Microfluidics channels were integrated with two silicon probe designs, including the optogenetics probes developed in chapter 2 and the conventional silicon probes for

biosensing. The latter case was validated *in vivo* by injection and detection of exogenous glucose in rat striatum.

In chapter 4, we aimed to improve the longevity of intracortical implants by developing a PDMS-based ultra-soft neural probe to minimize the mechanical mismatch and micromotion between the implants and brain tissue. To implant the highly flexible and soft probe into brain, we invented a strategy of using liquid metal (Ga) to tune its mechanical stiffness from extremely stiff for deep brain implantation to extremely soft to reduce brain damage. At the same time, Ga was also used as electrical interconnects without any adhesion issue. The probe was designed with a microfluidic channel for chemical delivery function. Acute *in vivo* testing validated the functions of electrochemical sensing and chemical delivery of the new device. Probes were implanted in animals for longer time and showed reduced scar encapsulation around the soft PDMS probe.

Appendix A

Fabrication process for PDMS probes with electrodes

- General photolithography process
  <u>AZ 5214</u>:

  Vapor deposition of adhesive layer HMDS for 3min

  Spin coating

  step 1: rate 500 rpm, ramp 500 rpm/s, 5 sec

  step 2: rate 3000 rpm, ramp 1000 rpm, 30 sec

  Soft bake 100°C, 1 min

  Exposure 9.5 sec;

  Develop AZ400K 1:4

  Hard bake 120°C, 2 min

  Descum using technics (500 mTorr, 80 W, 1 min)

  <u>AZ 5214 IR</u>:

  Vapor deposition of adhesive layer HMDS for 3min

  Spin coating

  step 1: rate 500 rpm, ramp 500 rpm/s, 5 sec

  step 2: rate 4000 rpm, ramp 1000 rpm, 30 sec

  Soft bake 90°C, 2 min 10 sec;

  Exposure 3 sec

Post bake 128°C 30sec

Flood exposure 25 sec (longer than 16.8 sec should be fine)

Develop AZ400K 1:3 or 1:4

Hard bake at 120°C 2 min or dehydration bake for lift off process at 50°C 5 min

Descum using technics (500 mTorr, 80 W, 1 min)

AZ 4620:

Vapor deposition of adhesive layer HMDS for 3min

Spin coating

step 1: rate 500 rpm, ramp 500 rpm/s, 5 sec

step 2: rate 2500 rpm, ramp 1000 rpm, 30 sec

Soft bake 100°C, 2 min;

Exposure 25 sec

Develop AZ400K 1:3 or 1:4

Hard bake at 120°C 2 min or dehydration bake for press through structure at 50°C

5 min

Descum using technics (500 mTorr, 80 W, 1 min)

1. First insulation layer
   - Grow 1um thick thermal oxide
   - Pattern oxide layer
     i. Use AZ 5214 to transfer patterns from mask
     ii. BOE isotopically etch oxide for 10 min
        - Caution: This step should be performed by a continuous etching of oxide or wafers should stay in liquid all the time. Otherwise, the sidewalls of the undercut area could be quite rough.

- Caution: Use Nanospec recipe 1 (oxide on silicon) to measure remaining oxide thickness. Recipe 7 (thin oxide on silicon) sometimes does not show accurate thickness and hence don't just rely on the measurement data. Carefully inspect using Microscope.
- Caution: wash wafers for at least 5 cycles and spin dry
  - iii. Remove PR using Matrix (250°C, 3min)

2. E-beam deposition of Cr/Pt/Cr films
   - Pattern electrode
     - i. Use AZ 5214 IR to transfer patterns from mask
       - Caution: make sure develop just right by checking alignment mark
       - Caution: Do dehydration bake at 50°C for 5 mins instead of hard bake at 120°C to prevent PR reflow
       - Caution: Descum before e-beam evaporation (technics 500 mTorr, 80 W, 1 min)
   - E-beam evaporation
     - i. Cr/Pt/Cr = 20 nm/ 100 nm/ 50 nm
     - ii. Deposition rate = 1 Å/s
       - Caution: Chromium film can't be thicker than 50 nm. PR could be detached from the surface during the process
   - Metal film Lift off
     - i. Immerse wafers in acetone bath for 2 hours
     - ii. Ultrasound in acetone for 5 secs for 3 times in 3 different beakers and rinse with methanol, IPA, and DI water
       - Caution: Keep wafers immersed in solution while handling, to prevent redeposit of metal or debris onto wafers
       - Optional: Oxygen plasma using Technics, Matrix, or Tegal can be applied to enhance adhesion for later on silicon oxide deposition

3. Second insulation layer
   - Deposit silicon oxide
     - i. Use STS-PECVD to deposit a total of approximate 400 nm oxide layer using recipe 5LFSO by two runs of 7 min 35 sec
       - Caution: Clean chamber when accumulated thickness is more than 8 μm. Rotate wafer during deposition process to eliminate pinholes
       - Caution: record thickness of oxide film
   - Pattern silicon dioxide
     - i. Use AZ 5214 to transfer patterns from mask
     - ii. Use AOE recipe OXIDAPIC to etch oxide for at least 1 min 35 sec
     - iii. Remove PR using Matrix (250°C, 3min)

4. First PDMS thin film
   i. Use AZ 4620 to pattern vias
      - Caution: Do dehydration bake at 50°C, 5min, to prevent PR reflow
      - Caution: Cover 2 inch area with PDMS and remove outer PR for thin film press through process
      - Caution: Descum using Technics (500 mTorr, 80 W, 1 min)
      - Caution: Keep it in room temperature for 4 hours after descum
   ii. Make PDMS thin film
      - Prepare PDMS 10:1 with platinum 0.6x~1x μL
        - Ex. 10g PDMS base : 1g curing agent : 0.6-1μL platinum
      - Oxygen plasma using Technics (500 mTorr, 80 W, 30 sec)
      - Pour uncured PDMS and covered with reused silane-coated glass
      - Degas at lab and press followinging standard thin film process
      - Wait until PDMS fully cured
   iii. Remove PDMS residue
      - Use Oxford RIE recipe pdms_xm to etch PDMS for 3 mins or longer. Since the etching rate differs among the areas, PDMS film becomes nonuniform, which prevents the second thin film bonded successfully. Hence, more than 5 mins etching time is not recommended.
      - Caution: Make sure the residue has been etched or taped off by inspecting if there is light interference pattern among those areas
   iv. Remove AZ 4620 in acetone
      - Caution: If there is PR enclosed by PDMS residue, PR could still stay inside after the cleaning process, which becomes stubborn and hard to be removed.
      - Caution: Make sure all residual PDMS film has been taped off
   v. Etch oxide
      - Use AOE recipe oxidapic for at least 1 min 35 sec. Make sure the oxide layer has been removed thoroughly
      - Or use Oxford RIE recipe oxide_s for two runs of 7 min 30 sec
      - Caution: Oxygen plasma using Technics (500 mTorr, 80 W, 1 min) to remove organics deposited during AOE
- Second PDMS thin film (wires) and third PDMS thin film (stiffening channels)

      i.   Use aligner bonder to pre-align PDMS film(s) on silicon wafer with another PDMS film carried by a PDMS buffer, a glass slide, and a plastic frame
- Caution: Fix bottom substrate and top film with gap of 100 um. Make sure the gaps at left and right alignment marks are similar by checking the focal planes

      ii.   Do oxygen plasma bonding using Technics (500 mTorr, 80 W, 30 sec)
- Caution: If there is dust deposited on film, use tape to pick it up and prevent tape to contact films directly

      iii.   Use aligner bonder to bond the PDMS film(s) on silicon wafer with the PDMS film carried by the PDMS buffer, glass slide, and plastic frame
- Caution: Decrease gap by 30 um each time and turn off vacuum pump when two films contact
- Caution: Gently and evenly squeeze the films to make sure the bonding is okay under microscope. Bake in oven at 70°C for at least 1 hour for transfer of second layer and 2 hours for transfer of third layer

      iv.   Remove carriers
- Remove plastic frame, glass, and PDMS buffer step by step
- Caution: Be careful when removing PDMS buffer. To prevent cracking of films, silane treatment on thin films before making PDMS buffer is needed. When the width of suspending membrane is wider than 50 um, 1 uL silane vapor coating (10 min vacuum and 10 min coating) is recommended.
- Caution: Make sure there is no residual PDMS films at inlets and edges of probes

- Adapter
      i.   Punch holes
- Use 0.5 mm puncher to drill holes on adapter from the side with inlets patterns. Carry the adapters by glass slides.
- Caution: The surfaces of adapters might have silane residue transferred from silane-coated glass slide. Use tape to remove it as much as possible

      ii.   Do oxygen plasma bonding using Technics (500 mTorr, 80 W, 30 sec)
- Bake at 70°C for at least 4 hours
- Caution: Test bonding strength. If the bonding wasn't good, use spacers to separate unbonded areas and do oxygen bonding again

5. Gallium injection
- Wires

      i.   Fill liquid gallium into channels at the same time
- Caution: Make sure liquid gallium fills into vias

      ii.   Solidified liquid gallium under atmosphere pressure
- Use solid gallium to initial solidification process
- Caution: Ice could be used to increase the solidifying speed

- Stiffening channel

      i.   Fill liquid gallium into channel
- Caution: pump air into drug delivery channel to prevent collapse due to expansion of stiffening channel

      ii.   Solidified liquid gallium under 5-60 psi
- Use solid gallium to initiate solidification process
- Caution: 15-30 psi is recommended for gel and brain insertion of <1cm long probe. 60 psi is needed for 2cm long probe and to check the insertion trace in brain
- Caution: Ice is used to increase the solidifying speed

6. Probe releasing using xenon difluoride (XeF_2) etching
   - Cover adapters with PI films or PDMS to prevent the etching of PDMS under the adapter
   - Do 120 pulses of etching: etching pressure 1000 mTorr-1500 mTorr, etching time 30 sec, and purging time 10 sec
     - Caution: Do not open the valve all the way to prevent instant high heat generated at the beginning of each pulse
     - Caution: Do 5 pulses of etching to test if exposed silicon can be etched. If there is no etching of silicon, try to do oxide etching using Technics (150 mTorr CF4, 30 mTorr O2, 100 W, 10 sec)
     - Caution: Make sure probes are released. Total undercut should be more than 330 μm and one can see probes might tilt or lift when being released totally

Reference

[1] K. D. Wise, A. M. Sodagar, Ying Yao, M. N. Gulari, G. E. Perlin, and K. Najafi, "Microelectrodes, Microelectronics, and Implantable Neural Microsystems," *Proceedings of the IEEE*, vol. 96, no. 7, pp. 1184–1202, Jul. 2008.

[2] J. H. Chin and N. Vora, "The global burden of neurologic diseases," *Neurology*, vol. 83, no. 4, pp. 349–351, Jul. 2014.

[3] N. K. Logothetis, "What we can do and what we cannot do with fMRI," *Nature*, vol. 453, no. 7197, pp. 869–878, Jun. 2008.

[4] A. C. Frank *et al.*, "Hotspots of dendritic spine turnover facilitate clustered spine addition and learning and memory," *Nature Communications*, vol. 9, no. 1, Dec. 2018.

[5] B. A. Flusberg *et al.*, "High-speed, miniaturized fluorescence microscopy in freely moving mice," *Nature Methods*, vol. 5, no. 11, pp. 935–938, Nov. 2008.

[6] P. K. Campbell, K. E. Jones, R. J. Huber, K. W. Horch, and R. A. Normann, "A silicon-based, three-dimensional neural interface: manufacturing processes for an intracortical electrode array," *IEEE Trans Biomed Eng*, vol. 38, no. 8, pp. 758–768, Aug. 1991.

[7] K. M. Wassum, V. M. Tolosa, J. Wang, E. Walker, H. G. Monbouquette, and N. T. Maidment, "Silicon Wafer-Based Platinum Microelectrode Array Biosensor for Near Real-Time Measurement of Glutamate in Vivo," *Sensors*, vol. 8, no. 8, pp. 5023–5036, Aug. 2008.

[8] B. Wang, B. Koo, and H. G. Monbouquette, "Enzyme Deposition by Polydimethylsiloxane Stamping for Biosensor Fabrication," *Electroanalysis*, vol. 29, no. 10, pp. 2300–2306, Oct. 2017.

[9] K. Deisseroth, "Optogenetics," *Nature Methods*, vol. 8, no. 1, pp. 26–29, Jan. 2011.

[10] J.-W. Jeong *et al.*, "Wireless Optofluidic Systems for Programmable In Vivo Pharmacology and Optogenetics," *Cell*, vol. 162, no. 3, pp. 662–674, Jul. 2015.

[11] T. D.-B. S. for P. D. S. Group, "Deep-Brain Stimulation of the Subthalamic Nucleus or the Pars Interna of the Globus Pallidus in Parkinson's Disease," *New England Journal of Medicine*, vol. 345, no. 13, pp. 956–963, Sep. 2001.

[12] T. Pradhan, H. S. Jung, J. H. Jang, T. W. Kim, C. Kang, and J. S. Kim, "Chemical sensing of neurotransmitters," *Chem. Soc. Rev.*, vol. 43, no. 13, pp. 4684–4713, 2014.

[13] J. T. Gass and M. Foster Olive, "Glutamatergic substrates of drug addiction and alcoholism," *Biochem Pharmacol*, vol. 75, no. 1, pp. 218–265, Jan. 2008.

[14] F. Blandini, R. H. Porter, and J. T. Greenamyre, "Glutamate and Parkinson's disease," *Mol. Neurobiol.*, vol. 12, no. 1, pp. 73–94, Feb. 1996.

[15] H. Bernheimer, W. Birkmayer, O. Hornykiewicz, K. Jellinger, and F. Seitelberger, "Brain dopamine and the syndromes of Parkinson and Huntington Clinical, morphological and neurochemical correlations," *Journal of the Neurological Sciences*, vol. 20, no. 4, pp. 415–455, Dec. 1973.

[16] J. T. Greenamyre, "Glutamate-dopamine interactions in the basal ganglia: relationship to Parkinson's disease," *J. Neural Transmission*, vol. 91, no. 2–3, pp. 255–269, Jun. 1993.

[17] "Microdialysis," *Wikipedia*. 25-Nov-2017.

[18] K. L. Drew, E. A. Pehek, B. T. Rasley, Y. L. Ma, and T. K. Green, "Sampling glutamate and GABA with microdialysis: suggestions on how to get the dialysis membrane closer to the synapse," *J. Neurosci. Methods*, vol. 140, no. 1–2, pp. 127–131, Dec. 2004.

[19] D. L. Robinson, B. J. Venton, M. L. A. V. Heien, and R. M. Wightman, "Detecting Subsecond Dopamine Release with Fast-Scan Cyclic Voltammetry in Vivo," *Clinical Chemistry*, vol. 49, no. 10, pp. 1763–1773, Oct. 2003.

[20] E. S. Bucher and R. M. Wightman, "Electrochemical Analysis of Neurotransmitters," *Annu Rev Anal Chem (Palo Alto Calif)*, vol. 8, pp. 239–261, 2015.

[21] V. M. Tolosa, K. M. Wassum, N. T. Maidment, and H. G. Monbouquette, "Electrochemically deposited iridium oxide reference electrode integrated with an electroenzymatic glutamate sensor on a multi-electrode arraymicroprobe," *Biosensors and Bioelectronics*, vol. 42, pp. 256–260, Apr. 2013.

[22] Pomerleau F., Day B. K., Huettl P., Burmeister J. J., and Gerhardt G. A., "Real Time in Vivo Measures of l-Glutamate in the Rat Central Nervous System Using Ceramic-Based Multisite Microelectrode Arrays," *Annals of the New York Academy of Sciences*, vol. 1003, no. 1, pp. 454–457, Jan. 2006.

[23] M. Pisanello, F. Pisanello, L. Sileo, and M. De Vittorio, "Photonic technologies for optogenetics," 2014, pp. 1–4.

[24] J. Y. Sim, M. P. Haney, S. I. Park, J. G. McCall, and J.-W. Jeong, "Microfluidic neural probes: in vivo tools for advancing neuroscience," *Lab on a Chip*, vol. 17, no. 8, pp. 1406–1435, 2017.

[25] D. M. O'Connor and N. M. Boulis, "Gene therapy for neurodegenerative diseases," *Trends in Molecular Medicine*, vol. 21, no. 8, pp. 504–512, Aug. 2015.

[26] J. Sevigny *et al.*, "The antibody aducanumab reduces Aβ plaques in Alzheimer's disease," *Nature*, vol. 537, no. 7618, pp. 50–56, Aug. 2016.

[27] T. J. Stachniak, A. Ghosh, and S. M. Sternson, "Chemogenetic Synaptic Silencing of Neural Circuits Localizes a Hypothalamus→Midbrain Pathway for Feeding Behavior," *Neuron*, vol. 82, no. 4, pp. 797–808, May 2014.

[28] B. L. Roth, "DREADDs for Neuroscientists," *Neuron*, vol. 89, no. 4, pp. 683–694, Feb. 2016.

[29] H. Shin *et al.*, "Neural probes with multi-drug delivery capability," *Lab on a Chip*, vol. 15, no. 18, pp. 3730–3737, 2015.

[30] D. J. Heal, S. C. Cheetham, and S. L. Smith, "The neuropharmacology of ADHD drugs in vivo: Insights on efficacy and safety," *Neuropharmacology*, vol. 57, no. 7, pp. 608–618, Dec. 2009.

[31] F. Strumwasser, *Long-term recording from single neurons in brain of unrestrained mammals. Science 127:469*. 1958.

[32] K. C. Cheung, "Implantable microscale neural interfaces," *Biomedical Microdevices*, vol. 9, no. 6, pp. 923–938, Oct. 2007.

[33] G. Buzsáki, "Large-scale recording of neuronal ensembles," *Nature Neuroscience*, vol. 7, no. 5, pp. 446–451, May 2004.

[34] K. D. Wise, J. B. Angell, and A. Starr, "An Integrated-Circuit Approach to Extracellular Microelectrodes," *IEEE Transactions on Biomedical Engineering*, vol. BME-17, no. 3, pp. 238–247, Jul. 1970.

[35] J. J. Jun *et al.*, "Fully integrated silicon probes for high-density recording of neural activity," *Nature*, vol. 551, no. 7679, pp. 232–236, Nov. 2017.

[36] J. L. Shobe, L. D. Claar, S. Parhami, K. I. Bakhurin, and S. C. Masmanidis, "Brain activity mapping at multiple scales with silicon microprobes containing 1,024 electrodes," *Journal of Neurophysiology*, vol. 114, no. 3, pp. 2043–2052, Sep. 2015.

[37] J. Scholvin *et al.*, "Close-Packed Silicon Microelectrodes for Scalable Spatially Oversampled Neural Recording," *IEEE Transactions on Biomedical Engineering*, vol. 63, no. 1, pp. 120–130, Jan. 2016.

[38] K. D. Wise, "Silicon microsystems for neuroscience and neural prostheses," *IEEE Engineering in Medicine and Biology Magazine*, vol. 24, no. 5, pp. 22–29, Sep. 2005.

[39] T. T.-C. Tseng and H. G. Monbouquette, "Implantable microprobe with arrayed microsensors for combined amperometric monitoring of the neurotransmitters, glutamate and dopamine," *Journal of Electroanalytical Chemistry*, vol. 682, pp. 141–146, Aug. 2012.

[40] F. Wu *et al.*, "An implantable neural probe with monolithically integrated dielectric waveguide and recording electrodes for optogenetics applications," *Journal of Neural Engineering*, vol. 10, no. 5, p. 056012, Oct. 2013.

[41] M. Im, I.-J. Cho, F. Wu, K. D. Wise, and E. Yoon, "Neural probes integrated with optical mixer/splitter waveguides and multiple stimulation sites," 2011, pp. 1051–1054.

[42] A. N. Zorzos, E. S. Boyden, and C. G. Fonstad, "Multiwaveguide implantable probe for light delivery to sets of distributed brain targets," *Opt. Lett., OL*, vol. 35, no. 24, pp. 4133–4135, Dec. 2010.

[43] Y. Son *et al.*, "*In vivo* optical modulation of neural signals using monolithically integrated two-dimensional neural probe arrays," *Scientific Reports*, vol. 5, p. 15466, Oct. 2015.

[44] F. Wu, E. Stark, P.-C. Ku, K. D. Wise, G. Buzsáki, and E. Yoon, "Monolithically Integrated µLEDs on Silicon Neural Probes for High-Resolution Optogenetic Studies in Behaving Animals," *Neuron*, vol. 88, no. 6, pp. 1136–1148, Dec. 2015.

[45] T. Kim *et al.*, "Injectable, Cellular-Scale Optoelectronics with Applications for Wireless Optogenetics," *Science*, vol. 340, no. 6129, pp. 211–216, Apr. 2013.

[46] K. Y. Kwon, H.-M. Lee, M. Ghovanloo, A. Weber, and W. Li, "Design, fabrication, and packaging of an integrated, wirelessly-powered optrode array for optogenetics application," *Front. Syst. Neurosci.*, vol. 9, 2015.

[47] E. Iseri and D. Kuzum, "Implantable optoelectronic probes for *in vivo* optogenetics," *Journal of Neural Engineering*, vol. 14, no. 3, p. 031001, Jun. 2017.

[48] I. Papautsky, A. B. Frazier, and H. Swerdlow, "A low temperature IC compatible process for fabricating surface micromachined metallic microchannels," in *Proceedings IEEE The Tenth Annual International Workshop on Micro Electro Mechanical Systems. An Investigation of Micro Structures, Sensors, Actuators, Machines and Robots*, 1997, pp. 317–322.

[49] Liwei Lin and A. P. Pisano, "Silicon-processed microneedles," *Journal of Microelectromechanical Systems*, vol. 8, no. 1, pp. 78–84, Mar. 1999.

[50] S. Chandrasekaran, J. D. Brazzle, and A. B. Frazier, "Surface micromachined metallic microneedles," *Journal of Microelectromechanical Systems*, vol. 12, no. 3, pp. 281–288, Jun. 2003.

[51] S. T. Retterer *et al.*, "Model neural prostheses with integrated microfluidics: a potential intervention strategy for controlling reactive cell and tissue responses," *IEEE Transactions on Biomedical Engineering*, vol. 51, no. 11, pp. 2063–2073, Nov. 2004.

[52] K. B. Neeves, C. T. Lo, C. P. Foley, W. M. Saltzman, and W. L. Olbricht, "Fabrication and characterization of microfluidic probes for convection enhanced drug delivery," *Journal of Controlled Release*, vol. 111, no. 3, pp. 252–262, Apr. 2006.

[53] H. J. Lee, Y. Son, J. Kim, C. J. Lee, E.-S. Yoon, and I.-J. Cho, "A multichannel neural probe with embedded microfluidic channels for simultaneous in vivo neural recording and drug delivery," *Lab on a Chip*, vol. 15, no. 6, pp. 1590–1597, 2015.

[54] K. Seidl *et al.*, "In-plane silicon probes for simultaneous neural recording and drug delivery," *Journal of Micromechanics and Microengineering*, vol. 20, no. 10, p. 105006, Oct. 2010.

[55] P. Zellner, L. Renaghan, Z. Hasnain, and M. Agah, "A fabrication technology for three-dimensional micro total analysis systems," *Journal of Micromechanics and Microengineering*, vol. 20, no. 4, p. 045013, Apr. 2010.

[56] J. Chen, K. D. Wise, J. F. Hetke, and S. C. Bledsoe, "A multichannel neural probe for selective chemical delivery at the cellular level," *IEEE Transactions on Biomedical Engineering*, vol. 44, no. 8, pp. 760–769, Aug. 1997.

[57] A. Pongrácz, Z. Fekete, G. Márton, Z. Bérces, I. Ulbert, and P. Fürjes, "Deep-brain silicon multielectrodes for simultaneous in vivo neural recording and drug delivery," *Sensors and Actuators B: Chemical*, vol. 189, pp. 97–105, Dec. 2013.

[58] S. Spieth *et al.*, "A floating 3D silicon microprobe array for neural drug delivery compatible with electrical recording," *Journal of Micromechanics and Microengineering*, vol. 21, no. 12, p. 125001, Dec. 2011.

[59] C. M. Gray, P. E. Maldonado, M. Wilson, and B. McNaughton, "Tetrodes markedly improve the reliability and yield of multiple single-unit isolation from multi-unit recordings in cat striate cortex," *Journal of Neuroscience Methods*, vol. 63, no. 1, pp. 43–54, Dec. 1995.

[60] M. A. Nicolelis *et al.*, "Chronic, multisite, multielectrode recordings in macaque monkeys," *Proceedings of the National Academy of Sciences*, vol. 100, no. 19, pp. 11041–11046, 2003.

[61] P. J. Rousche and R. A. Normann, "Chronic recording capability of the Utah Intracortical Electrode Array in cat sensory cortex," *Journal of Neuroscience Methods*, vol. 82, no. 1, pp. 1–15, Jul. 1998.

[62] J. R. Capadona, D. J. Tyler, C. A. Zorman, S. J. Rowan, and C. Weder, "Mechanically adaptive nanocomposites for neural interfacing," *MRS Bulletin*, vol. 37, no. 06, pp. 581–589, Jun. 2012.

[63] M. Jorfi, J. L. Skousen, C. Weder, and J. R. Capadona, "Progress towards biocompatible intracortical microelectrodes for neural interfacing applications," *Journal of Neural Engineering*, vol. 12, no. 1, p. 011001, Feb. 2015.

[64] J. Rivnay, H. Wang, L. Fenno, K. Deisseroth, and G. G. Malliaras, "Next-generation probes, particles, and proteins for neural interfacing," *Science Advances*, vol. 3, no. 6, p. e1601649, Jun. 2017.

[65] Y.-T. Kim, R. W. Hitchcock, M. J. Bridge, and P. A. Tresco, "Chronic response of adult rat brain tissue to implants anchored to the skull," *Biomaterials*, vol. 25, no. 12, pp. 2229–2237, May 2004.

[66] K. C. Cheung, P. Renaud, H. Tanila, and K. Djupsund, "Flexible polyimide microelectrode array for in vivo recordings and current source density analysis," *Biosensors and Bioelectronics*, vol. 22, no. 8, pp. 1783–1790, Mar. 2007.

[67] Z. J. Du *et al.*, "Ultrasoft microwire neural electrodes improve chronic tissue integration," *Acta Biomaterialia*, vol. 53, pp. 46–58, Apr. 2017.

[68] J. K. Nguyen *et al.*, "Mechanically-compliant intracortical implants reduce the neuroinflammatory response," *Journal of Neural Engineering*, vol. 11, no. 5, p. 056014, Oct. 2014.

[69] T. Ware, D. Simon, R. L. Rennaker, and W. Voit, "Smart Polymers for Neural Interfaces," *Polymer Reviews*, vol. 53, no. 1, pp. 108–129, Jan. 2013.

[70] J. P. Seymour and D. R. Kipke, "Neural probe design for reduced tissue encapsulation in CNS," *Biomaterials*, vol. 28, no. 25, pp. 3594–3607, Sep. 2007.

[71] T. D. Y. Kozai *et al.*, "Ultrasmall implantable composite microelectrodes with bioactive surfaces for chronic neural interfaces," *Nature Materials*, vol. 11, no. 12, pp. 1065–1073, Dec. 2012.

[72] J. Liu *et al.*, "Syringe-injectable electronics," *Nature Nanotechnology*, vol. 10, no. 7, pp. 629–636, Jun. 2015.

[73] L. Luan *et al.*, "Ultraflexible nanoelectronic probes form reliable, glial scar–free neural integration," *Science advances*, vol. 3, no. 2, p. e1601966, 2017.

[74] T. Zhou *et al.*, "Syringe-injectable mesh electronics integrate seamlessly with minimal chronic immune response in the brain," *Proceedings of the National Academy of Sciences*, vol. 114, no. 23, pp. 5894–5899, 2017.

[75] J. P. Seymour, F. Wu, K. D. Wise, and E. Yoon, "State-of-the-art MEMS and microsystem tools for brain research," *Microsystems & Nanoengineering*, vol. 3, p. 16066, Jan. 2017.

[76] P. Anikeeva *et al.*, "Optetrode: a multichannel readout for optogenetic control in freely moving mice," *Nature Neuroscience*, vol. 15, no. 1, pp. 163–170, Jan. 2012.

[77] E. Stark, T. Koos, and G. Buzsáki, "Diode probes for spatiotemporal optical control of multiple neurons in freely moving animals," *Journal of Neurophysiology*, vol. 108, no. 1, pp. 349–363, Jul. 2012.

[78] N. McAlinden *et al.*, "Thermal and optical characterization of micro-LED probes for in vivo optogenetic neural stimulation," *Opt. Lett., OL*, vol. 38, no. 6, pp. 992–994, Mar. 2013.

[79] B. Rubehn, S. B. E. Wolff, P. Tovote, A. Lüthi, and T. Stieglitz, "A polymer-based neural microimplant for optogenetic applications: design and first in vivo study," *Lab on a Chip*, vol. 13, no. 4, p. 579, 2013.

[80] N. Daldosso *et al.*, "Fabrication and optical characterization of thin two-dimensional Si3N4 waveguides," *Materials Science in Semiconductor Processing*, vol. 7, no. 4, pp. 453–458, Jan. 2004.

[81] F. Zhang, L.-P. Wang, E. S. Boyden, and K. Deisseroth, "Channelrhodopsin-2 and optical control of excitable cells," *Nature Methods*, vol. 3, no. 10, pp. 785–792, Oct. 2006.

[82] E. Shim, Y. Chen, S. Masmanidis, and M. Li, "Multisite silicon neural probes with integrated silicon nitride waveguides and gratings for optogenetic applications," *Scientific Reports*, vol. 6, no. 1, Sep. 2016.

[83] A. Gorin, A. Jaouad, E. Grondin, V. Aimez, and P. Charette, "Fabrication of silicon nitride waveguides for visible-light using PECVD: a study of the effect of plasma frequency on optical properties," *Optics Express*, vol. 16, no. 18, p. 13509, Sep. 2008.

[84] A. C. Hoogerwerf and K. D. Wise, "A three-dimensional microelectrode array for chronic neural recording," *IEEE Transactions on Biomedical Engineering*, vol. 41, no. 12, pp. 1136–1146, Dec. 1994.

[85] I. R. Minev *et al.*, "Electronic dura mater for long-term multimodal neural interfaces," *Science*, vol. 347, no. 6218, pp. 159–163, Jan. 2015.

[86] J. H. Jennings, G. Rizzi, A. M. Stamatakis, R. L. Ung, and G. D. Stuber, "The Inhibitory Circuit Architecture of the Lateral Hypothalamus Orchestrates Feeding," *Science*, vol. 341, no. 6153, pp. 1517–1521, Sep. 2013.

[87] D. J. Chew *et al.*, "A Microchannel Neuroprosthesis for Bladder Control After Spinal Cord Injury in Rat," *Science Translational Medicine*, vol. 5, no. 210, pp. 210ra155-210ra155, Nov. 2013.

[88] X. Wen, T. Liu, and P.-Y. Chiou, "A hybrid silicon-PDMS multifunctional neural probe," in *2016 International Conference on Optical MEMS and Nanophotonics (OMN)*, 2016, pp. 1–2.

[89] Z.-J. Chen *et al.*, "A realistic brain tissue phantom for intraparenchymal infusion studies," *Journal of Neurosurgery*, vol. 101, no. 2, pp. 314–322, Aug. 2004.

[90] Y.-C. Kung, K.-W. Huang, Y.-J. Fan, and P.-Y. Chiou, "Fabrication of 3D high aspect ratio PDMS microfluidic networks with a hybrid stamp," *Lab on a Chip*, vol. 15, no. 8, pp. 1861–1868, 2015.

[91] S. I. Park *et al.*, "Stretchable multichannel antennas in soft wireless optoelectronic implants for optogenetics," *Proceedings of the National Academy of Sciences*, vol. 113, no. 50, pp. E8169–E8177, 2016.

[92] M. L. Reed and W.-K. Lye, "Microsystems for Drug and Gene Delivery," *Proceedings of the IEEE*, vol. 92, no. 1, pp. 56–75, Jan. 2004.

[93] D. V. McAllister *et al.*, "Microfabricated needles for transdermal delivery of macromolecules and nanoparticles: fabrication methods and transport studies," *Proceedings of the National Academy of Sciences*, vol. 100, no. 24, pp. 13755–13760, 2003.

[94] J.-W. Jeong, G. Shin, S. I. Park, K. J. Yu, L. Xu, and J. A. Rogers, "Soft Materials in Neuroengineering for Hard Problems in Neuroscience," *Neuron*, vol. 86, no. 1, pp. 175–186, Apr. 2015.

[95] D. Ziegler, T. Suzuki, and S. Takeuchi, "Fabrication of Flexible Neural Probes With Built-In Microfluidic Channels by Thermal Bonding of Parylene," *Journal of Microelectromechanical Systems*, vol. 15, no. 6, pp. 1477–1482, Dec. 2006.

[96] L. W. Tien, F. Wu, M. D. Tang-Schomer, E. Yoon, F. G. Omenetto, and D. L. Kaplan, "Silk as a Multifunctional Biomaterial Substrate for Reduced Glial Scarring around Brain-Penetrating Electrodes," *Adv. Funct. Mater.*, vol. 23, no. 25, pp. 3185–3193, Jul. 2013.

[97] Z. Xiang *et al.*, "Ultra-thin flexible polyimide neural probe embedded in a dissolvable maltose-coated microneedle," *Journal of Micromechanics and Microengineering*, vol. 24, no. 6, p. 065015, Jun. 2014.

[98] T. Ware *et al.*, "Thiol-ene/acrylate substrates for softening intracortical electrodes," *Journal of Biomedical Materials Research Part B: Applied Biomaterials*, vol. 102, no. 1, pp. 1–11, 2014.

[99] F. Wu, L. W. Tien, F. Chen, J. D. Berke, D. L. Kaplan, and E. Yoon, "Silk-Backed Structural Optimization of High-Density Flexible Intracortical Neural Probes," *Journal of Microelectromechanical Systems*, vol. 24, no. 1, pp. 62–69, Feb. 2015.

[100] S. H. Felix *et al.*, "Insertion of Flexible Neural Probes Using Rigid Stiffeners Attached with Biodissolvable Adhesive," *J Vis Exp*, no. 79, Sep. 2013.

[101] J. Subbaroyan, D. C. Martin, and D. R. Kipke, "A finite-element model of the mechanical effects of implantable microelectrodes in the cerebral cortex," *Journal of Neural Engineering*, vol. 2, no. 4, pp. 103–113, Dec. 2005.

[102] J. H. Lee, H. Kim, J. H. Kim, and S.-H. Lee, "Soft implantable microelectrodes for future medicine: prosthetics, neural signal recording and neuromodulation," *Lab on a Chip*, vol. 16, no. 6, pp. 959–976, 2016.

[103] H. Fang *et al.*, "Ultrathin, transferred layers of thermally grown silicon dioxide as biofluid barriers for biointegrated flexible electronic systems," *Proceedings of the National Academy of Sciences*, vol. 113, no. 42, pp. 11682–11687, Oct. 2016.

[104] "Stretchable and Foldable Silicon Integrated Circuits | Science." [Online]. Available: http://science.sciencemag.org/content/320/5875/507. [Accessed: 29-Mar-2018].

[105] S. P. Lacour, J. Jones, S. Wagner, Teng Li, and Zhigang Suo, "Stretchable Interconnects for Elastic Electronic Surfaces," *Proceedings of the IEEE*, vol. 93, no. 8, pp. 1459–1467, Aug. 2005.

[106] S. P. Lacour, S. Wagner, Z. Huang, and Z. Suo, "Stretchable gold conductors on elastomeric substrates," *Applied Physics Letters*, vol. 82, no. 15, pp. 2404–2406, Apr. 2003.

[107] D.-H. Kim *et al.*, "Materials for multifunctional balloon catheters with capabilities in cardiac electrophysiological mapping and ablation therapy," *Nature Materials*, vol. 10, no. 4, pp. 316–323, Apr. 2011.

[108] A. J. Baca *et al.*, "Semiconductor Wires and Ribbons for High- Performance Flexible Electronics," *Angewandte Chemie International Edition*, vol. 47, no. 30, pp. 5524–5542, Jul. 2008.

[109] M. D. Dickey, "Stretchable and Soft Electronics using Liquid Metals," *Adv. Mater.*, vol. 29, no. 27, p. n/a-n/a, Jul. 2017.

[110] J. P. Lowry, M. R. Ryan, and R. D. O'Neill, "Behaviourally induced changes in extracellular levels of brain glutamate monitored at 1 s resolution with an implanted biosensor," *Anal. Commun.*, vol. 35, no. 3, pp. 87–89, Jan. 1998.

[111] N. Hamdi, J. Wang, E. Walker, N. T. Maidment, and H. G. Monbouquette, "An electroenzymatic l-glutamate microbiosensor selective against dopamine," *Journal of Electroanalytical Chemistry*, vol. 591, no. 1, pp. 33–40, Jun. 2006.

[112] M. R. Ryan, J. P. Lowry, and R. D. O'Neill, "Biosensor for Neurotransmitter L-Glutamic Acid Designed for Efficient Use of L-Glutamate Oxidase and Effective Rejection of Interference," *Analyst*, vol. 122, no. 11, pp. 1419–1424, Jan. 1997.

[113] F. Blandini, R. H. P. Porter, and J. T. Greenamyre, "Glutamate and Parkinson's disease," *Mol Neurobiol*, vol. 12, no. 1, pp. 73–94, Feb. 1996.

[114] N. C. Danbolt, "Glutamate uptake," *Progress in Neurobiology*, vol. 65, no. 1, pp. 1–105, Sep. 2001.

[115] C. Boehler, T. Stieglitz, and M. Asplund, "Nanostructured platinum grass enables superior impedance reduction for neural microelectrodes," *Biomaterials*, vol. 67, pp. 346–353, Oct. 2015.

[116] E. Walker, J. Wang, N. Hamdi, H. G. Monbouquette, and N. T. Maidment, "Selective detection of extracellular glutamate in brain tissue using microelectrode arrays coated with over-oxidized polypyrrole," *The Analyst*, vol. 132, no. 11, p. 1107, 2007.

[117] T. D. Y. Kozai *et al.*, "Chronic tissue response to carboxymethyl cellulose based dissolvable insertion needle for ultra-small neural probes," *Biomaterials*, vol. 35, no. 34, pp. 9255–9268, Nov. 2014.

[118] M. Eddleston and L. Mucke, "Molecular profile of reactive astrocytes— Implications for their role in neurologic disease," *Neuroscience*, vol. 54, no. 1, pp. 15–36, May 1993.

[119] H.-J. Jin *et al.*, "Water-Stable Silk Films with Reduced β-Sheet Content," *Adv. Funct. Mater.*, vol. 15, no. 8, pp. 1241–1247, Aug. 2005.

[120] H. Wang *et al.*, "Brain temperature and its fundamental properties: a review for clinical neuroscientists," *Front Neurosci*, vol. 8, Oct. 2014.

[121] A. Percy, S. Widman, J. A. Rizzo, M. Tranquilli, and J. A. Elefteriades, "Deep hypothermic circulatory arrest in patients with high cognitive needs: full preservation of cognitive abilities," *Ann. Thorac. Surg.*, vol. 87, no. 1, pp. 117–123, Jan. 2009.

[122] T. Oku *et al.*, "The influence of focal brain cooling on neurophysiopathology: validation for clinical application," *Journal of Neurosurgery*, vol. 110, no. 6, pp. 1209–1217, Mar. 2009.

[123] P. Girard and J. Bullier, "Visual activity in area V2 during reversible inactivation of area 17 in the macaque monkey," *Journal of Neurophysiology*, vol. 62, no. 6, pp. 1287–1302, Dec. 1989.

[124] R. A. W. Galuske, K. E. Schmidt, R. Goebel, S. G. Lomber, and B. R. Payne, "The role of feedback in shaping neural representations in cat visual cortex," *PNAS*, vol. 99, no. 26, pp. 17083–17088, Dec. 2002.